

University of Alberta

**Atomic Layer Deposition of Metal Oxide Thin Films on Metallic
Substrates**

by

Ali Foroughi Abari

A thesis submitted to the Faculty of Graduate Studies and Research
in partial fulfillment of the requirements for the degree of

Doctor of Philosophy

in

Materials Engineering

Department of Chemical and Materials Engineering

©Ali Foroughi Abari

Fall 2012

Edmonton, Alberta

Permission is hereby granted to the University of Alberta Libraries to reproduce single copies of this thesis and to lend or sell such copies for private, scholarly or scientific research purposes only. Where the thesis is converted to, or otherwise made available in digital form, the University of Alberta will advise potential users of the thesis of these terms.

The author reserves all other publication and other rights in association with the copyright in the thesis and, except as herein before provided, neither the thesis nor any substantial portion thereof may be printed or otherwise reproduced in any material form whatsoever without the author's prior written permission.

Abstract

Atomic layer deposition (ALD) is a powerful ultra-thin film deposition technique that uses sequential self-limiting surface reactions to provide conformal atomic scale film growth. Deposition of ALD films on many substrate systems has been studied before; however, limited data is available on deposition on metallic surfaces. The investigation of the growth of Al_2O_3 , HfO_2 , and ZrO_2 as three technologically important metal oxides on metallic substrates is the subject of this thesis. Al_2O_3 , HfO_2 , and ZrO_2 films were grown by ALD on silicon, as a well-studied substrate, in different operating conditions to investigate the effect of process parameters on film properties. To study the growth of oxides on metals, thin metallic substrates were prepared by sputter deposition on silicon wafers and then were transferred to the ALD chamber where the film growth was monitored by *in-situ* spectroscopic ellipsometry. The transfer was performed via a load lock system without breaking the vacuum to preserve the pristine metal surface. Formation of a thin interfacial layer of metal oxide was observed during the initial moments of plasma enhanced ALD, that was due to the exposure of metal surface to oxygen plasma. *In-situ* spectroscopic ellipsometry was used to accurately measure the thickness change of the growing films including the interfacial layer. The thickness of this interfacial oxide layer depended on various process parameters including deposition temperature, order of precursors and plasma pulse length. The interfacial oxide layer was absent during the conventional thermal ALD. However, thermal ALD of oxides on metals exhibited substrate-

inhibited growth, especially at higher deposition temperatures. With the knowledge of ALD growth characteristics on metals, metal-insulator-metal (MIM) devices were fabricated by both thermal and plasma enhanced ALD and electrically characterized. The presence of the interfacial oxide layer altered the device performance by changing the capacitance and current characteristics. Employing this approach, it was shown that ALD can be successfully used in the fabrication process of MIM devices and similar systems where ultra-thin insulating layers need to be uniformly deposited on a metallic surface.

Acknowledgements

The accomplishment of this Ph.D. would never be possible without support from many individuals. I would like to express my gratitude to all the people who have been instrumental in the successful completion of this project.

First and foremost, I would like to thank my supervisor, Dr. Ken Cadien, for all his support, encouragement and guidance during the course of my Ph.D. at the University of Alberta. His expertise, insight, and attitude have been an endless source of inspiration. I am really glad I had the chance to work with him. I would also like to thank the other members of my supervisory committee, Dr. Douglas Ivey and Dr. John Nychka for their advice and support.

It has been an honor and pleasure for me to work with Dr. Abdulhakem Elezzabi, and Dr. Douglas Barlage from the Department of Electrical and Computer Engineering. I would like to thank them for their advice and also providing the opportunity for me to be actively involved in various research projects.

I would like to thank Dimitre Karpuzov, Anquang He, and Shihong Xu from Alberta Center for Surface Engineering and Science (ACSES), Les Schowalter from Nanofab at the University of Alberta, Bruce Rayner from Kurt. J. Lesker, and Greg Pribil from J. A. Woollam for their technical support.

I am also deeply indebted to my friends and colleagues, especially Farshid Vejahati, Pouya Maraghechi, Amir Afshar, Lucy Nolan, and Can Xu for all the friendship and support throughout these years.

Lastly, my special thanks to my beloved wife, Maryam, and my family for their constant love and support. This thesis is dedicated to them.

Table of Contents

| | |
|---|-----------|
| 1 Introduction | 1 |
| 1.1 Atomic Layer Deposition | 1 |
| 1.1.1 ALD Fundamentals | 2 |
| 1.1.2 Plasma-Enhanced ALD | 4 |
| 1.1.3 ALD Precursors | 6 |
| 1.1.4 Role of Substrate | 7 |
| 1.2 ALD of Metal Oxides | 9 |
| 1.2.1 Aluminum Oxide | 9 |
| 1.2.2 Hafnium Oxide | 11 |
| 1.2.3 Zirconium Oxide | 12 |
| 1.3 Metal-Insulator-Metal Diodes | 12 |
| 1.4 Thesis Objectives and Scope | 14 |
| 1.5 References | 16 |
| | |
| 2 Characterization of ALD Oxides | 23 |
| 2.1 Introduction | 23 |
| 2.2 Experimental Procedures | 24 |
| 2.2.1 The ALD Research System | 24 |
| 2.2.2 <i>In-Situ</i> Spectroscopic Ellipsometry | 29 |
| 2.2.3 Composition Analysis | 30 |
| 2.3 Results and Discussion | 30 |
| 2.3.1 Optical Characterization | 30 |
| 2.3.2 Chemical Composition | 47 |
| 2.4 Conclusions | 52 |
| 2.5 References | 53 |
| | |
| 3 Preparation of Sputtered Chromium Thin Films | 56 |
| 3.1 Introduction | 56 |
| 3.2 Experimental Procedure | 58 |
| 3.3 Results and Discussion | 59 |

| | | |
|-------|---|----|
| 3.3.1 | Electrical resistivity | 60 |
| 3.3.2 | Microstructure and surface morphology | 63 |
| 3.4 | Optical Properties | 68 |
| 3.5 | Conclusions | 71 |
| 3.6 | References | 73 |

4 ALD of Oxides on Metal Substrates 75

| | | |
|-------|--|-----|
| 4.1 | Introduction | 75 |
| 4.2 | Experimental | 77 |
| 4.2.1 | Sample Preparation | 77 |
| 4.2.2 | Analysis..... | 78 |
| 4.3 | Results and Discussion..... | 81 |
| 4.3.1 | Optical Properties..... | 81 |
| 4.3.2 | Metal Oxidation under Plasma Exposure..... | 82 |
| 4.3.3 | Growth of Aluminum Oxide..... | 87 |
| 4.3.4 | Growth of Aluminum Oxide on Silver | 94 |
| 4.3.5 | Non-Linear Growth in Thermal ALD..... | 96 |
| 4.3.6 | FTIR Analysis..... | 102 |
| 4.4 | Conclusions | 104 |
| 4.5 | References | 105 |

5 ALD for Fabrication of Metal-Insulator-Metal Diodes 108

| | | |
|-------|--|-----|
| 5.1 | Introduction | 108 |
| 5.2 | Experimental Procedure | 110 |
| 5.3 | Results and Discussion..... | 113 |
| 5.3.1 | Deposition and Film Properties | 113 |
| 5.3.2 | Capacitance Measurements..... | 120 |
| 5.3.3 | IV Characteristics..... | 122 |
| 5.3.4 | MIM Diodes with Multiple Insulating Layers | 128 |
| 5.4 | Conclusions | 129 |
| 5.5 | References | 131 |

6 Summary, Conclusions, and Future Directions 133

List of Tables

| | | |
|-----|---|----|
| 2-1 | Refractive index of Al ₂ O ₃ films at 633 nm deposited by thermal and plasma-enhanced ALD at 100°C and 300°C..... | 37 |
| 2-2 | Operating conditions for ALD of aluminum oxide in thermal and plasma-enhanced ALD modes..... | 37 |
| 2-3 | Operating conditions for ALD of HfO ₂ and ZrO ₂ in thermal and plasma-enhanced ALD modes..... | 41 |
| 2-4 | Chemical composition of Al ₂ O ₃ ALD films. | 47 |
| 2-5 | Chemical composition of HfO ₂ ALD films. | 50 |
| 2-6 | Chemical composition of ZrO ₂ ALD films..... | 50 |
| 3-1 | The effect of sputter system base pressure on the Cr film resistivity at 0.23 and 0.80 Pa Ar sputtering pressure. | 60 |
| 3-2 | XPS results showing surface composition of Cr films prepared at 0.13 and 0.93 Pa after 1 and 4 min of sputter-etching (SE)..... | 66 |
| 3-3 | Refractive index (n) of chromium thin films sputtered at different sputtering pressures..... | 70 |
| 4-1 | Work function energy for Zr, Ta, Cr, and Ni metals..... | 86 |

| | | |
|-----|--|-----|
| 4-2 | Effect of deposition temperature on oxidation of Cr. | 92 |
| 4-3 | Thickness of interfacial oxide layer formed during the PEALD of Al ₂ O ₃ on various metals. The deposition temperature was 100°C. | 93 |
| 5-1 | Chemical composition of Al ₂ O ₃ ALD films | 116 |
| 5-2 | Chemical composition of HfO ₂ ALD films | 116 |

List of Figures

| | | |
|-----|---|----|
| 1-1 | Schematics of an ALD cycle..... | 2 |
| 1-2 | Adsorption of precursor molecules on the substrate surface. Reproduced with permission from [6]..... | 3 |
| 1-3 | Schematic diagram of a typical PEALD reactor with an inductively coupled remote plasma source. | 4 |
| 1-4 | Different types of ALD growth: (a) linear growth; (b) substrate-enhanced growth; (c) substrate-inhibited growth. Adapted from [23]..... | 8 |
| 1-5 | The ALD window is defined as a range of deposition temperatures that leads to ALD- type reactions. | 10 |
| 1-6 | Schematic representation of a MOSFET | 12 |
| 1-7 | Energy diagram for a symmetric MIM diode, Φ is the barrier height, ψ is the metal work function and η is the Fermi level. | 14 |
| 2-1 | Schematic representation of the ALD research system. | 25 |
| 2-2 | View of the ALD research system. | 25 |
| 2-3 | Cross view of the ALD chamber. | 26 |

| | | |
|------|---|----|
| 2-4 | Discharge glow from the oxygen plasma at various plasma powers and oxygen flow rates. (a) 300 W, 60 sccm O ₂ ; (b) 600 W, 60 sccm O ₂ ; (c) 300 W, 20 sccm O ₂ ; (d) 150 W, 5 sccm O ₂ | 28 |
| 2-5 | Typical components of an ellipsometry measurement equipment..... | 29 |
| 2-6 | Thermal ALD growth of aluminum oxide on Si substrate. | 31 |
| 2-7 | Thickness variation during a single ALD cycle consisting of two half-cycles. In phase A, precursor molecules (TMA) are adsorbed on the surface. In the second half-cycle, B, water reacts with the TMA molecules releasing the byproducts. The red dashed line indicates the thickness variation as measured by ellipsometry..... | 32 |
| 2-8 | Increasing the speed of data acquisition to 1 s and increasing the purge time to 10 s gave a more clear view of the thickness variation during each ALD cycle (a). Thickness variation in one single cycle was obtained by averaging the changes over 10 cycles (b). | 33 |
| 2-9 | Ellipsometry data from deposition of Al ₂ O ₃ on Si substrate: (a) Psi and Delta parameters obtained from 10-nm Al ₂ O ₃ layer; (b) optical constants of Al ₂ O ₃ based on Cauchy model. | 34 |
| 2-10 | The dependence of growth per cycle on the deposition temperature for ALD of Al ₂ O ₃ in thermal and plasma-enhanced modes. | 35 |
| 2-11 | Desorption of hydroxyl groups. As the substrate temperature increases, the rate of OH desorption also increases resulting in lower available reaction sites on the surface. | 36 |

| | | |
|------|---|----|
| 2-12 | Variation of GPC as a function of oxygen plasma exposure length in deposition of Al ₂ O ₃ . The GPC decreases when longer plasma pulses are used that is attributed to the plasma etching ability..... | 38 |
| 2-13 | Effect of film thickness on FTIR spectrum for aluminum oxide ALD films. The peak is caused by Al-O stretching vibration..... | 39 |
| 2-14 | FTIR peak height for aluminum oxide films as a function of film thickness..... | 40 |
| 2-15 | Molecular structure of tetrakis(dimethylamino) hafnium (TDMAH) and tetrakis(dimethylamide) zirconium (TDMAZ) used in ALD of HfO ₂ and ZrO ₂ , respectively. | 40 |
| 2-16 | Optical constants of ZrO ₂ and HfO ₂ as a function of wavelength. Tauc-Lorentz parameterization was used to obtain the dispersions..... | 42 |
| 2-17 | Tauc absorption method can be used to determine optical band gap energy, Eg. Here the band gap energy for HfO ₂ ALD film deposited on Si at 200°C is determined to be ~5.5eV by extrapolating the linear part of the curve to cross the photon energy axis. | 42 |
| 2-18 | Growth per cycle during plasma-enhanced ALD of Al ₂ O ₃ , HfO ₂ and ZrO ₂ as a function of deposition temperature. The data is obtained from <i>in-situ</i> spectroscopic ellipsometry during the ALD growth..... | 44 |
| 2-19 | Measured refractive index for ALD oxides at different deposition temperatures..... | 45 |

| | | |
|------|--|----|
| 2-20 | Comparison between measured ZrO ₂ thickness grown by PEALD on GaN substrate using <i>in-situ</i> spectroscopic ellipsometry (a) and TEM imaging (b)..... | 46 |
| 2-21 | XPS survey spectrum for Al ₂ O ₃ ALD film on Si. The main identified elements are O, C, Ar, and Al. Argon peak is only detected after surface cleaning using an Ar ion source due to ion implantation. The spectrum was calibrated by fixing the plot to C1s peak at 284.8 eV..... | 48 |
| 2-22 | High resolution XPS spectra of Al2p and C1s core levels in Al ₂ O ₃ films prepared at different conditions. The plots were calibrated based on C1s reference peak. | 49 |
| 2-23 | XPS survey spectra for HfO ₂ (a), and ZrO ₂ (b) ALD films grown on Si. | 51 |
| 2-24 | High-resolution XPS spectra for HfO ₂ (a), and ZrO ₂ ALD films. The films grown at 100°C by PEALD have shifted to lower binding energies due to change in oxygen/metal ratio. | 51 |
| 3-1 | Schematic diagram showing the influence of argon pressure and substrate temperature on microstructure of sputtered metallic films, reproduced from [8]. The arrow indicates the operating range used in the experiments. | 60 |
| 3-2 | The resistivity of chromium sputtering system #1 and sputtering system #2 as a function of argon pressure | 62 |
| 3-3 | Magnified portion of the zone diagram showing the boundary of zone I and T. The vertical arrow indicates the path of experimental data covering an argon pressure range of 0.13 to 0.93 Pa. | 63 |

| | | |
|-----|--|----|
| 3-4 | SEM images of surface of chromium thin films sputtered under different argon pressures: (a) 0.13 Pa (b) 0.27 Pa (c) 0.40 Pa (d) 0.53 Pa (e) 0.80 Pa (f) 0.93 Pa..... | 64 |
| 3-5 | High resolution XPS spectra of Cr _{2p3/2} core level of the sputtered chromium thin film deposited at 0.13 Pa argon pressure and 0.93 Pa argon pressure. | 65 |
| 3-6 | (a) Schematic of oxidation of porous chromium thin film after exposure to air; (b) Schematic of porous columnar grains surrounded by a thin oxide layer..... | 67 |
| 3-7 | Comparison of the measured and model dispersion curves for 10±1 nm Cr films grown at 0.93 Pa. | 69 |
| 3-8 | Optical properties of Cr thin films deposited at different sputtering pressures..... | 70 |
| 3-9 | Transmittance and reflectance of Cr thin films deposited at different sputtering pressures..... | 71 |
| 4-1 | Schematic of the equipment used for the experiments. | 78 |
| 4-2 | Optical dispersion curves for aluminum oxide (a) and chromium (b) thin films. | 80 |
| 4-3 | AFM images of Cr thin film surface (10 nm thickness) before (a) and after (b) the ALD of Al ₂ O ₃ (5 nm). | 81 |

| | | |
|------|--|----|
| 4-4 | Oxidation of Cr film under oxygen plasma at 100°C. | 82 |
| 4-5 | Oxidation of various metals under oxygen plasma exposure at 100°C..... | 84 |
| 4-6 | Schematic general representation of metal oxidation | 86 |
| 4-7 | Plot of oxide growth for Ta, Cr, and Ni metals during oxygen plasma oxidation based on the Ghez approximation..... | 87 |
| 4-8 | Growth of aluminum oxide on Cr surface; (a) ALD cycles started with TMA pulse; (b) ALD cycles started with plasma exposure..... | 89 |
| 4-9 | Thermal ALD of aluminum oxide on Cr surface at 100°C..... | 90 |
| 4-10 | Effect of plasma exposure time on oxidation of Cr surface during PEALD of aluminum oxide..... | 91 |
| 4-11 | ALD started with 6 cycles of thermal aluminum oxide deposition. | 91 |
| 4-12 | Schematic of radical oxygen diffusion through growing Al ₂ O ₃ and Cr ₂ O ₃ layers. As the ALD film grows, the available oxygen for reaction at the Cr surface decreases until there is very little oxygen available to react with Cr..... | 93 |
| 4-13 | Oxidation of silver layer during oxygen plasma exposure at 100°C..... | 94 |
| 4-14 | Thermal Al ₂ O ₃ ALD on silver at 100°C..... | 95 |

| | | |
|------|--|-----|
| 4-15 | PEALD Al ₂ O ₃ on 0.5 nm thermal Al ₂ O ₃ interface layer on silver at 100°C. | 95 |
| 4-16 | Growth of thermal ALD HfO ₂ and ZrO ₂ on Cr and Si substrates. Unlike deposition on Si, the growth on Cr is initially slower, but gradually increases until stabilizes..... | 96 |
| 4-17 | Thermal ALD of Al ₂ O ₃ on Cr substrate at a deposition temperature of 200°C..... | 97 |
| 4-18 | Effect of water pulse duration on the growth of Al ₂ O ₃ on Cr at a deposition temperature of 300°C..... | 98 |
| 4-19 | The first few cycles during thermal ALD of Al ₂ O ₃ on Cr substrate at a deposition temperature of 200°C. The adsorption of TMA on the surface is identified as a jump in thickness after the first cycle..... | 100 |
| 4-20 | Top-view TEM images of thin Al ₂ O ₃ on Cr at various magnifications.. | 101 |
| 4-21 | FTIR spectra of thin aluminum oxide on Cr films with different Cr/Al ₂ O ₃ interfaces. | 103 |
| 4-22 | FTIR spectra of thin aluminum oxide on Cr films with different Cr/Al ₂ O ₃ interfaces subtracted from the Cr spectrum. | 104 |
| 5-1 | Schematic structure of MIM diodes. The two metallic electrodes are separated by a thin insulating layer. The electrical measurements are performed by applying a potential across the insulating layer. | 110 |

| | | |
|-----|--|-----|
| 5-2 | Schematic layout of the ALD research system. | 111 |
| 5-3 | Growth of Al ₂ O ₃ and HfO ₂ thin films on Cr substrate as measured by <i>in-situ</i> ellipsometry; (a) thermal ALD of Al ₂ O ₃ ; (b) Plasma ALD of Al ₂ O ₃ ; (c) Thermal ALD of HfO ₂ ; (d) Plasma ALD of HfO ₂ . All the depositions were at 100°C. The dashed lines indicate ideal growth. | 115 |
| 5-4 | XPS spectra of ALD films (10-nm) deposited on Si (100) substrate in thermal and plasma modes at 100°C: (a) Al 2p peak from Al ₂ O ₃ ; (b) Hf 4f peaks from HfO ₂ ; (c) C 1s peak from Al ₂ O ₃ ; (d) C 1s peak from HfO ₂ | 118 |
| 5-5 | Cross sectional TEM image of an MIM (Cr/Cr ₂ O ₃ -HfO ₂ -Al ₂ O ₃ /Cr) structure. The bottom-left image schematically shows the structure of the native oxide around the Cr grains and the deposited ALD oxide. | 119 |
| 5-6 | Plan-view SEM image of sputtered Cr surface: (a) as-deposited and (b) after being exposed to oxygen plasma. The oxidation process has changed the morphology of the surface. | 120 |
| 5-7 | CV characteristics of Cr/4.6 nm Al ₂ O ₃ /Cr diodes. A lower capacitance was measured for MIM diodes prepared by PEALD due to presence of a thin interfacial chromium oxide. | 121 |
| 5-8 | Capacitance vs thickness for MIM structures prepared by PEALD and TALD. | 122 |
| 5-9 | IV characteristics of MIM diodes with Cr/Al ₂ O ₃ /Cr structure with an ALD oxide thickness of 4.6 nm. | 123 |

| | | |
|------|---|-----|
| 5-10 | IV curves for MIM diodes with Cr/HfO ₂ /Cr structure..... | 124 |
| 5-11 | IV curves for MIM diodes (Cr/PEALD Al ₂ O ₃ /Cr)..... | 125 |
| 5-12 | IV curves for (a) the Cr/2nm Al ₂ O ₃ - 2 nmHfO ₂ /Cr and (b) the Cr/4 nm HfO ₂ /Cr and Cr/4nm Al ₂ O ₃ /Cr diodes..... | 129 |

List of Abbreviations

AFM: Atomic Force Microscope

ALD: Atomic Layer Deposition

CMOS: Complementary Metal Oxide Semiconductor

CV: Capacitance Voltage

DRAM: Dynamic Random Access Memory

FTIR: Fourier Transform Infrared spectroscopy

GPC: Growth per Cycle

IV: Current Voltage

MIM: Metal Insulator Metal

MOS: Metal Oxide Semiconductor

MOSFET: Metal Oxide Semiconductor Field Effect Transistor

PEALD: Plasma Enhanced Atomic Layer Deposition

QCM: Quartz Crystal Microbalance

SEM: Scanning Electron Microscope

TEM: Transmission Electron Microscope

TMA: Trimethylaluminum

TDMAH: Tetrakis(dimethylamino) Hafnium

TDMAZ: Tetrakis(dimethylamide) Zirconium

XPS: X-ray Photoelectron Spectroscopy

Chapter 1 Introduction *

1.1 Atomic Layer Deposition

Atomic layer deposition (ALD) is a thin film deposition technique based on alternating surface saturating adsorption and reactions of the individual precursors leading to the controlled layer by layer growth of thin films. [1, 2]. ALD is considered to be an ideal deposition technique for preparation of ultra-thin films especially when the geometry is complex [3]. There is a controversy over the origin of ALD. Some suggest that the ALD was originally invented by Russian scientists led by Professor Aleskovskii in an attempt to grow metal oxides such as TiO_2 and GeO_2 during 1960's [4]. However the more commonly referenced origin of ALD is the research done in Finland by Tuomo Suntola and co-workers in 1970's [5]. The method was initially named "Atomic Layer Epitaxy" or ALE and was used to grow layers of ZnS by the employment of alternating element reactants Zn and S. It was later used for deposition of SnO_2 from Sn/O and GaP from Ga/P. Suntola and co-workers soon showed that the same process could use compounds as reactants instead of elements: a $\text{TaCl}_5/\text{H}_2\text{O}$ process to form Ta_2O_5 and an $\text{AlCl}_3/\text{H}_2\text{O}$ process to deposit Al_2O_3 . The name ALE was later gradually

* A version of this chapter has been published as a book chapter: A. Foroughi-Abari and K.C. Cadien in Stepanova, S. Dew, *Nano-fabrication*, SpringerWien 2011

substituted by ALD in the early 1990's, and it is currently the most common name for the technique. More details can be found in an extensive review by Puurunen [4].

1.1.1 ALD Fundamentals

The basic steps in an ALD cycle are schematically shown in Figure 1-1. The first precursor is pulsed into the reaction chamber and is chemically adsorbed on the surface of the substrate until the surface is completely saturated (Figure 1-1a). Once the surface becomes saturated, no further precursor molecule is adsorbed. A constant flow of a carrier gas (typically nitrogen or argon) is used to sweep away the excess gases out of the chamber (Figure 1-1b). The second precursor is pulsed into the chamber and reacts with the adsorbed species on the surface until surface saturation is achieved (Figure 1-1c). Excess precursors and by-products are removed by pumping and carrier gas purging (Figure 1-1d). At the end of these four steps, one monolayer of the desired material is deposited on the substrate surface. By repeating step a to d, the film material with the desired thickness is deposited.

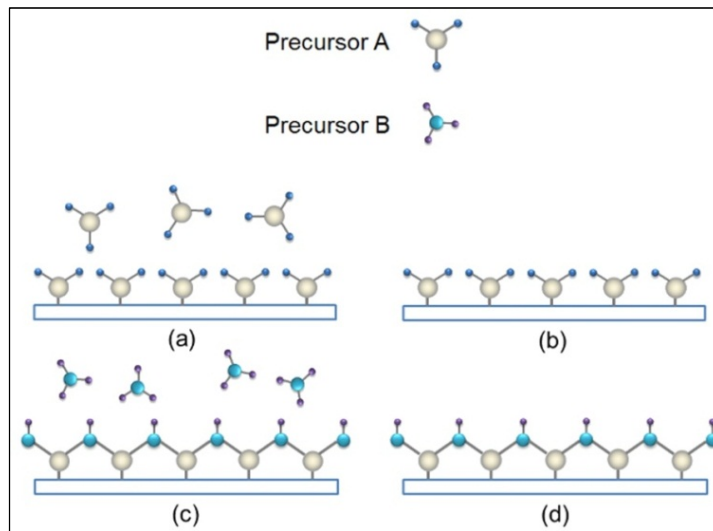


Figure 1-1 Schematics of an ALD cycle

Each cycle usually takes a few seconds to complete and a film with thickness of 0.01 to 0.3 nm may be deposited [3]. The growth rate is determined by the size of the precursor molecules and also the number of available adsorption sites on the surface. Due to steric hindrance, the growth per cycle (GPC) is usually less than a monolayer of the ALD-grown material [4]. Simple models have been developed to show this effect. Figure 1-2 shows a schematic configuration of adsorbed precursor molecules on the surface redrawn from [6]. The number of adsorbed species depends on the size of the molecules. Since ALD precursors are mostly large organometallic molecules, only a fraction of the reaction sites are occupied after each dose of the precursor which results in GPC of less than a monolayer [3]. The surface reactions during ALD are thermally-driven by providing heat to the substrate. Typical substrate temperatures range from 100°C to 400°C. Therefore, this method is sometimes referred to as thermal ALD.

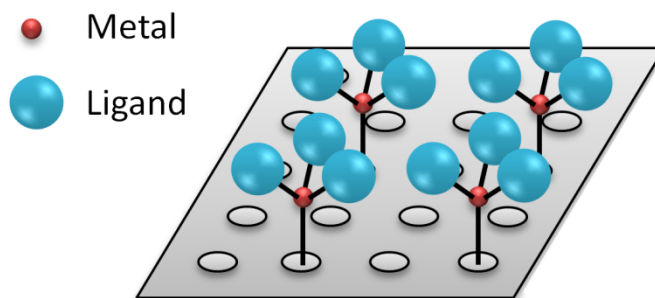


Figure 1-2 Adsorption of precursor molecules on the substrate surface. Reproduced with permission from [6].

ALD is a self-limiting process [7] which means that the film growth does not depend on the flux of reactive species providing that sufficient precursor is dosed. Basically, once the reaction sites on the surface are filled with adsorbed precursor molecules, the surface becomes saturated and no more precursor molecule is adsorbed. The process limits itself and does not proceed until the next precursor is

introduced. This unique feature makes ALD an ideal method to deposit uniform and conformal thin films on complex structures.

1.1.2 Plasma-Enhanced ALD

Plasma-enhanced ALD (PEALD) is an energy-enhanced ALD method that uses radicals to enhance the reactions. In PEALD, also referred to as plasma-assisted ALD or plasma ALD, the surface is exposed to highly reactive species generated by the plasma for a short time (plasma exposure pulse) during each ALD cycle. O_2 , N_2 and H_2 plasmas are typically used in the PEALD process as a source of oxygen, nitrogen and hydrogen. For example, for plasma ALD of alumina, Trimethylaluminum (TMA) is used as the metal precursor and plasma oxygen is used for atomic oxygen. A schematic diagram of a PEALD reactor is shown in Figure 1-3.

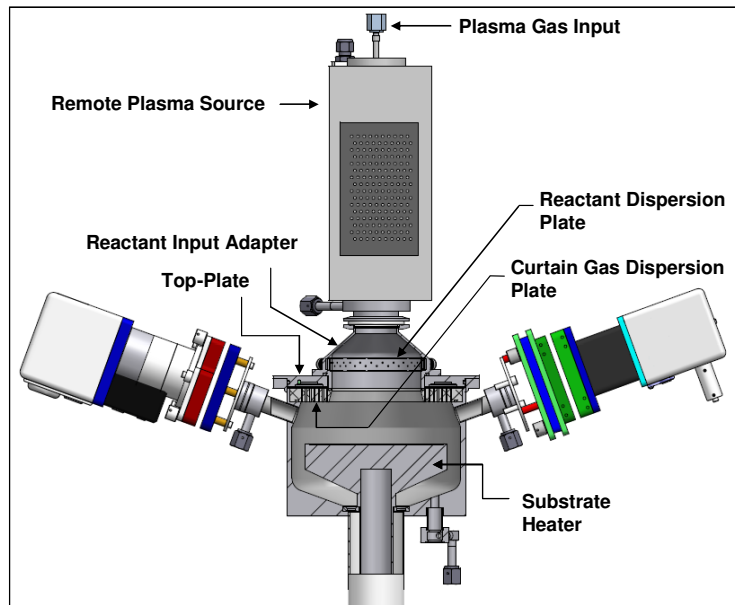


Figure 1-3 Schematic diagram of a PEALD reactor with an inductively coupled remote plasma source.

Theoretical molecular models show that the ALD reactions, such as TMA with water have intermediate metastable states separated by activation barriers [8-11]. In conventional thermal ALD, the required thermal energy to overcome the barrier is provided by heating of the substrate. In PEALD, the energy is provided by both the thermal energy as well as the energy from plasma. The plasma is utilized to generate highly reactive atomic radicals. These radicals can enhance the reactions and allow them to take place at a lower temperature. When plasma is used, the rate of surface reactions increases, fragmentation of precursor molecules increases, and the by-products are more easily removed by ion bombardment. The amount of material deposited after each cycle is determined by the separation between the plasma source and the substrate, the plasma pulse duration, pressure, and plasma power [12].

Three general types of plasma configuration have been used for PEALD: radical-enhanced, direct plasma, and remote plasma [13]. In radical-enhanced configuration, the plasma is generated in a separate chamber that is connected to the main ALD chamber by means of tubing. Therefore the plasma species need to travel through the tubes to reach the ALD chamber and the surface of the substrate. This increases the chance of recombination and results in a decrease in the number of radicals reaching the surface. In direct plasma configuration, however, the plasma is generated above the substrate and the substrate acts as one of the electrodes (usually grounded). In this configuration, the flux of ions and radicals toward the surface could be very high. The design is relatively simple and results in good uniformity (used in industrial systems) but, on the other hand, could lead to plasma-induced damage.

In the third configuration, remote plasma, the plasma is generated above the substrate, however unlike the direct plasma, the substrate is not involved in the generation of plasma. In this situation, the energy and flux of radicals are higher than those of radical-enhanced plasma configuration. Additionally, the damage induced by the plasma is typically less compared to the direct plasma. The main advantage of this type of configuration is that it allows for varying the conditions

of the plasma and deposition chamber independently. Therefore it has been used in research systems where flexibility is required [13].

PEALD has some advantages over the thermal ALD. Some of the main advantages include improvement in film impurity levels [14, 15] and electronic properties [16, 17]. A well-studied example of usage of plasma is for the deposition of aluminum oxide using TMA and plasma oxygen [12, 18-20]. The difference with thermal ALD is that instead of water, oxygen plasma is used as the source of oxygen. With the help of plasma, room-temperature deposition on thermally fragile, heat sensitive polymeric materials has been successfully carried out without destroying them [20, 21]. Another benefit of plasma ALD compared to thermal is that cycles times are much shorter during plasma ALD which results in faster depositions and higher throughput. Additionally, the amount of material deposited after each cycle is usually higher when plasma is used [19].

One of the main limitations of the thermal ALD process is that long purging is usually required to completely remove the water from the reactor due to its polar nature. As the deposition temperature decreases, this problem becomes more significant [22], which poses special challenges at low deposition temperatures. When the water remains at the surface due to improper purging, the films may contain high amounts of hydrogen as an impurity. For this reason, a temperature of 100°C has been suggested as the minimum temperature needed for thermal ALD of Al₂O₃ [20]. This is where PEALD presents its advantage by operating at lower deposition temperatures (down to room temperature) and yet maintaining acceptable quality.

1.1.3 ALD Precursors

The choice of precursor is an important consideration in the design of an ALD process. The precursor must be thermally stable to remain in the gas phase before reaching the substrate. On the other hand it must be reactive enough to chemisorb

on the surface. Precursor decomposition in the gas phase has a detrimental effect on the self-limiting growth mechanism. Additionally, the precursor must have enough vapor pressure when heated to be transferred into the reaction chamber. The transfer can be done in the form of a pure gas or as a vapor mixed with the carrier gas. Another consideration is that the reaction by-products cannot be reactive toward surface species. Otherwise, defect generation and excessive film accumulation could be an issue [23].

TMA and H₂O are considered as classic ALD precursors. Once TMA molecules react with hydroxyl groups (OH) on the surface, CH₄ is formed and Al atoms with one or two methyl (CH₃) groups are bonded to the surface. After purging the excess TMA, H₂O vapor is pulsed into the chamber and the methyl groups, attached to the Al atoms, are replaced by hydroxyl groups. These hydroxyl groups make the surface reactive toward TMA and therefore this cycle can be repeated [7, 24-27].

1.1.4 Role of Substrate

Linear film growth is considered as one of the key features of the ALD technique that is attributed to the self-limiting behavior. After each ALD cycle, a fixed amount of material is deposited that results in linear growth. However, during the initial stages of ALD film growth, non-linear growth might be observed. Lim *et al.* [28] performed an analysis on initial stages of TiN film growth deposited by ALD. They suggested that during the few first ALD cycles, the outermost layer on the surface is gradually changing from the substrate material to the ALD-grown material. Therefore, due to dependence of surface adsorption and reaction of reactants on the substrate surface properties, a non-linear growth regime might be observed. ALD growth is only influenced by the substrate when the substrate is not fully covered with the ALD material. As the deposition continues, the effect of the original substrate is lost until a steady GPC is observed. Three possible scenarios exist [29]: 1- the substrate may increase the GPC during the first few

cycles, referred to as substrate-enhanced growth. 2- the substrate may lower the GPC, referred to as substrate-inhibited growth. 3- the substrate may have insignificant effect on GPC (linear growth). These growth behaviors are shown schematically in Figure 1-4.

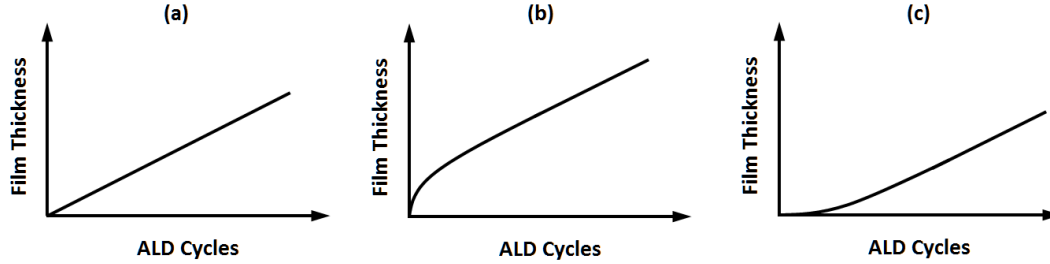


Figure 1-4 Different types of ALD growth: (a) linear growth; (b) substrate-enhanced growth; (c) substrate-inhibited growth.

ALD of metals on oxide substrates is a well-known example of non-linear growth. Elam et al. [30] demonstrated that ALD of W on SiO_2 surface involves nucleation on the surface. They also showed that surface treatments such as exposing the substrate to Si_2H_6 affected the initial growth conditions and resulted in more rapid nucleation. Similar observations were made for ALD of other metals on oxide surfaces [31-33].

Several other studies also showed that the nucleation and initial growth of oxides on Si substrates is affected by the conditions of the surface. For instance, the number of cycles required for nucleation of oxides on OH-terminated Si, H-terminated Si, and Si with native oxide is different [34-40].

The nucleation of ALD is extremely important for deposition of continuous ultra-thin films. Most applications require a uniform continuous pin-hole free layer. The lack of uniform nucleation results in undesired island growth, known as Volmer-Weber growth [22]. Although the islands eventually coalesce after multiple ALD cycles, for applications demanding very thin films, the nucleation

could be an issue. One of the examples of the nucleation problem can be seen in deposition of ultra-thin high k oxides for microelectronics applications [35, 41].

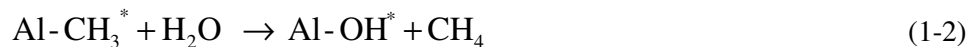
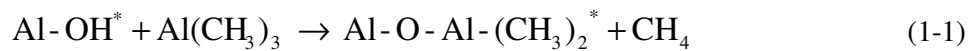
1.2 ALD of Metal Oxides

1.2.1 Aluminum Oxide

Aluminum oxide is perhaps the most studied material among all the oxides deposited by ALD since it is a technologically important material with high permittivity, good electrical properties and good adhesion to different surfaces. Additionally, its ALD processes are considered to be a representative of other ALD reactions [4, 22].

Al₂O₃ has good electrical properties such as wide bandgap (~8.7 eV), high electric field strength (8 MV/cm) [20] and high dielectric constant (~9). Electrical properties and chemical stability of Al₂O₃ have made this material attractive for applications such as microelectronic devices [42], solar energy devices [43], magnetic read heads [44], and wear-resistance coating for microelectromechanical systems (MEMS) [45]. Since Al₂O₃ is chemically stable on silicon, it can be used as a gate oxide on silicon for Metal-Oxide-Semiconductor (MOS) transistors [46, 47]. Al₂O₃ has also been used in the fabrication process of dynamic random-access memory (DRAM) devices [48, 49] due to its excellent dielectric properties.

Deposition of Al₂O₃ by ALD has been extensively studied by many researchers. Various precursors have been employed to satisfy the ALD self-limiting reaction. The most notable precursors are TMA and water [26, 27, 44, 45, 50, 51]. Deposition of aluminum oxide using TMA and water is described by the following half-reactions:



where the asterisks denote the surface species [11, 52]. In reality, the ALD process is not as simple as this and involves different phenomena including physisorption and dissociative chemisorption of precursor molecules, ligand exchange, and possible desorption of surface species [53]. These phenomena are affected by the deposition temperature. For instance when the temperature is too low, the adsorbed precursor molecules do not have enough energy to overcome the activation energy barrier. Therefore the reaction kinetics would be slow. On the other hand at high temperatures, precursor molecules are subject to decomposition [4], especially for precursors with large molecules, which could lead to CVD like deposition. Additionally, at high deposition temperatures the desorption rate for adsorbed species is higher which results in a slower growth [22]. These considerations often lead to a search for a suitable range of deposition temperatures; an ALD window. An ALD window, as shown schematically in Figure 1-5, defines the range of deposition temperatures at which the surface reactions have the basic requirements of an ALD reaction; most importantly self-limiting behavior.

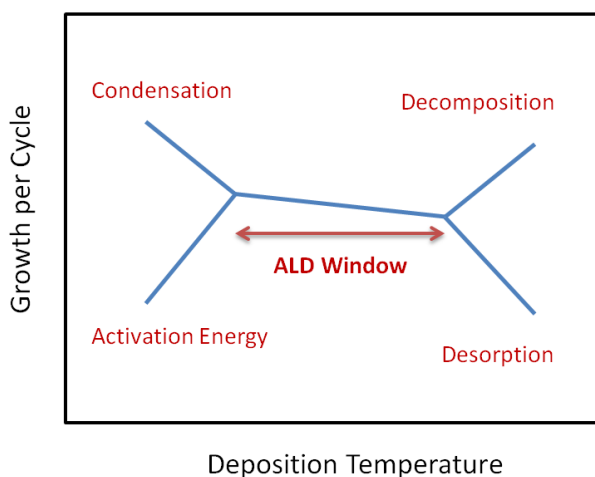


Figure 1-5 The ALD window is defined as a range of deposition temperatures that leads to ALD-type reactions.

In addition to using water as the oxygen source, oxygen plasma has been utilized in the deposition of Al_2O_3 allowing for successful depositions at temperatures as low as room temperature [12, 20, 54].

1.2.2 Hafnium Oxide

HfO_2 is another important metal oxide that has been one of the major areas of ALD research for the last decade [55-63]. The main application of HfO_2 is to replace SiO_2 as a gate oxide in MOSFETs. The MOSFET (metal oxide semiconductor field effect transistor) is the building block of CMOS (complementary metal oxide semiconductor) devices. In a MOSFET, voltage is applied across the gate oxide to control the flow of carriers in the channel as shown in Figure 1-6. SiO_2 has been used as the standard material for the past forty years. However, due to downscaling of the transistors, the SiO_2 layer has changed from 100 nm thickness in 1969 to ~2 nm by 2005 while the leakage current has increased exponentially [64]. This was a strong motivation for semiconductor industry and the ALD research community to search for suitable candidates to substitute SiO_2 . The candidate material must have high dielectric constant (higher than the 3.9 dielectric constant of SiO_2), chemical stability and good compatibility with the existing silicon-based processes. HfO_2 and ZrO_2 were two of the most important candidates with high relative permittivity (~20-25). Ultimately it led to implementation of ALD deposited Hf-based oxides in the 45-nm node in 2007 by Intel Corp. [65]. Since then, ALD has been used as a standard deposition method in fabrication of CMOS devices in the 32-nm and 22-nm nodes [66, 67]. A detailed review of the development of high-k hafnium based materials has been recently published by Choi *et al.* [68].

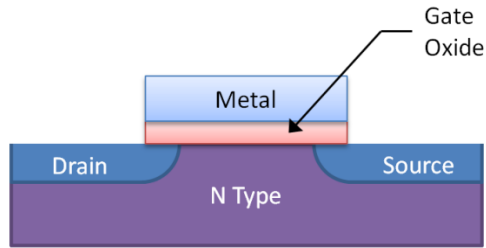


Figure 1-6 Schematic representation of a MOSFET

Different metalorganic precursors have been used in the ALD of HfO_2 including HfCl_4 [69], tetrakis(diethylamino)hafnium [62], tetrakis(dimethylamide)hafnium [57] and tetrakis(ethylmethylamide)hafnium [56]. H_2O [35, 57], O_3 [70] and plasma oxygen [71] have been used as oxygen sources.

1.2.3 Zirconium Oxide

Similar to HfO_2 , ZrO_2 has also been an interesting material for microelectronic applications. ZrO_2 is a high-k oxide. In fact, ZrO_2 and HfO_2 have very similar properties (bandgap = 5.8 eV and dielectric constant = 20-25) [72]. Zr and Hf are both from column IV in the periodic table; however, their chemical stability has been found to be slightly different. ZrO_2 is slightly unstable and could react with Si to form ZrSi_2 [72]. This is the main reason that HfO_2 is currently preferred over ZrO_2 as a gate dielectric. Research has been focused on ALD of ZrO_2 as a gate dielectric [73-75] and also as a capacitor [3, 76]. Various precursors have been developed for ALD of ZrO_2 , such as ZrCl_4 [77] and tetrakis(ethylmethylamino) zirconium [78].

1.3 Metal-Insulator-Metal Diodes

Metal-insulator-metal (MIM) diodes operate on the basis of quantum mechanical tunneling. Their simple structure consists of a thin insulating layer positioned

between two metallic electrodes. If the insulating layer is sufficiently thin (a few nanometers), current can flow between the two electrodes by means of the quantum tunneling effect [79]. MIM diodes have suitable rectifying properties. Compared to semiconductor rectifying elements, MIM diodes have very fast response time and wide bandwidth. These rectifying elements are currently the center of attention for the development of next generation antenna-coupled infrared detectors [80-82], high frequency mixers [83], and optical rectennas [84].

Figure 1-7 shows the energy band diagram for an MIM diode with similar electrodes (symmetric MIM). The relationship between current density J and applied voltage V in the intermediate voltage range ($0 < V \leq \phi/e$), can be expressed by the following equation [79]:

$$J = J_0 \left\{ \tilde{\phi} \exp\left(-A\tilde{\phi}^{-\frac{1}{2}}\right) - \tilde{\phi} + eV \times \exp\left(-A(\tilde{\phi} + eV)^{\frac{1}{2}}\right) \right\} \quad (1.3)$$

where $\tilde{\phi}$ is the mean value of the barrier height above the Fermi level of the negatively biased electrode, V is the applied voltage across the insulator layer. J_0 and A are defined with a reasonable approximation as:

$$J_0 = \left[\frac{e}{(2\pi h)} \right] \cdot \left[\frac{1}{(\Delta s)^2} \right], \quad A = \left(\frac{4\pi\Delta s}{h} \right) \cdot (2m)^{\frac{1}{2}} \quad (1.4)$$

where m and e are the mass and the charge of the electron, h is Plank's constant and Δs is the insulator thickness.

MIM diodes have been investigated by researchers since the early 1960s [81, 82, 85-89]. Early diodes were fabricated by positioning a tungsten wire on an oxidized metal surface [90]. The thin native oxide on the tungsten and the metallic surface acted as the insulating layer. Later, thin film diodes replaced the point-contact diodes [91]. MIM diodes have been fabricated using various techniques such as thermal oxidation [92-94], plasma oxidation [80, 82] and anodic oxidation [89] of metallic surfaces.

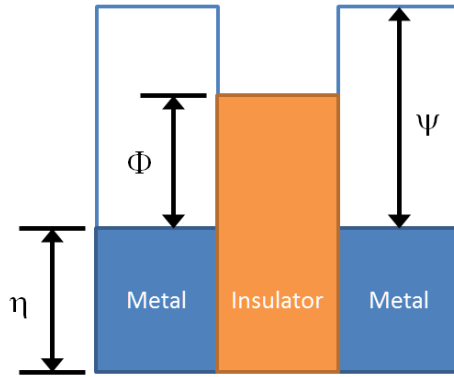


Figure 1-7 Energy diagram for a symmetric MIM diode, Φ is the barrier height, ψ is the metal work function and η is the Fermi level.

Fabrication of MIM diodes requires synthesis of an insulating layer between two metallic surfaces. The probability of quantum tunneling strongly depends on the thickness of the insulating layer. The insulating layer needs to have uniform thickness over the entire diode area in order to obtain high performance. In addition to uniformity, the fabrication process must allow for precise thickness control for reliability and reproducibility of the MIM diodes. ALD can be used to deposit thin layers of metal oxides on a metallic surface with good uniformity and thickness precision as part of the MIM fabrication process.

1.4 Thesis Objectives and Scope

The main focus of this thesis is the deposition of metal oxides on metallic substrates by ALD. There are various methods to construct an insulator film on a metal surface. In this thesis the capabilities of ALD for preparation of insulator films on metallic substrates especially for the case of ultra-thin films is studied. One of the main applications of this method would be in fabrication of MIM diodes.

In Chapter 2 the deposition of metal oxides on silicon substrates is studied. The motivation is to characterize various aspects of ALD film growth on a known

substrate. Since the main equipment used for the experiments was an integrated multi-chamber ALD research system, it was essential to explore the capabilities and options of this sophisticated tool to perform careful and precise experiments.

Chapter 3 describes the preparation of chromium thin films by DC magnetron sputtering as a main metallic substrate used in the study of ALD film growth. In this chapter it is tried to correlate the film resistivity to microstructure and also process parameters such as sputtering pressure.

Chapter 4 presents the results of *in-situ* spectroscopic ellipsometry study of ALD film growth on metallic substrates. The deposition can be performed by conventional thermal ALD or PEALD. The difference between the two methods will be discussed with an emphasis on formation of a thin native oxide as the result of exposure to oxygen plasma and the remedies to eliminate the problem caused by the presence of this interfacial layer.

In Chapter 5, the fabrication of MIM diodes using ALD is studied. MIM diodes prepared by thermal and PEALD are characterized by performing electrical measurements. The motivation is to study the suitability of ALD for fabrication of MIM diodes.

1.5 References

- [1] H. Kim, P.C. McIntyre, *J Korean Phys Soc* 48/1 (2006) 5.
- [2] K.E. Elers, T. Blomberg, M. Peussa, B. Aitchison, S. Haukka, S. Marcus, *Chemical Vapor Deposition* 12/1 (2006) 13.
- [3] M. Leskela, M. Ritala, *Angew Chem Int Ed Engl* 42/45 (2003) 5548.
- [4] R.L. Puurunen, *Journal of Applied Physics* 97/12 (2005) 121301.
- [5] T. Suntola, J. Antson, US Patent No. 4,058,430, (15 Nov. 1977).
- [6] M. Ylilammi, *Thin Solid Films* 279/1-2 (1996) 124.
- [7] S.M. George, A.W. Ott, J.W. Klaus, *J Phys Chem-US* 100/31 (1996) 13121.
- [8] G. Mazaleyrat, A. Esteve, L. Jeloica, M. Djafarirouhani, *Computational Materials Science* 33/1-3 (2005) 74.
- [9] M.D. Halls, K. Raghavachari, *J Chem Phys* 118/22 (2003) 10221.
- [10] J.S. Lee, T. Kaufman-Osborn, W. Melitz, S. Lee, A. Delabie, S. Sioncke, M. Caymax, G. Pourtois, A.C. Kummel, *The Journal of Chemical Physics* 135/5 (2011) 054705.
- [11] Y. Widjaja, C.B. Musgrave, *Appl Phys Lett* 80/18 (2002) 3304.
- [12] T.O. Kääriäinen, D.C. Cameron, *Plasma Processes and Polymers* 6/S1 (2009) S237.
- [13] H.B. Profijt, S.E. Potts, M.C.M. van de Sanden, W.M.M. Kessels, *Journal of Vacuum Science & Technology A* 29/5 (2011).
- [14] J.Y. Kim, Y. Kim, H. Jeon, *Japanese Journal of Applied Physics Part 2-Letters* 42/4B (2003) L414.
- [15] G.A. Ten Eyck, J.J. Senkevich, F. Tang, D.L. Liu, S. Pimanpang, T. Karaback, G.C. Wang, T.M. Lu, C. Jezewski, W.A. Lanford, *Chemical Vapor Deposition* 11/1 (2005) 60.
- [16] B. Hoex, J. Schmidt, P. Pohl, M.C.M. van de Sanden, W.M.M. Kessels, *Journal of Applied Physics* 104/4 (2008).

- [17] W.J. Maeng, S.J. Park, H. Kim, *J Vac Sci Technol B* 24/5 (2006) 2276.
- [18] C.W. Jeong, B.I. Lee, S.K. Joo, *Mat Sci Eng C-Bio S* 16/1-2 (2001) 59.
- [19] J.L. van Hemmen, S.B.S. Heil, J.H. Klootwijk, F. Roozeboom, C.J. Hodson, M.C.M. van de Sanden, W.M.M. Kessels, *Journal of The Electrochemical Society* 154/7 (2007) G165.
- [20] A. Niskanen, K. Arstila, M. Ritala, M. Leskelä, *Journal of The Electrochemical Society* 152/7 (2005) F90.
- [21] S.M. George, C.A. Wilson, R.K. Grubbs, *Chem Mater* 17/23 (2005) 5625.
- [22] S.M. George, *Chem Rev* 110/1 (2010) 111.
- [23] F. Lee, S. Marcus, E. Shero, G. Wilk, J. Swerts, J. Willem Maes, T. Blomberg, *IEEE/SEMI Advanced Semiconductor Manufacturing Conference*, 2007, p. 359.
- [24] D. Hausmann, Harvard University, 2002.
- [25] C.A. Wilson, R.K. Grubbs, S.M. George, *Chem Mater* 17/23 (2005) 5625.
- [26] R.A. Wind, S.M. George, *J Phys Chem A* 114/3 (2010) 1281.
- [27] R.L. Puurunen, *Applied Surface Science* 245/1-4 (2005) 6.
- [28] J.W. Lim, H.S. Park, S.W. Kang, *Journal of Applied Physics* 88/11 (2000) 6327.
- [29] R.L. Puurunen, W. Vandervorst, *Journal of Applied Physics* 96/12 (2004) 7686.
- [30] J.W. Elam, C.E. Nelson, R.K. Grubbs, S.M. George, *Thin Solid Films* 386/1 (2001) 41.
- [31] T. Aaltonen, M. Ritala, T. Sajavaara, J. Keinonen, M. Leskela, *Chem Mater* 15/9 (2003) 1924.
- [32] R.K. Grubbs, C.E. Nelson, N.J. Steinmetz, S.M. George, *Thin Solid Films* 467/1-2 (2004) 16.
- [33] L. Baker, A.S. Cavanagh, D. Seghete, S.M. George, A.J.M. Mackus, W.M.M. Kessels, Z.Y. Liu, F.T. Wagner, *Journal of Applied Physics* 109/8 (2011).

- [34] J.C. Hackley, T. Gougousi, J.D. Demaree, *Journal of Applied Physics* 102/3 (2007).
- [35] J.C. Hackley, J.D. Demaree, T. Gougousi, *Journal of Vacuum Science & Technology A* 26/5 (2008) 1235.
- [36] R.L. Puurunen, W. Vandervorst, W.F.A. Besling, O. Richard, H. Bender, T. Conard, C. Zhao, A. Delabie, M. Caymax, S. De Gendt, M. Heyns, M.M. Viitanen, M. de Ridder, H.H. Brongersma, Y. Tamminga, T. Dao, T. de Win, M. Verheijen, M. Kaiser, M. Tuominen, *Journal of Applied Physics* 96/9 (2004) 4878.
- [37] K.J. Park, D.B. Terry, S.M. Stewart, G.N. Parsons, *Langmuir* 23/11 (2007) 6106.
- [38] J. Dendooven, S.P. Sree, K. De Keyser, D. Deduytsche, J.A. Martens, K.F. Ludwig, C. Detavernier, *J Phys Chem C* 115/14 (2011) 6605.
- [39] M.M. Frank, Y.J. Chabal, M.L. Green, A. Delabie, B. Brijs, G.D. Wilk, M.-Y. Ho, E.B.O. da Rosa, I.J.R. Baumvol, F.C. Stedile, *Appl Phys Lett* 83/4 (2003) 740.
- [40] M.M. Frank, Y.J. Chabal, G.D. Wilk, *Appl Phys Lett* 82/26 (2003) 4758.
- [41] M.A. Alam, M.L. Green, *Journal of Applied Physics* 94/5 (2003) 3403.
- [42] M.D. Groner, J.W. Elam, F.H. Fabreguette, S.M. George, *Thin Solid Films* 413/1-2 (2002) 186.
- [43] P. Saint-Cast, J. Benick, D. Kania, L. Weiss, M. Hofmann, J. Rentsch, R. Preu, S.W. Glunz, *IEEE Electr Device L* 31/7 (2010) 695.
- [44] A. Paranjpe, S. Gopinath, T. Omstead, R. Bubber, *Journal of The Electrochemical Society* 148/9 (2001) G465.
- [45] T.M. Mayer, J.W. Elam, S.M. George, P.G. Kotula, R.S. Goeke, *Appl Phys Lett* 82/17 (2003) 2883.
- [46] S.K. Kim, C.S. Hwang, *Journal of Applied Physics* 96/4 (2004) 2323.
- [47] E.P. Gusev, M. Copel, E. Cartier, I.J.R. Baumvol, C. Krug, M.A. Gribelyuk, *Appl Phys Lett* 76/2 (2000) 176.
- [48] S. Jakschik, U. Schroeder, T. Hecht, G. Dollinger, A. Bergmaier, J.W. Bartha, *Mat Sci Eng B-Solid* 107/3 (2004) 251.

- [49] H. Seidl, M. Gutsche, U. Schroeder, A. Birner, T. Hecht, S. Jakschik, J. Luetzen, M. Kerber, S. Kudelka, T. Popp, A. Orth, H. Reisinger, A. Saenger, K. Schupke, B. Sell, International Electron Devices 2002 Meeting, Technical Digest (2002) 839.
- [50] A. Rahtu, T. Alaranta, M. Ritala, Langmuir 17/21 (2001) 6506.
- [51] J.D. Ferguson, A.W. Weimer, S.M. George, Chem Mater 16/26 (2004) 5602.
- [52] S.Y. No, D. Eom, C.S. Hwang, H.J. Kim, Journal of The Electrochemical Society 153/6 (2006) F87.
- [53] M. Deminsky, Surface Science 549/1 (2004) 67.
- [54] S.E. Potts, W. Keuning, E. Langereis, G. Dingemans, M.C.M. van de Sanden, W.M.M. Kessels, Journal of The Electrochemical Society 157/7 (2010) P66.
- [55] M. Ritala, M. Leskela, L. Niinisto, T. Prohaska, G. Friedbacher, M. Grasserbauer, Thin Solid Films 250/1-2 (1994) 72.
- [56] K. Kukli, M. Ritala, T. Sajavaara, J. Keinonen, M. Leskela, Chemical Vapor Deposition 8/5 (2002) 199.
- [57] K. Kukli, T. Pilvi, M. Ritala, T. Sajavaara, J. Lu, M. Leskela, Thin Solid Films 491/1-2 (2005) 328.
- [58] X.Y. Liu, S. Ramanathan, A. Longdergan, A. Srivastava, E. Lee, T.E. Seidel, J.T. Barton, D. Pang, R.G. Gordon, Journal of The Electrochemical Society 152/5 (2005) L9.
- [59] V. Sammelselg, R. Rammula, J. Aarik, A. Kikas, K. Kooser, T. Kaambre, Journal of Electron Spectroscopy and Related Phenomena 156-158 (2007) 150.
- [60] R. Luptak, J.M.J. Lopes, S. Lenk, B. Hollander, E.D. Ozben, A.T. Tiedemann, M. Schnee, J. Schubert, S. Habicht, S. Feste, S. Mantl, U. Breuer, A. Besmehn, P.K. Baumann, M. Heuken, AVS, 2011, p. 01A301.
- [61] M. Tallarida, K. Karavaev, D. Schmeisser, AVS, Berlin, Germany, 2009, p. 300.
- [62] A. Deshpande, R. Inman, G. Jursich, C. Takoudis, Journal of Vacuum Science & Technology A 22/5 (2004) 2035.

- [63] M. Cho, J.H. Kim, C.S. Hwang, H.-S. Ahn, S. Han, J.Y. Won, *Appl Phys Lett* 90/18 (2007) 182907.
- [64] Y.C. Yeo, T.J. King, C.M. Hu, *IEEE T Electron Dev* 50/4 (2003) 1027.
- [65] K. Mistry, C. Allen, C. Auth, B. Beattie, D. Bergstrom, M. Bost, M. Brazier, M. Buehler, A. Cappellani, R. Chau, C.H. Choi, G. Ding, K. Fischer, T. Ghani, R. Grover, W. Han, D. Hanken, M. Hattendorf, J. He, J. Hicks, R. Huessner, D. Ingerly, P. Jain, R. James, L. Jong, S. Joshi, C. Kenyon, K. Kuhn, K. Lee, H. Liu, J. Maiz, B. McIntyre, P. Moon, J. Neiryneck, S. Pei, C. Parker, D. Parsons, C. Prasad, L. Pipes, M. Prince, P. Ranade, T. Reynolds, J. Sandford, L. Schifren, J. Sebastian, J. Seiple, D. Simon, S. Sivakumar, P. Smith, C. Thomas, T. Troeger, P. Vandervoorn, S. Williams, K. Zawadzki, 2007 IEEE International Electron Devices Meeting, Vols 1 and 2 (2007) 247.
- [66] S. Natarajan, M. Armstrong, M. Bost, R. Brain, M. Brazier, C.H. Chang, V. Chikarmane, M. Childs, H. Deshpande, K. Dev, G. Ding, T. Ghani, O. Golonzka, W. Han, J. He, R. Heussner, R. James, I. Jin, C. Kenyon, S. Klopacic, S.H. Lee, M. Liu, S. Lodha, B. McFadden, A. Murthy, L. Neiberg, J. Neiryneck, P. Packan, S. Pae, C. Parker, C. Pelto, L. Pipes, J. Sebastian, J. Seiple, B. Sell, S. Sivakumar, B. Song, K. Tone, T. Troeger, C. Weber, M. Yang, A. Yeoh, K. Zhang, *Int. El. Devices Meeting* (2008) 941.
- [67] M. Verghese, J.W. Maes, N. Kobayashi, *Solid State Technol* 53/10 (2010) 18.
- [68] J.H. Choi, Y. Mao, J.P. Chang, *Materials Science and Engineering: R: Reports* 72/6 (2011) 97.
- [69] H. Kim, P.C. McIntyre, C.O. Chui, K.C. Saraswat, S. Stemmer, *Journal of Applied Physics* 96/6 (2004) 3467.
- [70] R. Katamreddy, R. Inman, G. Jursich, A. Soulet, C. Takoudis, *Journal of Materials Research* 22/12 (2007) 3455.
- [71] P.K. Park, J.S. Roh, B.H. Choi, S.W. Kang, *Electrochem Solid St* 9/5 (2006) F34.
- [72] J. Robertson, *Eur Phys J-Appl Phys* 28/3 (2004) 265.
- [73] C.L. Dezelah, J. Niinisto, K. Kukli, F. Munnik, J. Lu, M. Ritala, M. Leskela, L. Niinisto, *Chemical Vapor Deposition* 14/11-12 (2008) 358.
- [74] M. Copel, M. Gribelyuk, E. Gusev, *Appl Phys Lett* 76/4 (2000) 436.

- [75] Y. Wong, K. Cheong, *Journal of Materials Science: Materials in Electronics* 21/10 (2010) 980.
- [76] H.J. Cho, Y.D. Kim, D.S. Park, E. Lee, C.H. Park, J.S. Jang, K.B. Lee, H.W. Kim, Y.J. Ki, I.K. Han, Y.W. Song, *Solid State Electron* 51/11–12 (2007) 1529.
- [77] J. Aarik, A. Aidla, H. Mandar, T. Uustare, V. Sammelselg, *Thin Solid Films* 408/1-2 (2002) 97.
- [78] S.J. Yun, J.W. Lim, J.H. Lee, *Electrochem Solid St* 7/12 (2004) F81.
- [79] J.G. Simmons, *Journal of Applied Physics* 34/9 (1963) 2581.
- [80] B. Tiwari, J.A. Bean, G. Szakmany, G.H. Bernstein, P. Fay, W. Porod, *J Vac Sci Technol B* 27/5 (2009) 2153.
- [81] P. Esfandiari, G. Bernstein, P. Fay, W. Porod, B. Rakos, A. Zarandy, B. Berland, L. Boloni, G. Boreman, B. Lail, B. Monacelli, A. Weeks, *Infrared Technology and Applications XXXI, Pts 1 and 2* 5783 (2005) 470.
- [82] P.C.D. Hobbs, R.B. Laibowitz, F.R. Libsch, *Appl Optics* 44/32 (2005) 6813.
- [83] I. Wilke, W. Herrmann, F.K. Kneubuhl, *Appl Phys B-Lasers O* 58/2 (1994) 87.
- [84] R. Corkish, M.A. Green, T. Puzzer, *Sol Energy* 73/6 (2002) 395.
- [85] J.C. Fisher, I. Giaever, *Journal of Applied Physics* 32/2 (1961) 172.
- [86] J.G. Simmons, *Journal of Applied Physics* 34/6 (1963) 1793.
- [87] A. Sanchez, C.F. Davis, K.C. Liu, A. Javan, *Journal of Applied Physics* 49/10 (1978) 5270.
- [88] F.K. Kneubuhl, C. Fumeaux, W. Herrmann, H. Rothuizen, *Infrared Phys Techn* 39/3 (1998) 123.
- [89] P.A. Parilla, P. Periasamy, J.J. Berry, A.A. Dameron, J.D. Bergeson, D.S. Ginley, R.P. O'Hayre, *Adv Mater* 23/27 (2011) 3080.
- [90] L.O. Hocker, D.R. Sokoloff, V. Daneu, A. Szoke, A. Javan, *Appl Phys Lett* 12/12 (1968) 401.

- [91] S.Y. Wang, T. Izawa, T.K. Gustafson, Appl Phys Lett 27/9 (1975) 481.
- [92] G.M. Elchinger, A. Sanchez, C.F. Davis, A. Javan, Journal of Applied Physics 47/2 (1976) 591.
- [93] M. Heiblum, S. Wang, J.R. Whinnery, T.K. Gustafson, IEEE J Quantum Elect 14/3 (1978) 159.
- [94] E.N. Grossman, T.E. Harvey, C.D. Reintsema, Journal of Applied Physics 91/12 (2002) 10134.

Chapter 2 Characterization of ALD Oxides

2.1 Introduction

Metal oxides are an important category of materials that have been deposited by atomic layer deposition (ALD). They have a wide range of applications including dielectric layers in electroluminescent thin film displays [1-3], gate oxide layers in MOS transistors [4-6], capacitors in DRAM applications [7-9], wear-resistance coating for MEMS devices [10] and insulator layers in metal-insulator-metal (MIM) devices. Successful preparation of metal oxides by ALD requires selection of suitable chemical precursors and optimum process parameters such as deposition temperature and precursor pulse length. The relation between the ALD process parameters and thin film properties has been the subject of extensive research in the ALD community since its early days. Various characterization techniques have been used to study ALD thin films. Techniques such as transmission electron microscopy (TEM), atomic force microscopy (AFM), Rutherford backscattering spectroscopy (RBS), x-ray photoelectron spectroscopy (XPS), Auger electron spectroscopy (AES) and x-ray diffraction and reflectometry (XRD and XRR) have been used to study the thickness, morphology, density, composition, microstructure and crystallinity of ALD thin films [11-15]. Electrical properties of ALD films have been also the subject of

interest for applications in microelectronics. Current-voltage (IV) and capacitance-voltage (CV) measurements have been used to study various electrical properties of thin ALD films including current leakage, capacitance density and dielectric strength of thin dielectric oxides [16, 17]. Recently, *in-situ* characterization tools have attracted the attention of researchers since they allow for online process monitoring and control of the deposition process at the atomic scale [18]. The quartz crystal microbalance (QCM) has been a valuable tool to study the growth of ALD films. QCM can be used to monitor the mass gained after each half ALD cycle [19, 20]. However, there are some limitations associated with this measurement technique. For instance, the actual film deposition on the substrate could be different from the deposition on the quartz crystal due to effects of substrate on the initial stages of ALD film nucleation and growth. Additionally, the QCM needs to be heated to emulate the conditions of the actual substrate. Another monitoring tool to study the ALD film growth is *in-situ* spectroscopic ellipsometry. It is considered as a powerful and versatile tool to study various aspects of ALD film growth [18].

In this research, various characterization tools were employed to study the properties of aluminum oxide, hafnium oxide and zirconium oxide films deposited by ALD.

2.2 Experimental Procedures

2.2.1 The ALD Research System

The depositions were carried out in an ALD-150 integrated research system from Kurt J. Lesker Company. This integrated system had an ALD reactor with dual thermal and remote plasma capability, as well as an *in-situ* spectroscopic ellipsometer. The design incorporated a sample preparation unit attached to the ALD reactor via a load-lock unit that allowed for treatment of the substrate before and after the ALD process. This is shown schematically in Figure 2-1. An actual

picture of the ALD system and a cross section view of the ALD chamber are shown in Figure 2-2 and Figure 2-3, respectively.

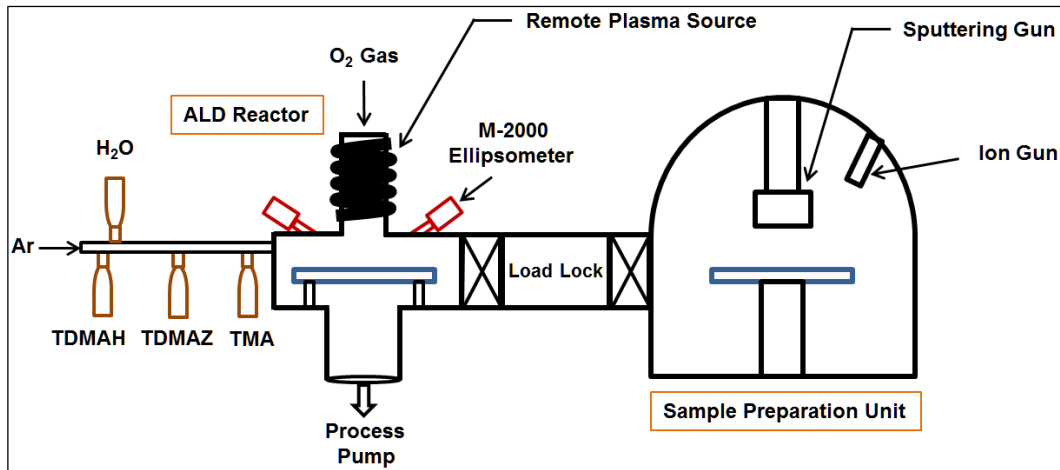


Figure 2-1 Schematic representation of the ALD research system.

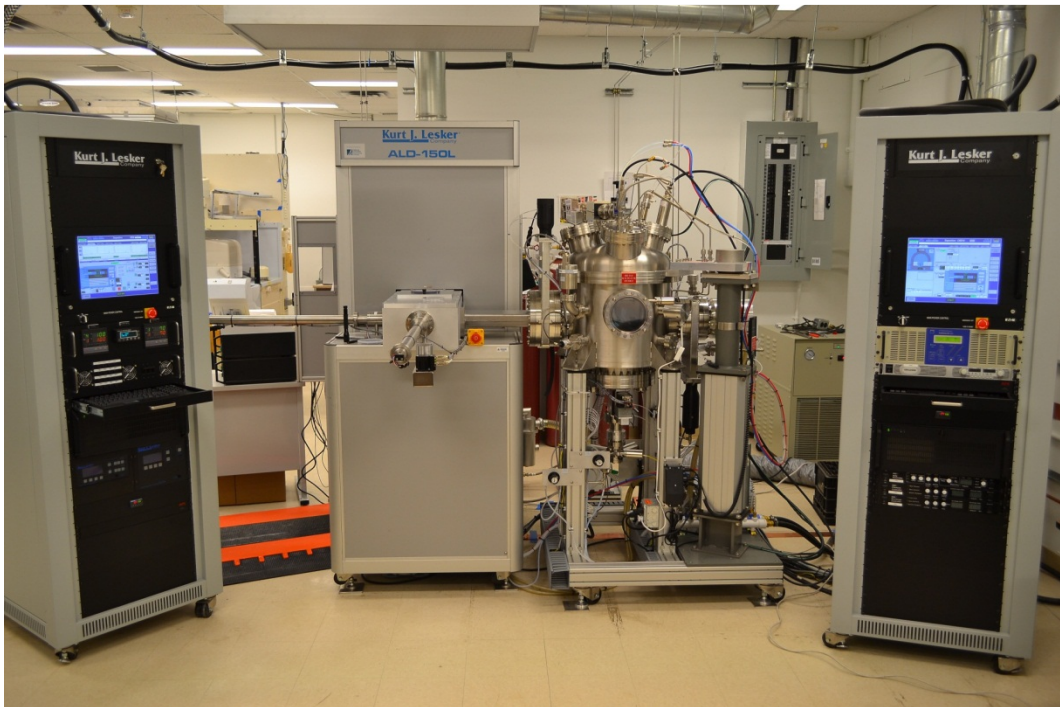


Figure 2-2 View of the ALD research system.

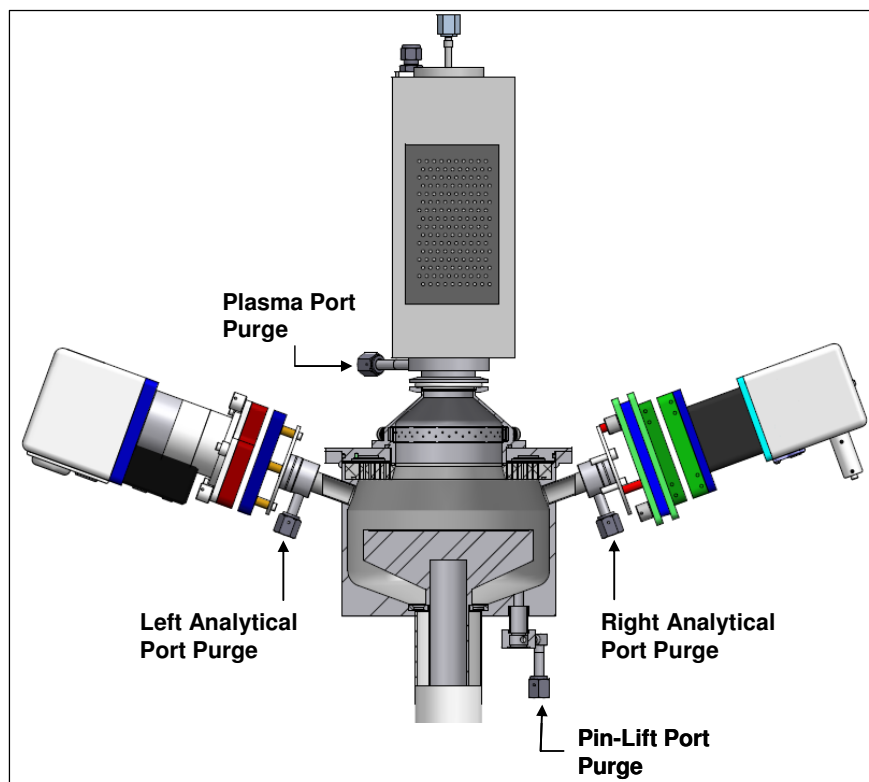


Figure 2-3 Cross section view of the ALD chamber.

The substrate surface can be cleaned *in-situ* using an ion source in the sample preparation chamber. The ion source can be also used to remove the native oxide formed on the surface of metals or semiconductors. The ion source can operate at a maximum power of 300 W producing Ar ions with kinetic energies in the range of approximately 50 to 250 eV. In addition to the *in-situ* cleaning and etching capabilities, the sample preparation unit has a sputtering source that is used to deposit metallic thin films. The sputtering source has a DC magnetron gun with a maximum power of 2 kW.

The plasma source was an inductively-coupled remote plasma source operated at a total pressure of 0.9-1.5 torr and a power of 150-600 W. A constant stream of high purity argon gas was flowed through the plasma source. Oxygen or nitrogen as reactant gases were added to the argon stream using a mass flow controller when the plasma source was operational. The plasma RF power and plasma

pressure must be chosen with care in order to obtain a dense contained plasma. For a given plasma pressure, the power must be high enough for the plasma to operate in the electromagnetic mode (H-mode) [21]. The combination of low power and high pressure usually leads to a faint electrostatic (E) mode, which should be avoided during plasma-enhanced ALD (PEALD). The effect of plasma power and pressure on the operational mode of the oxygen plasma is shown in Figure 2-4. The plasma in Figure 2-4a, operated at 300 W and an oxygen flow of 60 sccm, showed a faint spread discharge, the characteristics of the E-mode. Increasing the power to 600 W moved the plasma into the H-mode, as identified by a bright contained glow (Figure 2-4b). Figure 2-4c and d show the plasma operated in the H-mode at lower powers and low oxygen flow rates.

The ALD chamber was equipped with an advanced precursor delivery system consisting of four chemical precursors, water and plasma gas. Three metalorganic precursors were used in the experiments: trimethylaluminum (TMA), tetrakis(dimethylamino) hafnium (TDMAH) and tetrakis(dimethylamide) zirconium (TDMAZ) to deposit Al_2O_3 , HfO_2 and ZrO_2 , respectively. The precursors were stored in ampules (25 gr) purchased from Sigma-Aldrich. Reactant vapors were generated by vaporization of precursors in the liquid phase. During precursor dosing, carrier/purge flow is used as a carrier gas to assist in mass transport of reactant vapor to chamber. High purity argon was used as the carrier gas. Between doses, the argon flow acts as purge gas to remove the excess reactants and by-products from the chamber.

Lightly doped silicon wafers (Si 100) were used as the substrate material. The wafers were cleaned by immersing into a Piranha solution (3:1 mixture of sulfuric acid and hydrogen peroxide) for 15 minutes. The wafers were then cut into rectangular pieces (approximately 2x2 cm).

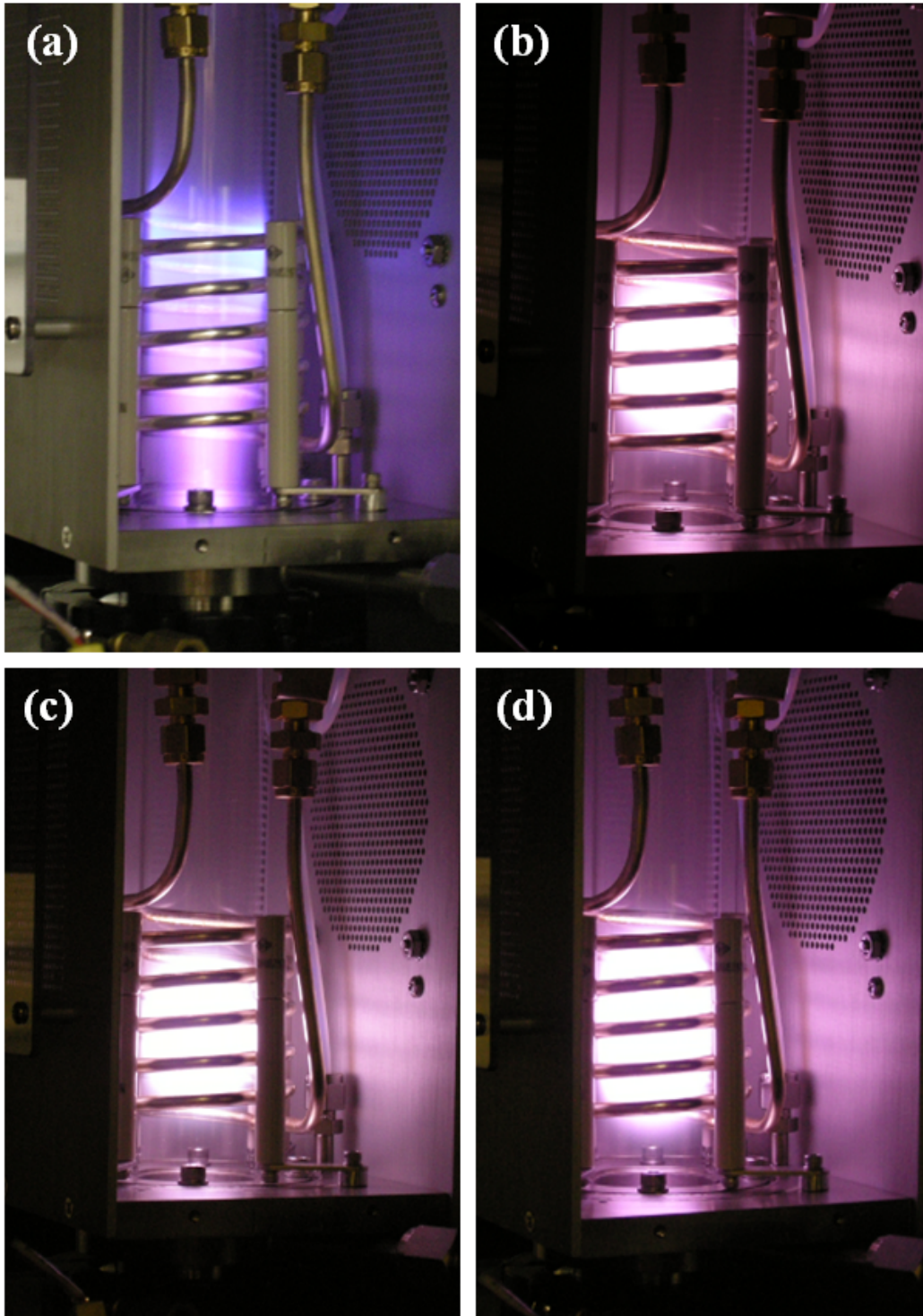


Figure 2-4 Discharge glow from the oxygen plasma at various plasma powers and oxygen flow rates. (a) 300 W, 60 sccm O₂; (b) 600 W, 60 sccm O₂; (c) 300 W, 20 sccm O₂; (d) 150 W, 5 sccm O₂.

2.2.2 *In-Situ* Spectroscopic Ellipsometry

Ellipsometry is an optical technique that has been widely used for precise determination of the film thickness and optical properties [22]. It measures the change in the polarized light upon reflection (or transmission) from the sample. The measurement is performed by sending a beam of light with a known polarization using a polarizer toward the sample and determining its output polarization using a rotating analyzer as shown schematically in Figure 2-5. In an ellipsometry measurement, two parameters are measured: the amplitude ratio Ψ and phase angle Δ [22]. These parameters are defined by the amplitude ratio of the amplitude reflection coefficients for p- and s-polarizations based on the following equation:

$$\rho = \frac{r_p}{r_s} = \tan \Psi e^{i\Delta} \quad (2.1)$$

where r_p and r_s are the amplitude reflection coefficients and ρ is the complex reflectance ratio [18]. The measured values are compared to the values generated by an optical model loaded with guessed values of thickness and optical constants. The optical parameters are adjusted iteratively until the model produces Ψ and Δ values that are closest to the measured Ψ and Δ . This analysis results in indirect determination of film thickness as well as optical properties.

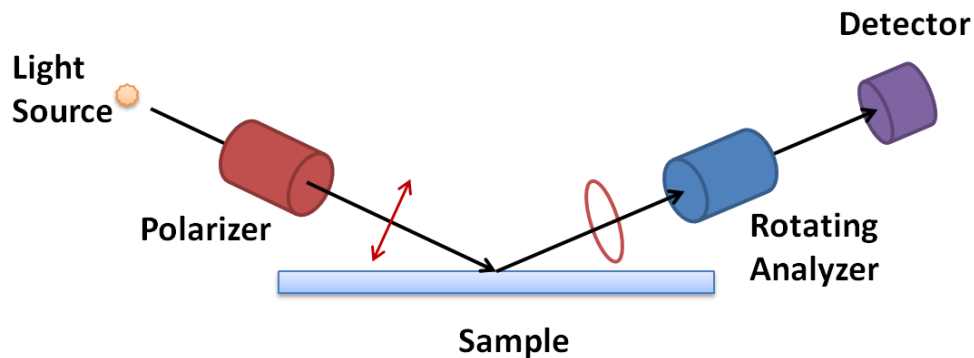


Figure 2-5 Typical components of an ellipsometry measurement equipment.

Ellipsometry measurements can be performed at one single wavelength or over a spectral range (spectroscopic ellipsometry) to increase accuracy and determination of optical constants at different wavelengths. The ellipsometry tool used in the presented research was a J. A. Woollam M-2000DI with a wide spectral range of 193 to 1700 nm (0.73 to 6.43 eV) and is capable of simultaneous CCD detection of all wavelengths with a fast data acquisition speed of 20 dispersion measurements per second.

2.2.3 Composition Analysis

X-ray photoelectron spectroscopy (XPS) analysis was performed using a Kratos Analytical AXIS-165 spectrometer at the Alberta Centre for Surface Engineering and Science (ACSES). The base pressure in the analytical chamber was lower than 3×10^{-8} Pa. A monochromatic Al K α ($h\nu = 1486.6$ eV) source was used at a power of 210 W. Survey spectra were collected for binding energies ranging from 1100 to 0 eV with a pass energy (PE) of 160 eV and a step of 0.35 eV. High-resolution spectra were measured with a PE of 20 eV and a step of 0.1 eV. To remove surface contamination, samples were sputter etched for 2 min. The analysis of the data was performed by Casa XPS software.

2.3 Results and Discussion

2.3.1 Optical Characterization

In-situ spectroscopic ellipsometry was employed to study the effects of key ALD process parameters on the optical properties of thin metal oxide films. Figure 2-6 shows a typical ellipsometry result from an experiment that involves deposition of aluminum oxide by means of thermal ALD on a silicon substrate at 100°C. As can be seen in the graph, a linear relationship exists between the thickness and the

number of cycles. The slope of the growth curve represents the added thickness after each cycle or so called ‘growth per cycle’ (GPC). In this case, a GPC of 0.83 Å/cycle is obtained for the deposition of Al₂O₃.

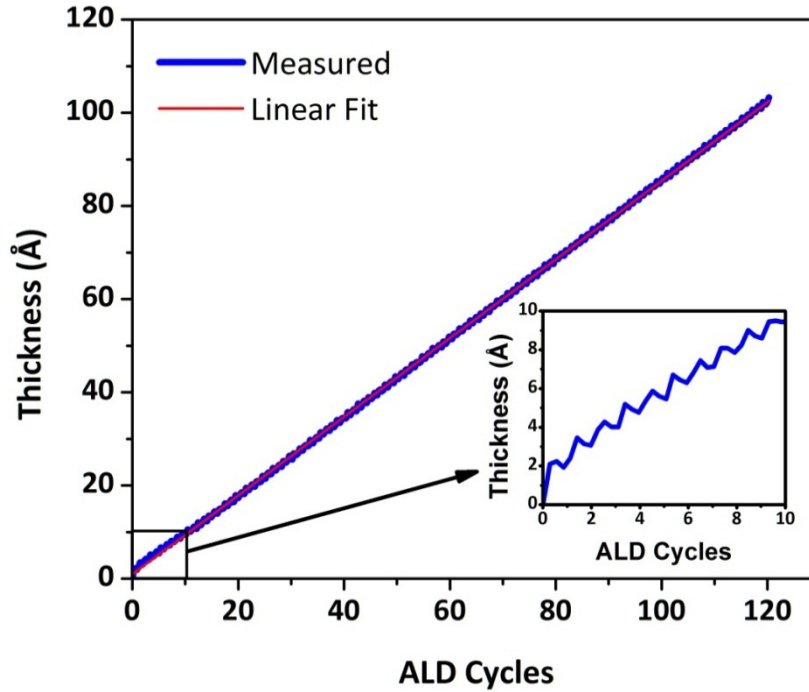


Figure 2-6 Thermal ALD growth of aluminum oxide on Si substrate.

The inset graph in Figure 2-6 depicts a more detailed view of the growth of Al₂O₃ during the first few cycles. A close look at the growth curve indicates it actually has a saw-tooth shape that is repeated after each cycle. The tooth-saw shape is caused by the change in film thickness during each ALD cycle. Since the data acquisition occurred every 4.37 s, the *in-situ* ellipsometry was not able to capture all the changes during each ALD cycle. Figure 2-7 schematically shows the changes during one ALD cycle. Each ALD cycle starts with a small dose (20 ms) of metalorganic precursor (TMA for Al₂O₃) that is adsorbed on the surface, as shown by phase A in the figure. Once the second reactant, in this case water, enters the deposition chamber, it chemically reacts with the absorbed TMA

molecules and the by-products (CH_4) are released. The reduction of thickness in the second half-cycle is attributed to the release of byproducts. The net amount of material gained after each cycle is linked with the GPC. Due to limitations of the ellipsometry data acquisition speed, a saw-tooth shape is recorded, as shown by the red dotted line.

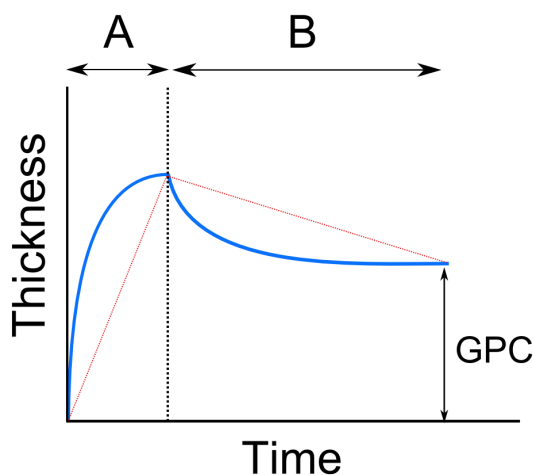


Figure 2-7 Thickness variation during a single ALD cycle consisting of two half-cycles. In phase A, precursor molecules (TMA) are adsorbed on the surface. In the second half-cycle, B, water reacts with the TMA molecules releasing the byproducts. The red dashed line indicates the thickness variation as measured by ellipsometry.

The data acquisition speed can be increased at the expense of increasing the noise level. Additionally, the purge time can be set to longer values to allow the ellipsometer to measure more data points during each ALD cycle. The graphs shown in Figure 2-8 demonstrate the power that *in-situ* monitoring provides for studying the growth of ALD films. The graph on the left shows 6 ALD cycles each consisting of a 20 ms TMA pulse, 10 s purge, 0.5 s water pulse, and 10 s purge during the growth of Al_2O_3 . Compared to the graphs in Figure 2-6, this growth curves provides a clearer view of the variations during each ALD cycles. To improve the signal to noise ratio, the variations can be averaged over a few cycles. Figure 2-8b shows the result of such statistical operation.

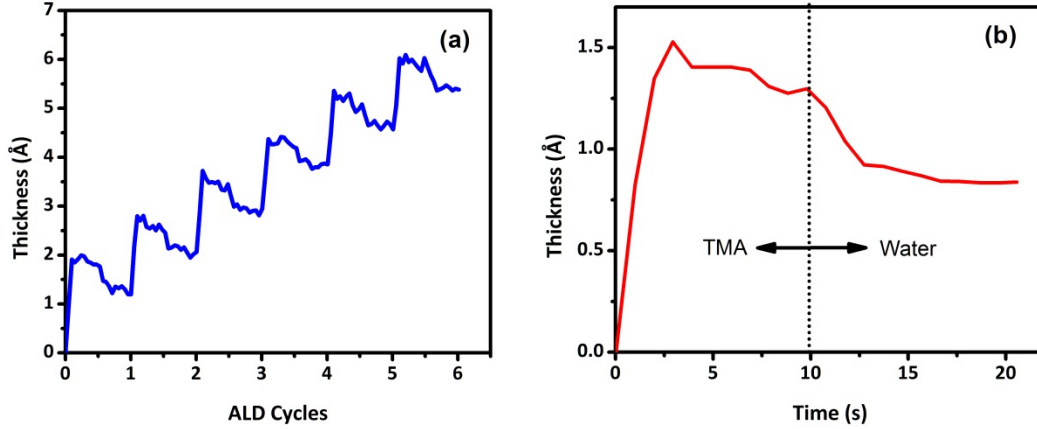


Figure 2-8 Increasing the speed of data acquisition to 1 s and increasing the purge time to 10 s gave a clearer view of the thickness variation during each ALD cycle (a). Thickness variation in one single cycle was obtained by averaging the changes over 10 cycles (b).

Figure 2-9a shows measured and generated ellipsometry parameters, Ψ and Δ versus wavelength (λ) for a 10 nm Al_2O_3 layer on a Si substrate from the ellipsometry software. The thickness and optical constants of the layer were iteratively changed to obtain the best fit for the modeled data. A very good fit with a small mean square error (MSE) is observed which is typical for insulating oxides on well-known substrates such as single crystal silicon. A Cauchy model was used to generate the ellipsometry data used for the fitting iteration. The Cauchy model is a simple empirical optical model that can describe the optical constants of transparent materials based on the following equation [22]:

$$n(\lambda) = A_n + \frac{B_n}{\lambda^2} + \frac{C_n}{\lambda^4} + \dots, k = 0 \quad (2.2)$$

where n is the refractive index, k is the extinction coefficient, λ is the wavelength and A , B , C , etc., are the coefficients determined empirically for a material by fitting the equation to measured refractive indices at known wavelengths. Usually, only two coefficients are used to describe the relationship between wavelength and refractive index. In order to relate the optical constants from the Cauchy model to the measured ellipsometry data (Ψ and Δ), the film thickness is used. If the film thickness is already known from other independent measurements such as stylus profilometry, the Cauchy model can be used to determine the optical

constants of the film. However, if both the optical constants and the thickness are unknown, the iteration should also involve the thickness as a fitting parameter. It is important to note that the film thickness needs to be large enough ($>10\text{nm}$) to minimize the error associated with correlation of optical constants with thickness. The optical constants of Al_2O_3 deposited by thermal ALD at 100°C are shown in Figure 2-9b. The A and B coefficients in the Cauchy model were determined to be 1.598 and $0.0088 \mu\text{m}^2$, respectively.

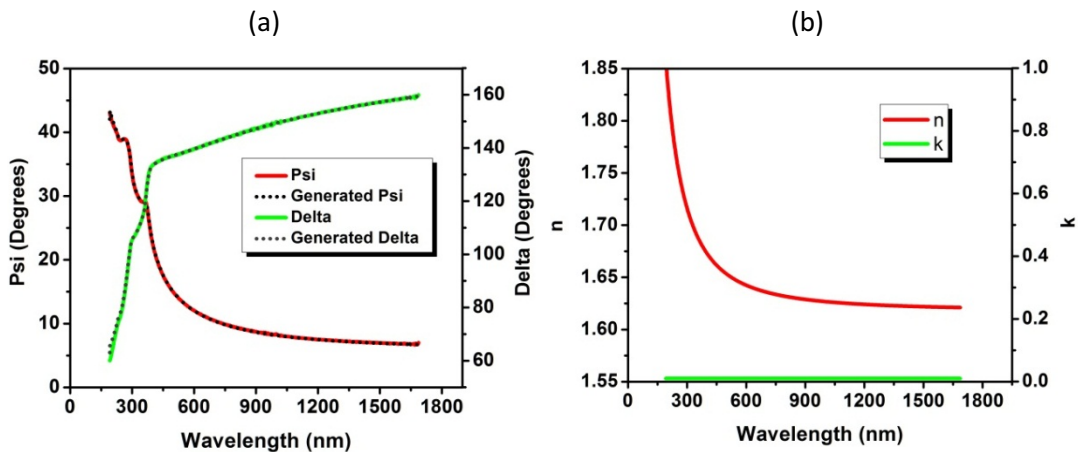


Figure 2-9 Ellipsometry data from deposition of Al_2O_3 on Si substrate: (a) Psi and Delta parameters obtained from 10-nm Al_2O_3 layer; (b) optical constants of Al_2O_3 based on Cauchy model.

The accuracy of ellipsometry measurement, especially for the cases where both the optical constants and thickness are unknown, can be improved by means of parameter coupling that is best performed using *in-situ* monitoring during the film growth. For linear film growth, the film thickness is linearly linked to the number of cycles. For instance, if the actual film thickness is 75 \AA after 50 cycles, then the thickness must become 150 \AA and 225 \AA after 100 cycles and 150 cycles, respectively. By coupling thickness with the number of cycles, it is possible to minimize the correlation of thickness with optical constants and therefore increase the accuracy of the measurements.

As discussed earlier, the *in-situ* ellipsometry technique can be used to accurately determine both the optical constants and the thickness of the ALD films. The measured thickness is then used to determine the growth per cycle for the ALD process used. Figure 2-10 illustrates the effect of deposition temperature on the GPC for ALD of Al_2O_3 in thermal and PEALD modes. It can be seen that the GPC during PEALD of Al_2O_3 monotonically decreases with increasing substrate temperature from 50°C to 300°C . This is mainly caused by a decrease in incorporation of aluminum atoms into the films during each ALD cycle [23]. The incorporation of aluminum atoms is directly related to the density of hydroxyl groups on the substrate surface that act as adsorption sites for TMA molecules. The surface density of hydroxyl groups decreases with increasing temperature causing the GPC to drop at higher deposition temperatures (Figure 2-11) [24]. It is also observed that the thermal ALD of Al_2O_3 shows a lower GPC compared to PEALD over the deposition range of 100°C to 300°C . At 300°C , the difference in GPC is relatively small; however, at lower temperatures the difference is more prominent.

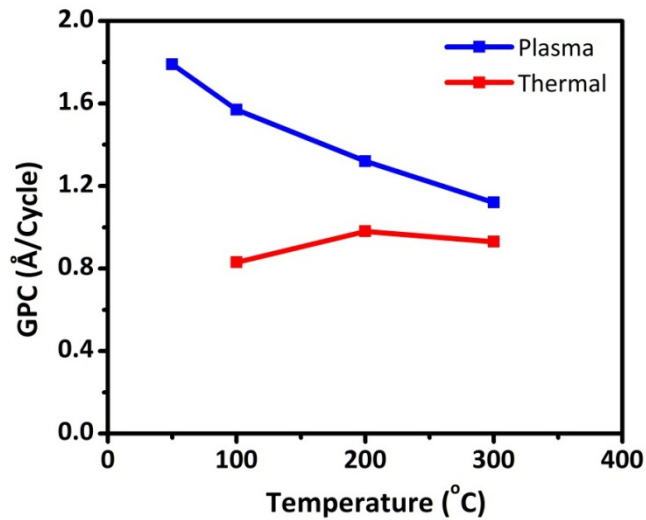


Figure 2-10 The dependence of growth per cycle on the deposition temperature for ALD of Al_2O_3 in thermal and plasma-enhanced modes.

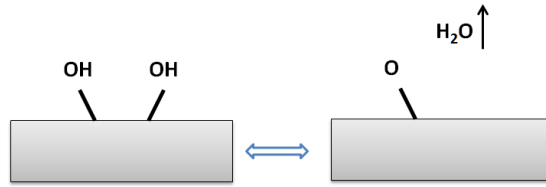


Figure 2-11 Desorption of hydroxyl groups. As the substrate temperature increases, the rate of OH desorption also increases resulting in lower available reaction sites on the surface.

At lower temperatures, the thermal energy is insufficient for the complete reaction of H_2O with the adsorbed surface species, which results in low growth per cycle values. The lower limit for thermal ALD of Al_2O_3 has been reported to be 100°C [25]. At deposition temperatures lower than 100°C , the films have lower density and contain large amount of impurities, mostly carbon and hydrogen. On the other hand, deposition at temperatures higher than 350°C will result in decomposition of TMA and CVD-like growth [16]. Therefore, a temperature range of 100°C to 300°C was chosen as a temperature window suitable for deposition of Al_2O_3 in both the thermal and plasma-enhanced modes.

The refractive index of aluminum oxide films deposited at two temperature limits are presented in Table 2-1. The refractive index for these amorphous films is lower than the refractive index of crystalline alumina ($n=1.76$ at 633 nm). However, it agrees with reported values for ALD aluminum oxide films ($n=1.63$ to $n=1.67$) [25-27]. The variation has been reported to be caused by the change in hydrogen levels in the films [27]. As the deposition temperature increases, the amount of hydrogen incorporated into the film decreases and as a result, a higher refractive index is observed. At higher temperatures, thermal and plasma-enhanced ALD seem to produce similar results in terms of optical properties. It is only at lower temperatures (100°C and lower) that the difference is more apparent.

Table 2-1 Refractive index of Al₂O₃ films at 633 nm deposited by thermal and plasma-enhanced ALD at 100°C and 300°C

| ALD Mode | 100°C | 300°C |
|------------------------|--------------|--------------|
| Thermal | 1.64 | 1.68 |
| Plasma-Enhanced | 1.65 | 1.68 |

Table 2-2 summarizes the main process parameters for the ALD of aluminum oxide in the ALD-150 research system. It can be seen that the ALD of aluminum oxide can be achieved by very fast ALD cycles (in the range of 8-15 s). The short cycles are the result of the small volume and high efficiency of the ALD chamber. The TMA precursor pulse width is only 20 ms. Increasing the TMA pulse would have no significant effect on the GPC which indicates the substrate surface is saturated by such a short dose. On the other hand, a relatively longer dose is required for water or oxygen plasma for the surface reactions to complete. The main difference in the cycle timing of the thermal and plasma modes are in the second purge duration (that is the carrier gas purge after the water or plasma pulse). Due to its polar nature, water requires longer purge times to completely desorb from the chamber walls and leave the chamber after each pulse. This becomes more problematic at lower deposition temperatures where longer purge times are needed [13].

Table 2-2 Operating conditions for ALD of aluminum oxide in thermal and plasma-enhanced ALD modes

| Parameter | Thermal ALD | Plasma-Enhanced ALD |
|---|--------------------|----------------------------|
| TMA pulse | 20 ms | 20 ms |
| The first purge time | 5 s | 5 s |
| H₂O or O₂ plasma pulse | 0.5 s | 0.5-2 s |
| The second purge time | 10 s | 2 s |
| Plasma power | - | 600 W |
| Precursor container temperature | 25 °C | 25 °C |
| ALD temperature window | 100-300 °C | 25-300 °C |
| Operating pressure | ~ 1 torr | ~ 1 torr |

Unlike thermal ALD, PEALD does not require long purge times and, as a result, the total cycle time is considerably shorter. However, the plasma pulse length can affect the growth characteristics. Figure 2-12 demonstrates the effect of oxygen plasma exposure time on the GPC of Al_2O_3 deposition at 100°C . As seen in the figure, the GPC gradually decreases as the plasma pulse increases. It is expected that the GPC either increases or remains constant (if the saturation is already achieved) when a longer plasma pulse duration is applied. In this case, it seems that the saturation is achieved within a very short time (< 1 s); however, the lower observed GPC at longer exposure times is caused by the removal of surface species as a result of plasma ion bombardment. The typical plasmas used in ALD reactors are known to have ions with kinetic energies from 20-40 eV which can produce damage once they reach the substrate surface [23]. Although the ions reaching the surface have relatively small kinetic energy, they still can remove loosely-bound surface species that results in smaller amount of material deposited at each ALD cycle. In order to ensure complete saturation and also minimize the plasma-induced damage, a plasma exposure duration of 0.5-2 s was used in the experiments.

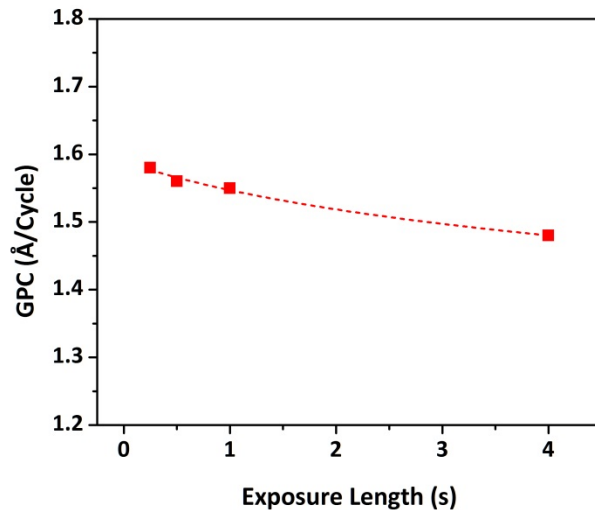


Figure 2-12 Variation of GPC as a function of oxygen plasma exposure length in deposition of Al_2O_3 . The GPC decreases when longer plasma pulses are used that is attributed to the plasma etching ability.

Fourier transform infrared spectroscopy (FTIR) is another optical technique that has been widely used to characterize ALD films [28-31]. The sensitivity of FTIR allows for detection of very thin films, even monolayers. Figure 2-13 shows the FTIR spectra for Al₂O₃ films on Si substrates. Al₂O₃ shows a characteristic peak at 950 wavenumber caused by Al-O stretching vibration. The intensity of this peak is related to film thickness as seen in the figure. Plotting the peak intensity as a function of film thickness, as illustrated in Figure 2-14, reveals that a linear relation exists between the peak intensity and the thickness. However, this might not be true for much thicker films.

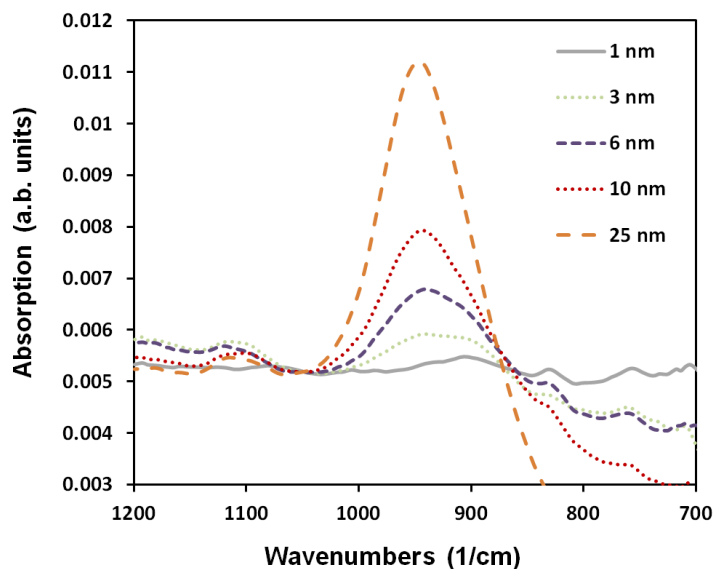


Figure 2-13 Effect of film thickness on FTIR spectrum for aluminum oxide ALD films. The peak is caused by Al-O stretching vibration.

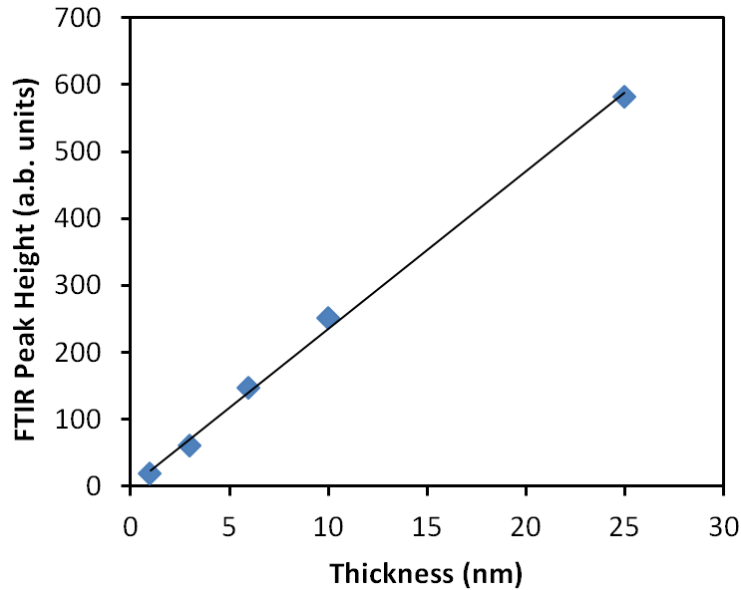


Figure 2-14 FTIR peak height for aluminum oxide films as a function of film thickness.

Hafnium and zirconium oxides have many similarities and their deposition by ALD is also similar. The molecular structure of the precursors used to deposit HfO_2 and ZrO_2 are shown in Figure 2-15.

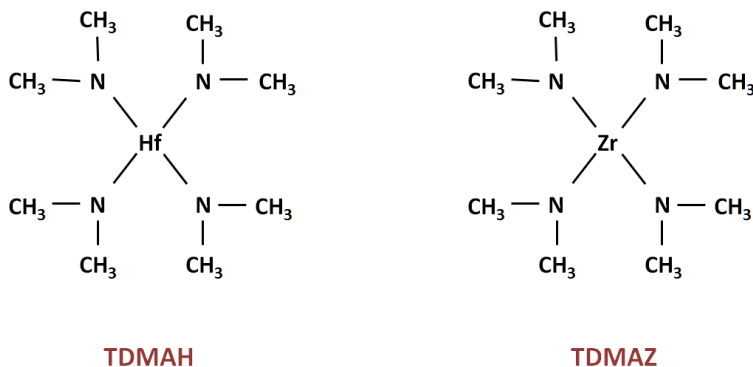


Figure 2-15 Molecular structure of tetrakis(dimethylamino) hafnium (TDMAH) and tetrakis(dimethylamide) zirconium (TDMAZ) used in ALD of HfO_2 and ZrO_2 , respectively.

These precursors need to be kept at elevated temperatures to have suitable vapor pressures. Based on GPC measurements, a temperature of 75°C was found

suitable for these precursors. Table 2-3 summarizes the deposition parameters used for ALD of HfO₂ and ZrO₂.

Table 2-3 Operating conditions for ALD of HfO₂ and ZrO₂ in thermal and plasma-enhanced ALD modes

| Parameter | Thermal ALD | Plasma-Enhanced ALD |
|---|-------------|---|
| TDMAH/TDMAZ pulse | 40 ms | 40 ms |
| The first purge time | 5 s | 5 s |
| H₂O or O₂ plasma pulse | 0.5 s | 0.5-2 s |
| The second purge time | 10 s | 2 s |
| Plasma power | - | 600 W |
| Precursor container temperature | 75 °C | 75 °C |
| ALD temperature window | 100-300°C | 25-300°C (250 °C for ZrO ₂) |
| Operating pressure | ~ 1 torr | ~ 1 torr |

The optical constants of ZrO₂ and HfO₂ ALD films deposited on Si substrates at 300°C in plasma-enhanced mode are shown in Figure 2-16. With a band gap of ~5.8 eV [32], these oxides show a small amount of absorption near the UV section of the spectrum. Since this absorption is relatively small, the Cauchy model can be used to describe the optical constants; however, it is more accurate to use a model that can accommodate an absorption edge near the UV part of the spectrum. Here, the Tauc–Lorentz model has been used to describe the optical constants of HfO₂ and ZrO₂. The Tauc-Lorentz model was designed for modeling of amorphous materials [33]. The absorption at energies higher than the band gap is defined by the following formula:

$$\varepsilon_2(E) \propto \frac{(E-E_g)^2}{E^2} \quad (2-3)$$

where ε_2 is the imaginary part of the dielectric function, E is photon energy, E_g is the band gap energy. The band gap energy of an amorphous material can be determined by plotting the parameter $\sqrt{\varepsilon_2} \cdot E$ as a function of photon energy and

extrapolating the linear part until it crosses the line $\sqrt{\epsilon_2} \cdot E = 0$ as shown in Figure 2-17.

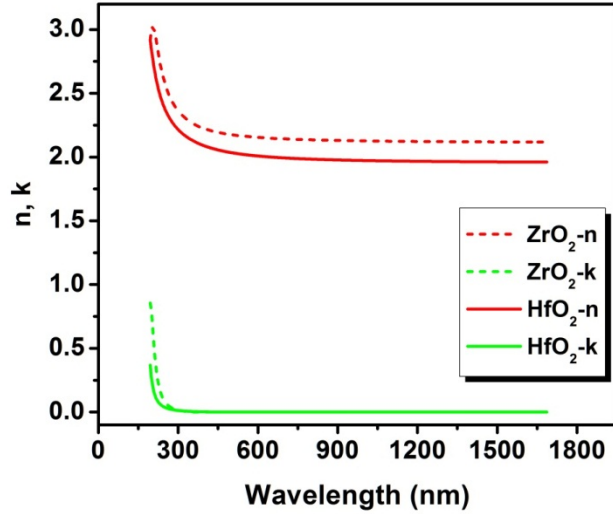


Figure 2-16 Optical constants of ZrO_2 and HfO_2 as a function of wavelength. Tauc-Lorentz parameterization was used to obtain the dispersions.

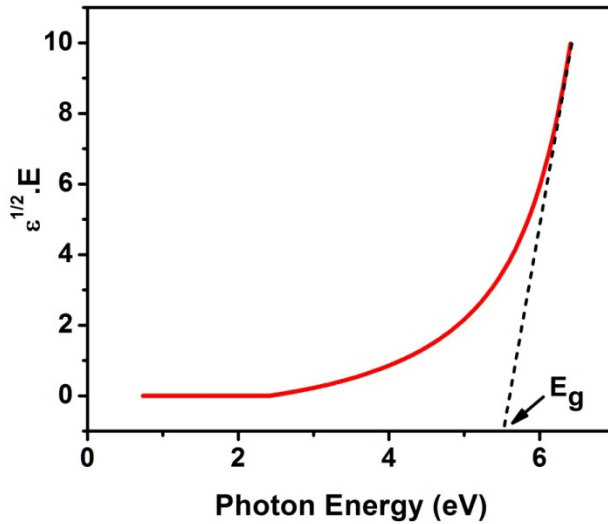


Figure 2-17 Tauc absorption method can be used to determine optical band gap energy, E_g . Here the band gap energy for HfO_2 ALD film deposited on Si at $200^\circ C$ is determined to be $\sim 5.5 eV$ by extrapolating the linear part of the curve to cross the photon energy axis.

For HfO₂, an optical band gap energy range of 5.4-5.6 eV was obtained from Tauc absorption analysis which is slightly lower than 5.7-5.8 eV, reported value for HfO₂ [34]. The difference could be due to levels of impurity in the films. The films deposited at lower substrate temperatures had the smallest band gaps. A larger band gap value of 5.6 eV was measured for films deposited at 300°C. ZrO₂ films had smaller band gap energies in the range of 5.0-5.2 eV as identified by the rise of the extinction coefficient, *k*, at a slightly longer wavelength compared to HfO₂ in Figure 2-16.

Figure 2-18 illustrates the growth per cycle for ALD of Al₂O₃, HfO₂ and ZrO₂ in plasma-enhanced mode as a function of deposition temperature. For aluminum oxide, GPC drops as the substrate temperature is increased, as discussed before. However, for hafnium oxide and zirconium oxide, the trend is not simple. At 50°C the GPC is close to 2.5 Å/cycle, a relatively high growth rate. It drops to less than 2 Å/cycle by increasing the temperature to 100°C and then it monotonically increases along with the deposition temperature. One possible explanation for such a change in trend is related to the type of precursors used for ALD of HfO₂ and ZrO₂. As mentioned earlier, TDMAH and TDMAZ precursors have relatively low pressures at room temperature and must be heated to provide enough vapor pressure required for the deposition. It is possible that these precursors condense on the surface of the substrate once they enter the deposition chamber. This condensation results in a non-ideal ALD growth and consequently a high measured GPC.

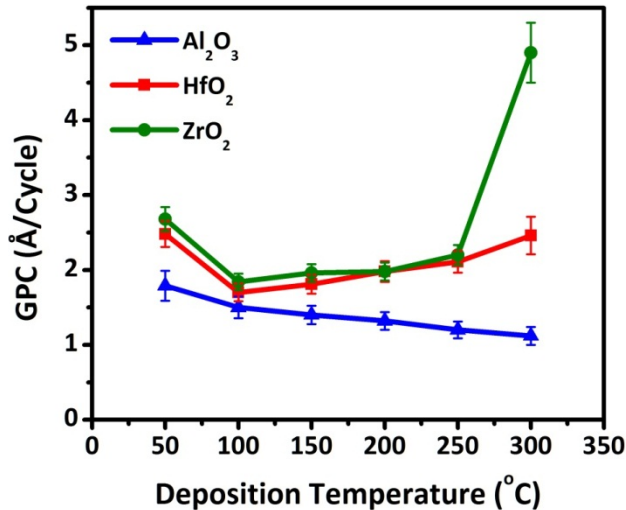


Figure 2-18 Growth per cycle during plasma-enhanced ALD of Al₂O₃, HfO₂ and ZrO₂ as a function of deposition temperature. The data is obtained from *in-situ* spectroscopic ellipsometry during the ALD growth.

HfO₂ and ZrO₂ have similar GPCs up to 250°C. At 300°C, HfO₂ seems to have a normal GPC, while for ZrO₂ a rather unusually high GPC is measured. The ALD of ZrO₂ at 300°C seems to involve some degree of non-ideality. The most probable cause to this deviation from ideal ALD growth is decomposition of the TDMAZ precursor at 300°C. Therefore the ALD reactions have a different nature at this temperature that can lead to high growth rates.

The variation of measured refractive index, *n*, as a function of deposition temperature for Al₂O₃, HfO₂ and ZrO₂ deposited in plasma-enhanced mode is shown in Figure 2-19. As a general trend, it can be seen that the refractive index improves by increasing the deposition temperature. For Al₂O₃ this variation is relatively small. However, for ZrO₂ and HfO₂, a larger variation is observed. At 50°C, ZrO₂ and HfO₂ films have the lowest refractive index indicating the films are not dense and possibly contain impurity that agrees with the observation made for the high GPC at this temperature and the precursor condensation phenomenon. Another important feature in Figure 2-19 is the decrease in refractive index of ZrO₂ by increasing the temperature from 200°C to 300°C that is consistent with the very high GPC.

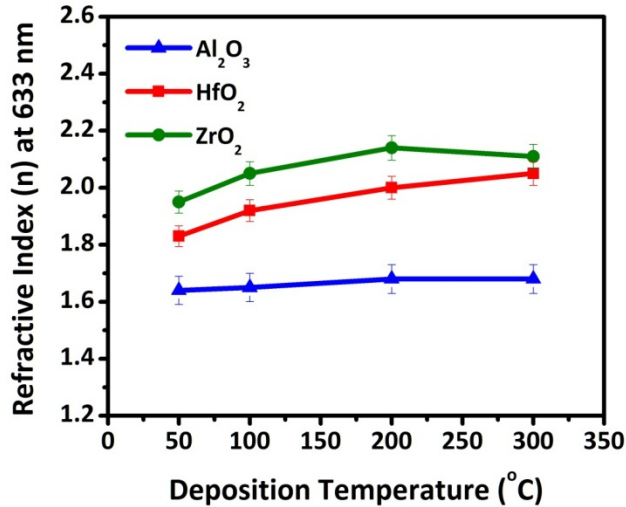


Figure 2-19 Measured refractive index for ALD oxides at different deposition temperatures.

Figure 2-20 shows the results of thickness measurement performed by *in-situ* spectroscopic ellipsometry and high-resolution cross-section TEM imaging. The main purpose of the experiment was to deposit 10 nm of ZrO₂ on a GaN substrate. The ALD procedure involved 58 PEALD cycles at 100°C. The sample was then annealed at 400°C. The thickness obtained from *in-situ* ellipsometry was 9.7 nm. High-resolution TEM images showed that the ZrO₂ film had an average physical thickness of ~9.0 nm. The two values are close. The difference can be related to the effect of annealing on the thickness. This comparison demonstrates the accuracy of ellipsometry measurements even for transparent substrates such as GaN. GaN is a semiconductor with a large band gap of 3.4 eV, which makes it transparent in most of the operating spectrum of ellipsometers. This results in a large number of interference fringes in the ellipsometry raw data. However, by having the benefits of *in-situ* measurements during growth, as explained before, an accurate thickness measurement can be performed.

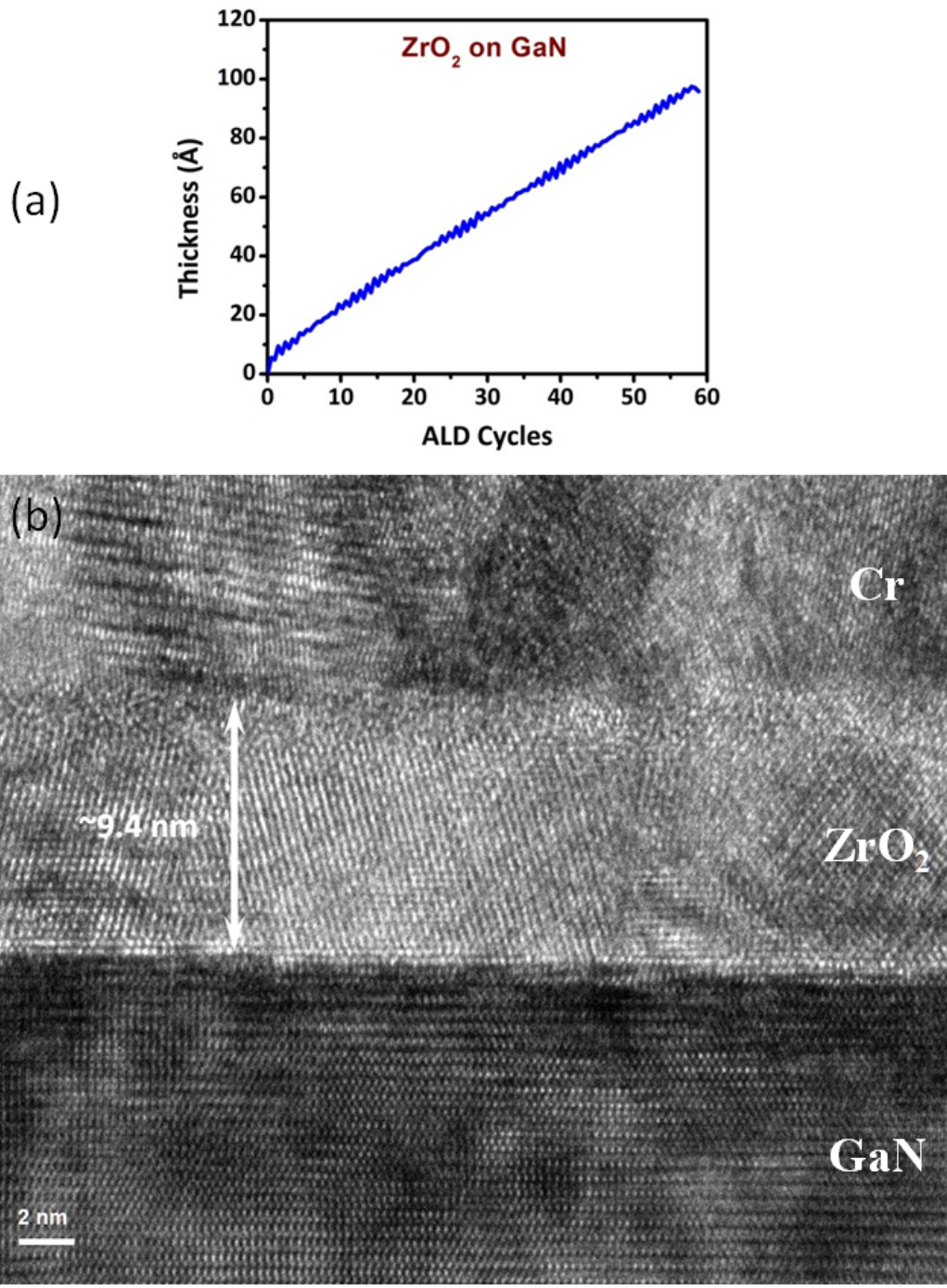


Figure 2-20 Comparison between measured ZrO₂ thickness grown by PEALD on GaN substrate using in-situ spectroscopic ellipsometry (a) and TEM imaging (b).

2.3.2 Chemical Composition

The chemical analysis of Al₂O₃ 10-nm films deposited on silicon substrates at the temperature of 100°C and 300°C are presented in Table 2-4. The films had an oxygen to aluminum ratio of 1.56 – 1.66, slightly higher than the stoichiometry ratio for aluminum oxide. The ratio improved by increasing the deposition temperature from 100°C to 300°C. Deposition temperature also seemed to affect the carbon content of the films, which ranged from 1.5 to 2.8 at. %. The presence of carbon in the films is due to organometallic nature of the TMA precursor. The level of carbon content in these films agrees with previously reported values [25]. Additionally, PEALD films seemed to contain less carbon compared to the films prepared by thermal ALD.

The films were also expected to contain some levels of hydrogen based on reported studies [13], although the XPS results could not be used to confirm this due to insensitivity to light elements. The fact that the films were rich in oxygen may suggest that the trapped hydrogen was mainly in the form of hydroxyl (-OH) groups. Experiments have shown that as the deposition temperature increases, the surface density of hydroxyl groups decreases [23]. This is linked to the lower excess oxygen in the films deposited at 300°C.

Table 2-4 Chemical composition of Al₂O₃ ALD films.

| Oxide | ALD Type | Deposition Temperature (°C) | Al at. % | O at. % | C at. % | O/Al ratio |
|--------------------------------|-------------|-----------------------------|----------|---------|---------|------------|
| Al ₂ O ₃ | Thermal-ALD | 100 | 36.7 | 60.5 | 2.8 | 1.65 |
| Al ₂ O ₃ | PEALD | 100 | 36.8 | 61.2 | 2.0 | 1.66 |
| Al ₂ O ₃ | Thermal-ALD | 300 | 38.3 | 59.6 | 2.1 | 1.56 |
| Al ₂ O ₃ | PEALD | 300 | 38.5 | 60.0 | 1.5 | 1.56 |

Figure 2-21 shows the XPS spectrum for an Al₂O₃ film. In addition to the elements listed in Table 2-4, Ar peaks are also seen in the survey spectrum.

However, as-deposited films did not show these Ar peaks which suggests that the Ar was added later during surface cleaning (using an Ar ion source). High resolution XPS spectra of Al 2p and C 1s peaks are plotted in Figure 2-22. The general shape of the Al 2p peak remains unchanged regardless of the deposition condition. However, a small shift toward lower binding energies is observed for the films deposited at 100°C. The shift seems to be related to the difference in oxygen to metal ratio.

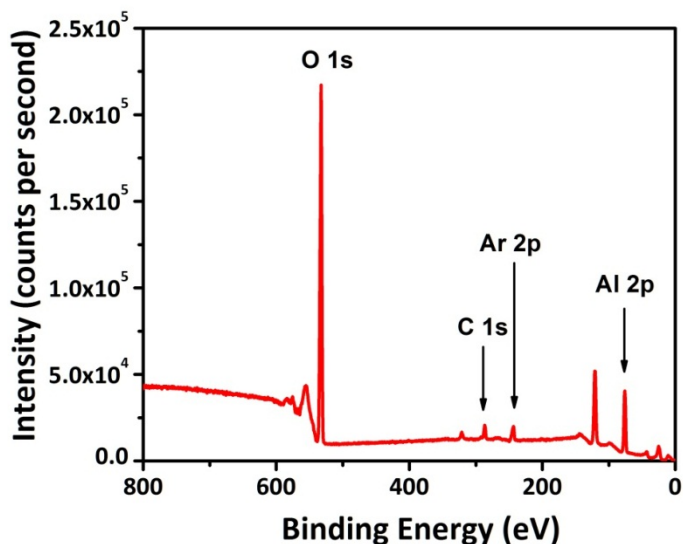


Figure 2-21 XPS survey spectrum for Al₂O₃ ALD film on Si. The main identified elements are O, C, Ar, and Al. The argon peak is only detected after surface cleaning using an Ar ion source due to ion implantation. The spectrum was calibrated by fixing the plot to the C1s peak at 284.8 eV.

The characteristic C 1s peak is observed at 284.8 eV. An additional peak is detected between 288 and 292 eV for films deposited at 100°C. This peak may be due to carbon compounds that contain the O-C=O bond at 289.03 eV. In addition to hydrogen, some of the excess oxygen in the films may be bound to carbon. The O-C=O peak is not observed in the films grown at 300°C since these films had lower carbon levels and less excess oxygen (O/Al ~ 1.5).

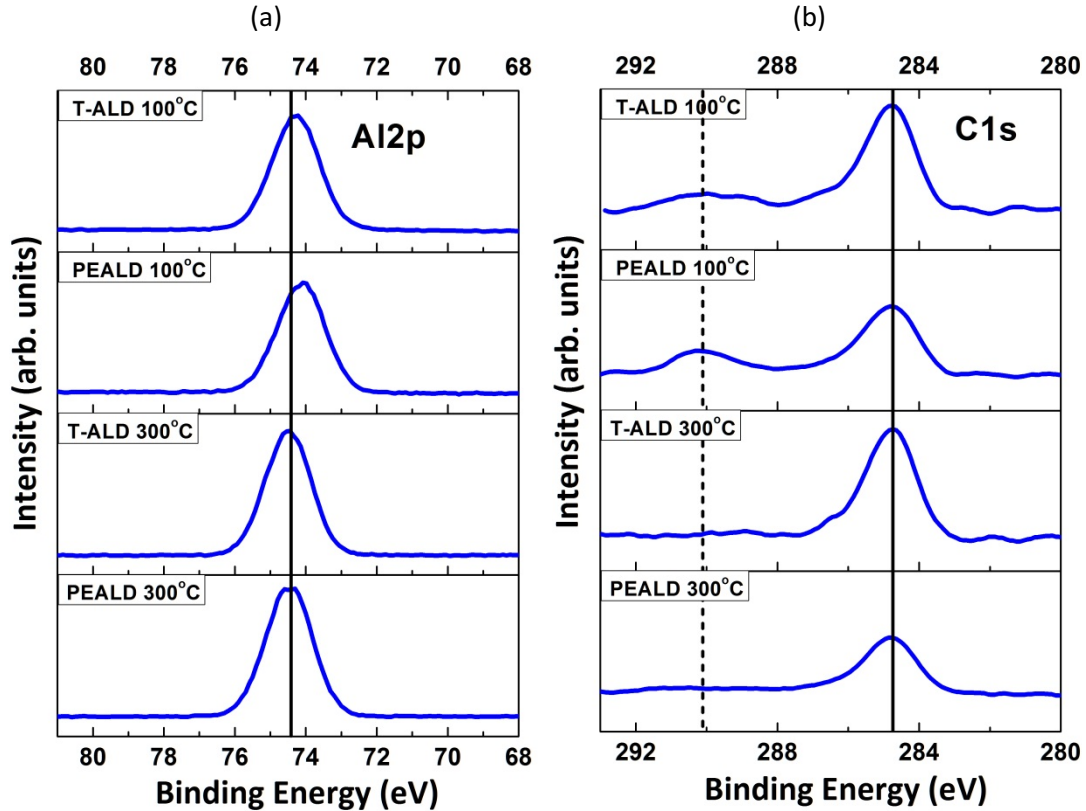


Figure 2-22 High resolution XPS spectra of Al₂p and C1s core levels in Al₂O₃ films prepared at different conditions. The plots were calibrated based on the C1s reference peak.

Chemical composition analysis of the 10 nm HfO₂ and ZrO₂ films is presented in Table 2-5 and Table 2-6, respectively. Similar to Al₂O₃ films, these films also contained carbon as an impurity. The amount of carbon in the films was higher compared to aluminum oxide and this is linked to the much larger size of TDMAH and TDMAZ precursor molecules, containing more carbon per metal atom. This increased the chance of carbon incorporation into the HfO₂ and ZrO₂ films. As a general trend, it is observed that the carbon level decreases as the deposition temperatures increases from 100°C to 300°C. However, for ZrO₂, the lowest carbon levels were observed in the films deposited at 200°C (data not shown here). This observation agrees with optical measurements, which showed that ZrO₂ films grown at 300°C possibly suffered from non-ideal ALD growth due to precursor decomposition, resulting in lower film density. Oxygen/metal ratio

ranged from ~2.1 to ~2.3, which showed the films were slightly rich in oxygen. The ratio also decreased as the substrate temperature increased from 100°C to 300°C. The highest amount of excess oxygen was observed for PEALD films grown at 100°C. Additionally, those films had the highest carbon content. This indicates that thermal ALD delivers better quality films compared to PEALD at the deposition temperature of 100°C using TDAMH and TDMAZ precursors.

Table 2-5 Chemical composition of HfO₂ ALD films.

| Oxide | ALD Type | Deposition Temperature (°C) | Hf at. % | O at. % | C at. % | O/Hf ratio |
|------------------|-------------|-----------------------------|----------|---------|---------|------------|
| HfO ₂ | Thermal-ALD | 100 | 30.5 | 64.7 | 4.8 | 2.12 |
| HfO ₂ | PEALD | 100 | 28.6 | 66.4 | 4.9 | 2.32 |
| HfO ₂ | Thermal-ALD | 300 | 31.2 | 65.3 | 3.5 | 2.09 |
| HfO ₂ | PEALD | 300 | 31.5 | 65.5 | 3.0 | 2.07 |

Table 2-6 Chemical composition of ZrO₂ ALD films

| Oxide | ALD Type | Deposition Temperature (°C) | Zr at. % | O at. % | C at. % | O/Zr ratio |
|------------------|-------------|-----------------------------|----------|---------|---------|------------|
| ZrO ₂ | Thermal-ALD | 100 | 31.0 | 64.1 | 4.9 | 2.07 |
| ZrO ₂ | PEALD | 100 | 28.4 | 66.1 | 5.5 | 2.33 |
| ZrO ₂ | Thermal-ALD | 300 | 30.5 | 65.3 | 4.2 | 2.14 |
| ZrO ₂ | PEALD | 300 | 30.4 | 65.1 | 4.5 | 2.14 |

Figure 2-23 shows the XPS survey spectra for HfO₂ and ZrO₂ ALD films. Hafnium and zirconium elements have several XPS characteristic peaks. Among the peaks, Hf4d and Zr3d were chosen for quantitative analysis. High-resolution XPS spectra for these peaks are shown in Figure 2-24. Similar to Al₂O₃ XPS spectra, a shift towards lower binding energies can be seen in the PEALD films grown at 100°C, which matches with the higher oxygen/metal ratio in these films. It is expected that changing ALD process parameters such as plasma exposure length and power could decrease the impurity levels and improve the oxygen/metal ratio.

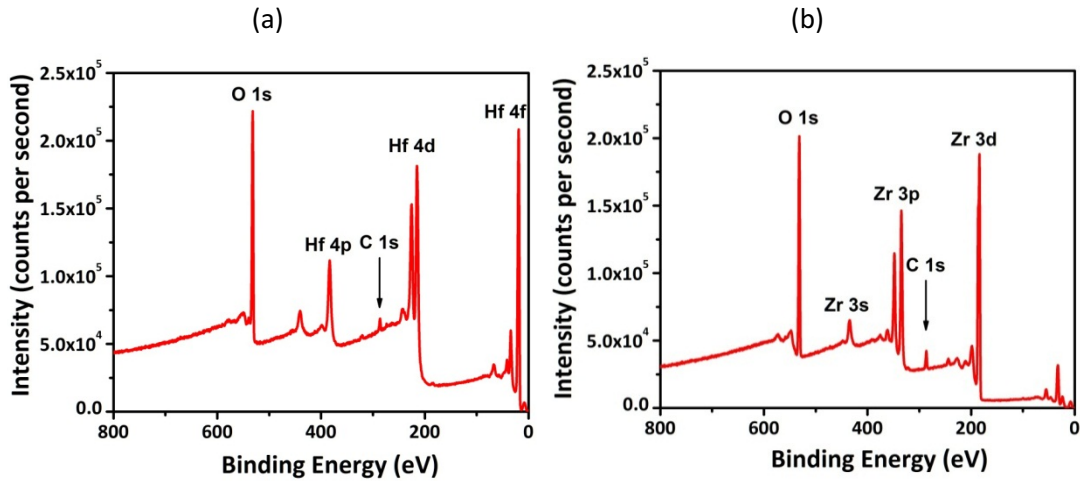


Figure 2-23 XPS survey spectra for HfO₂ (a), and ZrO₂ (b) ALD films grown on Si.

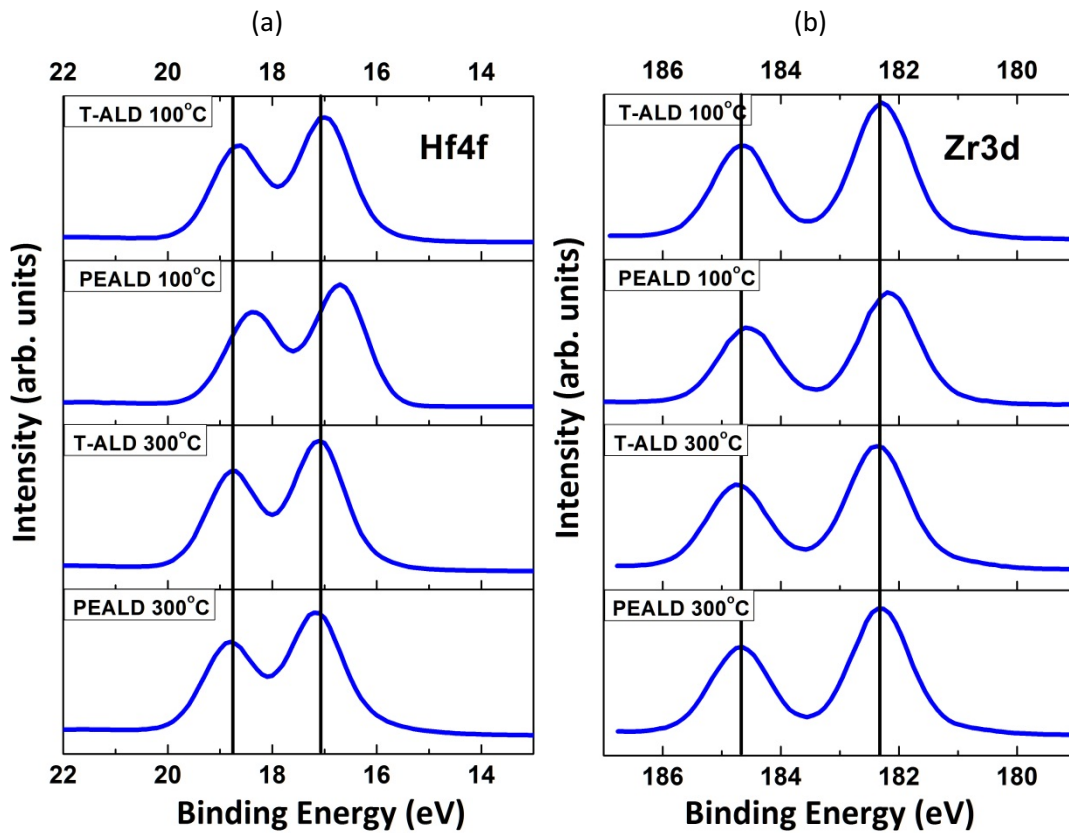


Figure 2-24 High-resolution XPS spectra for HfO₂ (a), and ZrO₂ ALD films. The films grown at 100°C by PEALD have shifted to lower binding energies due to a change in oxygen/metal ratio.

2.4 Conclusions

Thin Al_2O_3 , HfO_2 , and ZrO_2 films were grown by atomic layer deposition on silicon substrates in different operating conditions. Thickness and optical properties were measured using *in-situ* spectroscopic ellipsometry. Raw ellipsometry data was used to determine the growth rate, refractive index and optical band gap energy of the grown films. The results showed that both thermal ALD and PEALD can be used to deposit thin metal oxide films within the ALD temperature window. It was shown that the deposition temperature is one of the key process parameters in ALD of these metal oxides. As a general trend, the optical properties were improved by increasing the deposition temperature. Compositional analysis performed by XPS measurements showed that all the ALD films contained carbon as impurity. The oxygen to metal ratio was also determined to be higher than the stoichiometry ratio. Both the impurity levels and oxygen to metal ratio were improved by increasing the deposition temperature.

2.5 References

- [1] M. Leskela, M. Ritala, *Thin Solid Films* 409/1 (2002) 138.
- [2] C.W. Jeong, B.I. Lee, S.K. Joo, *Mat Sci Eng C-Bio S* 16/1-2 (2001) 59.
- [3] F. Lee, S. Marcus, E. Shero, G. Wilk, J. Swerts, J.W. Maes, T. Blomberg, 2007 IEEE/Semi Advanced Semiconductor Manufacturing Conference (2007) 291.
- [4] S. Natarajan, M. Armstrong, M. Bost, R. Brain, M. Brazier, C.H. Chang, V. Chikarmane, M. Childs, H. Deshpande, K. Dev, G. Ding, T. Ghani, O. Golonzka, W. Han, J. He, R. Heussner, R. James, I. Jin, C. Kenyon, S. Klopčič, S.H. Lee, M. Liu, S. Lodha, B. McFadden, A. Murthy, L. Neiberg, J. Neiryneck, P. Packan, S. Pae, C. Parker, C. Pelto, L. Pipes, J. Sebastian, J. Seiple, B. Sell, S. Sivakumar, B. Song, K. Tone, T. Troeger, C. Weber, M. Yang, A. Yeoh, K. Zhang, *Int El Devices Meet* (2008) 941.
- [5] R. Luptak, J.M.J. Lopes, S. Lenk, B. Hollander, E.D. Ozben, A.T. Tiedemann, M. Schnee, J. Schubert, S. Habicht, S. Feste, S. Mantl, U. Breuer, A. Besmehn, P.K. Baumann, M. Heuken, *AVS*, 2011, p. 01A301.
- [6] S. Gieraltowska, D. Sztenkiel, E. Guziewicz, M. Godlewski, G. Luka, B.S. Witkowski, L. Wachnicki, E. Lusakowska, T. Dietl, M. Sawicki, *Acta Phys Pol A* 119/5 (2011) 692.
- [7] S. Jakschik, U. Schroeder, T. Hecht, G. Dollinger, A. Bergmaier, J.W. Bartha, *Mat Sci Eng B-Solid* 107/3 (2004) 251.
- [8] H.J. Cho, Y.D. Kim, D.S. Park, E. Lee, C.H. Park, J.S. Jang, K.B. Lee, H.W. Kim, Y.J. Ki, I.K. Han, Y.W. Song, *Solid State Electron* 51/11–12 (2007) 1529.
- [9] H. Seidl, M. Gutsche, U. Schroeder, A. Birner, T. Hecht, S. Jakschik, J. Luetzen, M. Kerber, S. Kudelka, T. Popp, A. Orth, H. Reisinger, A. Saenger, K. Schupke, B. Sell, *International Electron Devices 2002 Meeting, Technical Digest* (2002) 839.
- [10] T.M. Mayer, J.W. Elam, S.M. George, P.G. Kotula, R.S. Goeke, *Appl Phys Lett* 82/17 (2003) 2883.
- [11] E.P. Gusev, M. Copel, E. Cartier, I.J.R. Baumvol, C. Krug, M.A. Gribelyuk, *Appl Phys Lett* 76/2 (2000) 176.

- [12] R. Katamreddy, R. Inman, G. Jursich, A. Soulet, C. Takoudis, *Journal of The Electrochemical Society* 153/10 (2006) C701.
- [13] A. Niskanen, K. Arstila, M. Ritala, M. Leskelä, *Journal of The Electrochemical Society* 152/7 (2005) F90.
- [14] J.C. Hackley, J.D. Demaree, T. Gougousi, *Journal of Vacuum Science & Technology A* 26/5 (2008) 1235.
- [15] V. Sammelseg, R. Rammula, J. Aarik, A. Kikas, K. Kooser, T. Kaambre, *Journal of Electron Spectroscopy and Related Phenomena* 156-158 (2007) 150.
- [16] M.D. Groner, J.W. Elam, F.H. Fabreguette, S.M. George, *Thin Solid Films* 413/1-2 (2002) 186.
- [17] K. Kukli, M. Ritala, T. Sajavaara, J. Keinonen, M. Leskela, *Chemical Vapor Deposition* 8/5 (2002) 199.
- [18] E. Langereis, S.B.S. Heil, H.C.M. Knoops, W. Keuning, M.C.M. van de Sanden, W.M.M. Kessels, *J Phys D Appl Phys* 42/7 (2009).
- [19] R.A. Wind, S.M. George, *J Phys Chem A* 114/3 (2010) 1281.
- [20] R.A. Matero, A. Rahtu, M. Ritala, *Langmuir* 21/8 (2005) 3498.
- [21] K. Ostrikov, E. Tsakadze, N. Jiang, Z. Tsakadze, J. Long, R. Storer, X. Shuyan, *Plasma Science, IEEE Transactions on* 30/1 (2002) 128.
- [22] H. Fujiwara, *Spectroscopic Ellipsometry: Principles and Applications*, Wiley, 2007.
- [23] H.B. Profijt, S.E. Potts, M.C.M. van de Sanden, W.M.M. Kessels, *Journal of Vacuum Science & Technology A* 29/5 (2011).
- [24] M. Deminsky, *Surface Science* 549/1 (2004) 67.
- [25] J.L. van Hemmen, S.B.S. Heil, J.H. Klootwijk, F. Roozeboom, C.J. Hodson, M.C.M. van de Sanden, W.M.M. Kessels, *Journal of The Electrochemical Society* 154/7 (2007) G165.
- [26] R. Matero, A. Rahtu, M. Ritala, M. Leskelä, T. Sajavaara, *Thin Solid Films* 368/1 (2000) 1.
- [27] A. Paranjpe, S. Gopinath, T. Omstead, R. Bubber, *Journal of The Electrochemical Society* 148/9 (2001) G465.

- [28] J.W. Elam, C.E. Nelson, R.K. Grubbs, S.M. George, *Thin Solid Films* 386/1 (2001) 41.
- [29] A. Deshpande, R. Inman, G. Jursich, C. Takoudis, *Journal of Vacuum Science & Technology A* 22/5 (2004) 2035.
- [30] S.X. Lao, R.M. Martin, J.P. Chang, *Journal of Vacuum Science & Technology A* 23/3 (2005) 488.
- [31] R. Katamreddy, R. Inman, G. Jursich, A. Soulet, A. Nicholls, C. Takoudis, *Thin Solid Films* 515/17 (2007) 6931.
- [32] J. Robertson, *Eur Phys J-Appl Phys* 28/3 (2004) 265.
- [33] J. Tauc, R. Grigorovici, A. Vancu, *physica status solidi (b)* 15/2 (1966) 627.
- [34] H. Takeuchi, D. Ha, T.-J. King, *Journal of Vacuum Science & Technology A: Vacuum, Surfaces, and Films* 22/4 (2004) 1337.

Chapter 3 Preparation of Sputtered Chromium Thin Films^{*}

3.1 Introduction

Chromium (Cr) thin films are used in the fabrication of masks for integrated circuit photolithography, diaphragms and mirrors for microelectromechanical systems (MEMS), as an adhesion layer for gold films, and as thin film resistor material [1]. Cr has also been widely studied as an archetypal band antiferromagnet [2, 3]. Furthermore, Cr is a spin density wave (SDW) material and recent research has focused on SDW properties of Cr thin films [4] as well as resonant impurity scattering in these materials [5]. Cr thin films also have been shown to have very high resistivity [5-8] that depends on sputtering pressure.

The relationship between the microstructure of thick films (25 to 250 μm thick) and the sputtering pressure and temperature was developed by Thornton [8-10]. This structural zone model has been further refined to include thin films down to 100 nm, nanostructure as well as microstructure, and the reduction of the temperature and pressure variables to one energy variable [11]. The role of

^{*} A version of this chapter has been published in:
Foroughi-Abari, A., Xu, C., Cadien, K.C., *Thin Solid Films*, 520 (2012)

oxygen in the deposition system has been shown to retard structure growth for evaporated Al thin films [12]. In Thornton's Zone Model there are several zones of microstructure that develop in films depending on the sputtering pressure and the homologous temperature, T_H . At low T_H and higher sputtering pressures the film microstructure consists of tapered crystallites with voided intergranular boundaries (zone 1). This leads to a porous structure which has poor lateral strength and low density [9]. At higher T_H the structure consists of a transition structure that is made up of densely packed but poorly defined fibrous grains that are separated by nearly conventional grain boundaries (zone T) [9]. Metal coatings with the transition structure exhibit high optical reflectance, moderate and relatively low resistivity, and a state of compression [13-15]. At even higher T_H and all pressures, the structure consists of columnar grains separated by dense intercrystalline boundaries (zone 2). At the highest T_H and all sputtering pressures the structure, consists of recrystallized equiaxed grains (zone 3) [16].

In this research, Cr thin films were deposited on oxidized Si wafers using two sputtering systems with different levels of cleanliness, and at argon sputtering pressures varying between 0.13 and 0.93 Pa. Electrical transport measurements were conducted on these films to investigate the influence of argon pressure on film electrical resistivity. The film morphology, microstructure and composition were characterized using scanning electron microscopy (SEM) and X-ray photoelectron spectroscopy (XPS). The resistivity performance and the microstructure of sputtered Cr thin films under different sputtering pressure were found to have significant differences. This change was shown to be due to the transition from a porous structure to a denser microstructure. Furthermore, it is shown that the resistivity change can be used to locate the boundary between these microstructures.

The Cr films sputtered at high pressure contained large quantities of oxygen after exposure to air. This oxygen was shown to be due to the formation of a native oxide on the surface of the porous Cr grains. Optical measurements were also

performed to investigate the effects of deposition pressure on the optical properties.

3.2 Experimental Procedure

Thin films of Cr were prepared by DC magnetron sputtering. Two sputtering systems were used in the experiments: sputtering system #1 and #2. Most of the films were grown in sputtering system #1, a load locked system with a base pressure below 4.0×10^{-5} Pa. For runs done in both systems the gun power was 300W DC, there was no substrate heat, and the Ar gas pressure was varied between 0.13 Pa and 0.93 Pa. Both systems used 75 mm diameter x 6.4 mm thick Cr metal targets with 99.95% purity, a common Ar high purity (99.998%) gas supply, and both units had cryopump high vacuum systems. Under these conditions, the deposition rate of Cr was 0.27 nm/s for 0.13 Pa argon pressure and 0.38 nm/s for 0.93 Pa argon pressure. To investigate the effect of base pressure on film resistivity, a series of Cr thin films were deposited in sputtering system #2. This system had a base pressure $< 3.2 \times 10^{-4}$ Pa, and since the chamber was exposed to air each time a sample was loaded, it was expected that the level of absorbed gases, such as water vapor, would much higher than in system #1.

Oxidized Si (100) wafers and microscope slides were used as substrates in these experiments. The Si wafers were cleaned in a standard Piranha solution (3:1 mixture of sulfuric acid and hydrogen peroxide) followed by a thermal oxidization process that formed a 200 nm SiO₂ layer on the wafers. Microscope slides were cleaned in isopropanol and dried in nitrogen. 150 nm Cr films were deposited for resistivity measurement. Film resistivity was obtained from sheet resistance data measured by a four point probe and the film thickness measured by stylus profilometry. The surface morphologies of the Cr films were imaged using a SEM (JEOL JAMP-9500F Field Emission Auger Microscope). To determine the surface composition of the films, XPS analysis was performed with a Kratos Analytical

AXIS-165 spectrometer at the ACSES facility. The base pressure in the analytical chamber was lower than 3×10^{-8} Pa. A monochromatic Al K_{α} ($h\nu = 1486.6$ eV) source was used at a power of 210 W. Survey spectra were collected for binding energies ranging from 1100 to 0 eV with a pass energy (PE) of 160 eV and step size of 0.35 eV. High-resolution spectra were measured with a PE of 20 eV and step size of 0.1 eV. A 4 keV argon ion beam was used for depth profiling. The beam was scanned with an amplitude of ± 1.5 mm in the x and y directions.

Optical properties of the films deposited on Si (100) substrates were measured using a Variable Angle Spectroscopic Ellipsometer (VASE) from J. A. Woollam Inc. The spectroscopic data was acquired at an angle of incidence of 75° over the spectral range of 1.5 to 4.1 eV. WVASE32 software was used for generation of model data and fitting to the experimental data. Spectroscopic measurements were performed on 10-nm-thick Cr films deposited on silicon substrates.

3.3 Results and Discussion

A two dimensional representation of the zone model is shown in Figure 3-1 with different regions of microstructure that depend on sputtering temperature and pressure. This diagram is based on Thornton's "Zone Model" [8, 9] which was based on the microstructural observation of thick metal films. The diagram is divided into four zones. Due to equipment operating limitations, the sputtering experiments were performed at room temperature. Since the homologous temperature of Cr is 0.14 at 300 K, with the variation in argon pressure from 0.13 to 0.93 Pa, the thin films would have microstructures changing from zone T to zone I as the sputtering pressure is increased. Zone I has a porous structure, consisting of tapered crystallites separated by voids. If exposed to air, the thin film will quickly oxidize leading to degraded purity and high resistivity. Zone T, however, has a transition structure of densely packed fibrous grains. The thin films in zone T would be in compression and have low resistivity.

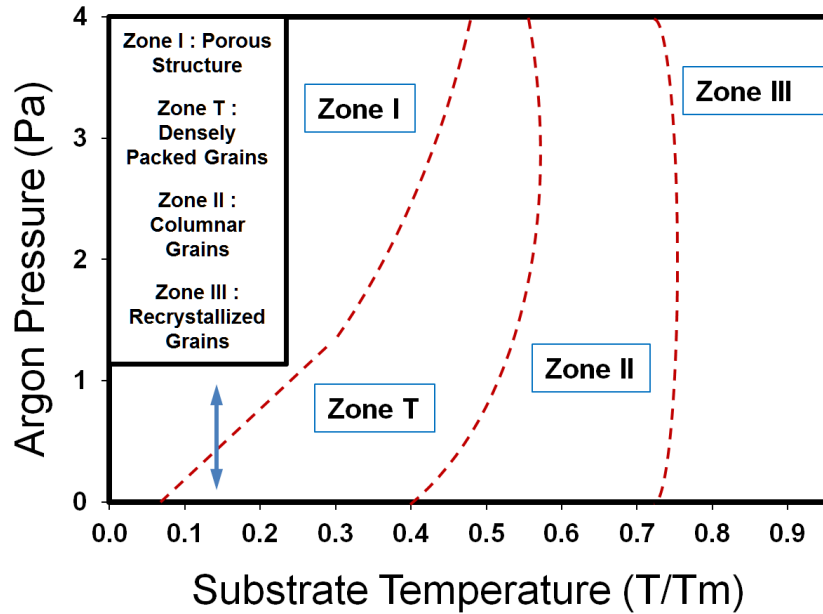


Figure 3-1 Schematic diagram showing the influence of argon pressure and substrate temperature on microstructure of sputtered metallic films, reproduced from [8]. The arrow indicates the operating range used in the experiments.

3.3.1 Electrical resistivity

The electrical resistivity of metal thin films is a sensitive indicator of the structure and purity of the films [17]. In order to understand the impact of the base pressure on the resistivity of Cr, thin films were grown in two different sputtering systems with different base pressures, as shown in Table 3-1.

Table 3-1 The effect of sputter system base pressure on the Cr film resistivity at 0.23 and 0.80 Pa Ar sputtering pressure.

| Sputter System | Resistivity, $\mu\Omega\cdot\text{cm}$ | |
|----------------|--|----------------------------------|
| | $P_{\text{Ar}}= 0.23 \text{ Pa}$ | $P_{\text{Ar}}= 0.80 \text{ Pa}$ |
| #1 | 33.3 | 168.4 |
| #2 | 78.1 | 236.0 |

The films grown in sputtering system #2 have resistivity values more than two times greater than the values obtained in system #1 at 0.23 Pa argon pressure and 35 % higher at 0.8 Pa. However, the increase in resistivity at both pressures is ~40-60 $\mu\Omega\cdot\text{cm}$. The only difference between the two sputtering systems is the quality of the base pressure. Base pressure governs the amount of residual oxygen in the sputtering system. The amount of oxygen incorporated into the growing Cr films can be estimated from the growth rate of the Cr films, and the impingement rate, N_i , of the residual oxygen in the chamber based on the following equation:

$$N_i = P(2\pi mk_B T)^{-\frac{1}{2}} \quad (3-1)$$

where N_i has units of molecules $\text{cm}^{-2}\text{s}^{-1}$, P is the partial pressure of oxygen in the vacuum chamber, m is the mass of the oxygen molecule, k_B is Boltzmann's constant, and T is temperature in Kelvin [18]. From the equation for N_i , the residual oxygen flux impinging on the growing film is directly proportional to P . Assuming $T=300\text{K}$ and that the partial pressure of oxygen in the chamber is ~0.21 of the total pressure (same ratio as oxygen in air at standard temperature and pressure), $P_{O_2} = 8.20 \times 10^{-6}$ Pa for system #1 and $P_{O_2} = 6.72 \times 10^{-5}$ Pa for system #2. A Cr deposition rate of $0.38 \text{ nm}\cdot\text{s}^{-1}$ (0.93 Pa argon pressure) gives a Cr flux of 5.24×10^{14} atoms $\text{cm}^{-2}\text{s}^{-1}$, and the O flux for system #1 is 4.41×10^{13} atoms $\text{cm}^{-2}\text{s}^{-1}$ and for system #2 it is 3.61×10^{14} atoms $\text{cm}^{-2}\text{s}^{-1}$. This gives an approximate atomic oxygen concentration of 8% for system #1 and 40% for system #2. These values are only estimates since this is a simplified calculation. The oxygen sticking coefficient is assumed to be one and the influence of molecular pumping speed on the partial pressure of gases at base pressure is ignored. The value for system #2 appears to be high since other research done on sputtering system # 2 showed approximately 25 at% O in niobium thin films grown in system # 2 [19]. However, this calculation points out the dramatic influence of base pressure and deposition rate on film purity. It also explains why films from system #2 have much higher resistivity than films from system #1. The remainder of the results discussed will be those from system # 1 without

identification.

The effect of argon sputtering pressure on film resistivity is shown in Figure 3-2. All films had an average thickness of 150 ± 4 nm. The resistivity of the sputtered films increased from $25.7 \mu\Omega\cdot\text{cm}$ at 0.13 Pa to $364 \mu\Omega\cdot\text{cm}$ at 1.06 Pa Ar working pressure. The resistivity appears to level off below 0.23 Pa but increases for all pressures above 0.23 Pa. Also plotted in this figure is data taken from reference [5].

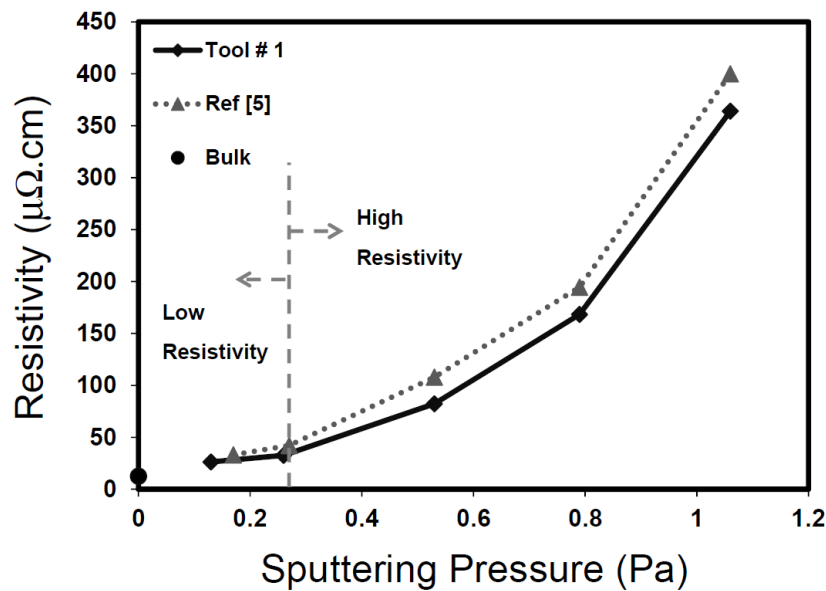


Figure 3-2 The resistivity of chromium sputtering system #1 and sputtering system #2 as a function of argon pressure

The observed resistivity trend can be explained by referring to the expanded view on the zone diagram shown in Figure 3-3. Since all experiments were done at room temperature, T_H is 0.14 as indicated by the vertical line on the figure. The films grown in zone T are denser and have higher conductivity than those grown under zone I conditions. Therefore, at low sputtering pressures (<0.3 Pa) the structure of the films would consist of densely packed grains. This is due to the fact that at low sputtering pressures the mean free path of target atoms is relatively

long (21 cm at 0.13 Pa argon pressure) with respect to the target/substrate separation (17 cm for the sputtering system #1). Therefore, the probability of a collision occurring before a target atom reaches the substrate is lower, and as a result, the arriving atoms have higher kinetic energies which results in higher surface mobility and a denser structure. However by increasing the pressure and entering zone I, the structure would become more porous and resistivity values start to increase which similarly can be explained by the effect of the mean free path on the film microstructure. The SEM images inside the graph are from the films deposited at 0.13 and 0.93 Pa and are discussed in more detail in the next section. They show that the structural variation as a result of the change in sputtering pressure is the reason for the resistivity increase.

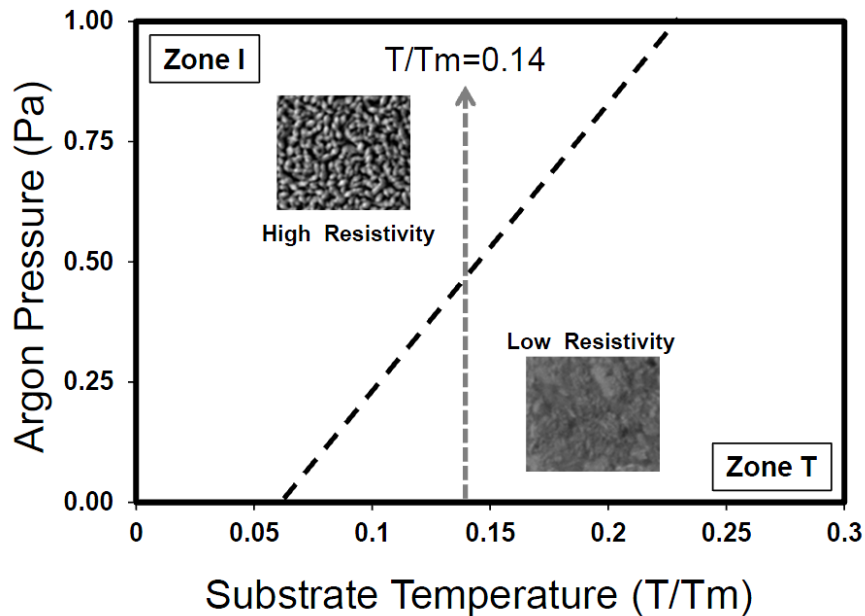


Figure 3-3 Magnified portion of the zone diagram showing the boundary of zone I and T. The vertical arrow indicates the path of experimental data covering an argon pressure range of 0.13 to 0.93 Pa.

3.3.2 Microstructure and surface morphology

The microstructure of the Cr films grown at different sputtering pressures was

studied using SEM. Several 100,000× magnification SEM images were taken to differentiate the surface microstructure of the Cr films. Figure 3-4 shows microstructure changes in chromium films grown at sputtering pressures ranging from 0.13 to 0.93 Pa. The figure reveals that the surface microstructures of Cr thin films sputtered at 0.13 and 0.93 Pa are significantly different.

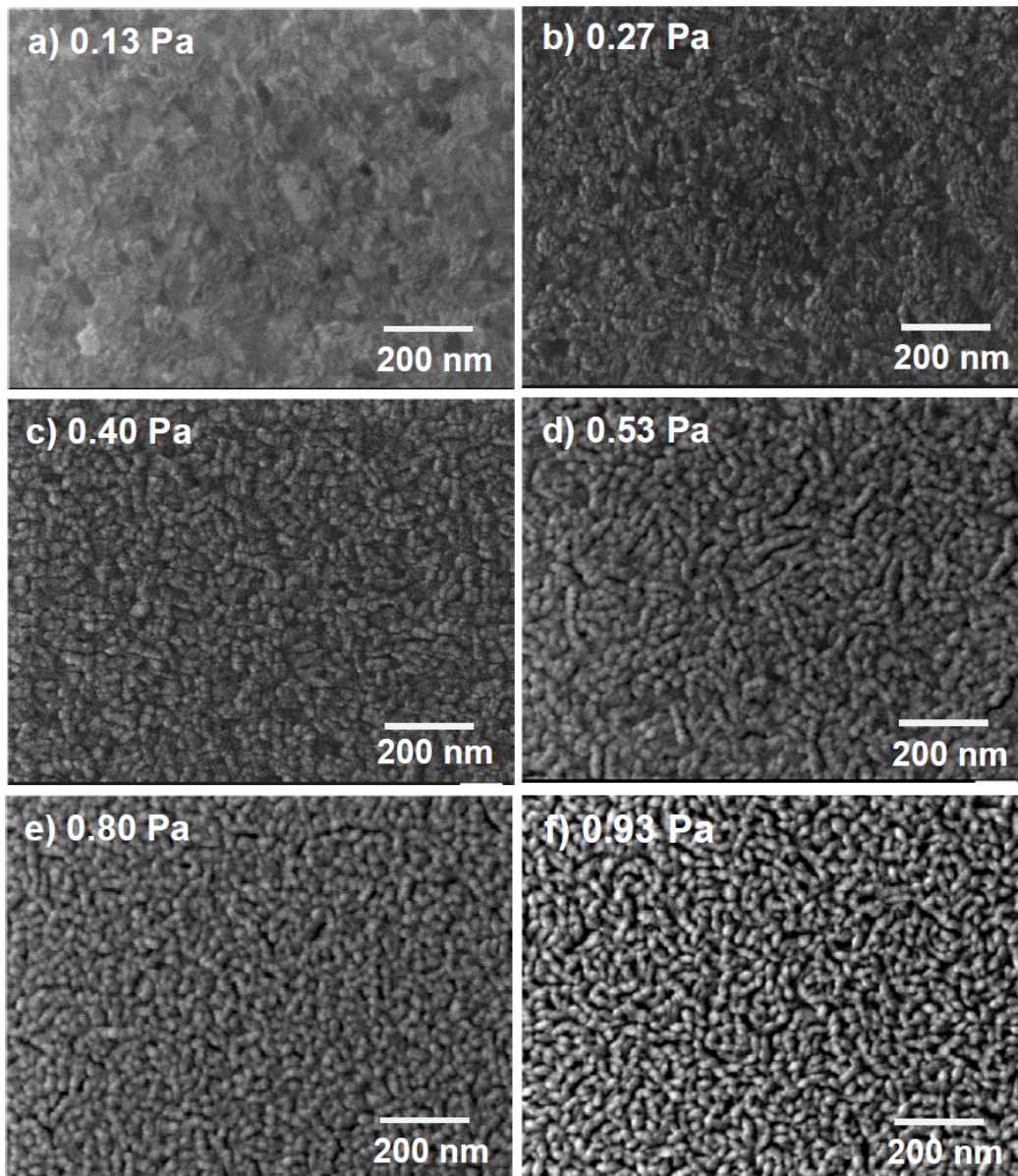


Figure 3-4 SEM images of surface of chromium thin films sputtered under different argon pressures: (a) 0.13 Pa (b) 0.27 Pa (c) 0.40 Pa (d) 0.53 Pa (e) 0.80 Pa (f) 0.93 Pa.

The Cr film sputtered at 0.13 Pa (Zone T) has a smooth and dense surface compared to the 0.93 Pa (Zone I) sputtered Cr film. The Cr film sputtered at 0.93 Pa appears to have a rougher surface and possible evidence of porosity. The film surface consisted of small crystallites separated by voids. From 0.13 to 0.93 Pa, the thin film surface appears to be rougher and have more voids. Similar to the argument discussed for resistivity data, this can be explained using Figure 3-1. At low sputtering pressures, sputtered films are smoother and denser as predicted by Thornton's zone model (zone T). Moving to higher pressures, the microstructure shifts to a porous and rough morphology which are characteristic of zone I. This porous microstructure leads to a much higher resistivity. Clearly pores in the Cr microstructure disrupt electron flow reducing electron mean free path.

The composition of the surface of the Cr films sputtered at 0.13 and 0.93 Pa were measured using XPS. Prior to measurements, *in-situ* physical sputter etching with a 5 nm/min etch rate was performed to remove the native oxide and other surface contamination. High resolution XPS spectra of the Cr_{2p_{3/2}} core level of the sputtered Cr thin film deposited at 0.13 and 0.93 Pa argon pressure are shown in Figure 3-5. The film deposited at 0.13 Pa shows a higher peak compared to the film deposited at 0.93 Pa which is due to the higher amount of chromium metal in the film structure.

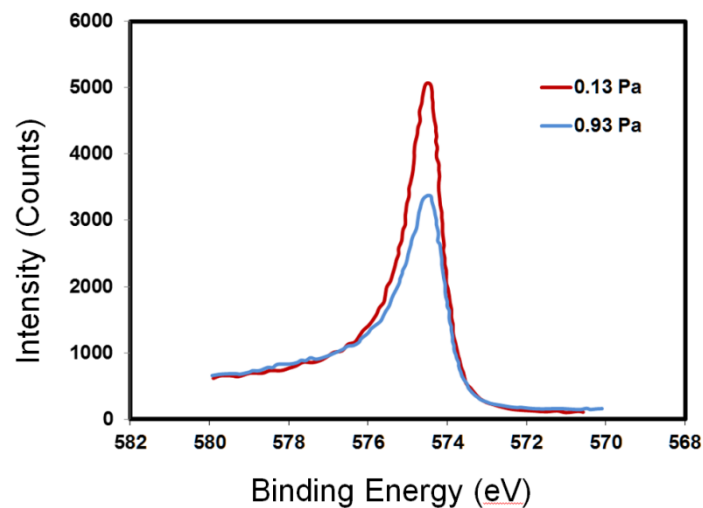


Figure 3-5 High resolution XPS spectra of Cr_{2p_{3/2}} core level of the sputtered chromium thin film deposited at 0.13 Pa argon pressure and 0.93 Pa argon pressure.

Table 3-2 shows the calculated compositions of the two samples (the calculations were done using CasaXPS software). After 1 min of *in-situ* sputter etching, the Cr films grown at 0.13 Pa contained 7.2% O, in good agreement with the value of 8% predicted earlier.

Table 3-2 XPS results showing surface composition of Cr films prepared at 0.13 and 0.93 Pa after 1 and 4 min of sputter-etching (SE)

| Deposition Pressure, SE time | at. % Cr | at. % O |
|-------------------------------------|-----------------|----------------|
| 0.13 Pa, 1 min. | 89.1 | 7.2 |
| 0.13 Pa, 4 min. | 89.8 | 5.5 |
| | | |
| 0.93 Pa, 1 min. | 66.0 | 23.7 |
| 0.93 Pa, 4 min. | 79.2 | 13.8 |

This oxygen comes from the residual oxygen in the chamber and should not change with sputtering pressure. However, the film sputtered at 0.93 Pa contains 23.7% O. It is apparent that this extra oxygen is due to porous nature of the films grown at higher pressure. That is, when these films are exposed to air, a native oxide forms on the internal surfaces of the pores, leading to a much higher oxygen level. If this is correct, we would expect the oxygen level to be highest near the surface of the film. To test this hypothesis, the films were sputter etched *in-situ* for 4 min (20 nm Cr removal). The Cr composition of the 0.13 Pa film showed little change. However, the amount of Cr in 0.93 Pa film increased by 13%. This trend is in agreement with our hypothesis that the oxygen diffused into the porous structure of the films once exposed to air and formed stable oxides, shown schematically in Figure 3-6a. It is concluded that the thin film properties were altered upon atmospheric exposure.

In order to explain the very high oxygen contents observed in XPS measurements, a simple model was developed based on the probability that the oxygen signal comes from a native oxide formed on the surface of the Cr. To simplify the model, the columnar grains were assumed to have a circular cross-section with a Cr metal

core and a thin oxide shell as shown schematically in Figure 3-6b. The oxide layer is formed once the metal surface is exposed to air (negative free energy of formation of chromium oxide at room temperature [20]).

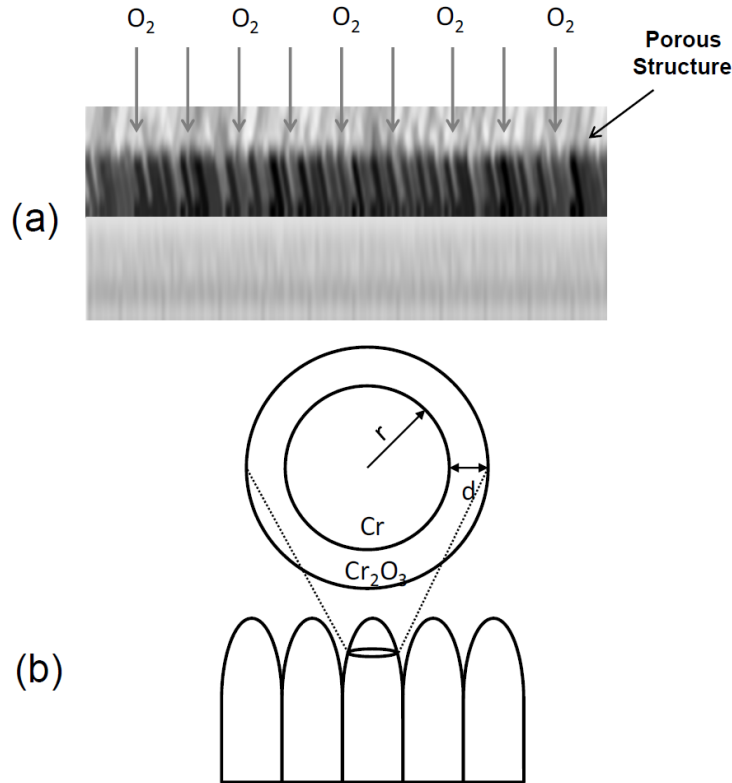


Figure 3-6 (a) Schematic of oxidation of porous chromium thin film after exposure to air; (b) Schematic of porous columnar grains surrounded by a thin oxide layer.

The XPS signal is generated at a very shallow depth (less than 10 nm) below the surface. Since the ends of the columnar grains would be oxidized the measured oxygen concentration without any sputter cleaning would be very high. However, after sputter-cleaning the metal core is revealed and measured oxygen concentration decreases significantly. With the above assumptions, the atomic concentration of Cr and O can be expressed based on the core/shell area and density by the following equation:

$$\frac{\text{at.\% Cr}}{\text{at.\% O}} = \frac{\rho_{Cr} \times A_{Cr} + 0.4 \times \rho_{Cr_2O_3} \times A_{Cr_2O_3}}{0.6 \times \rho_{Cr_2O_3} \times A_{Cr_2O_3}} \quad (3-1)$$

where $\frac{\text{at.\% Cr}}{\text{at.\% O}} = 5.74$ from XPS measurements after 4 min of sputtering (13.8 % O, 79.2 % Cr), A is the cross-section area, $\rho_{Cr} = 7.19 \text{ g/cm}^3$ and $\rho_{Cr_2O_3} = 5.22 \text{ g/cm}^3$. The average radius of grains, r, is estimated to be 15 nm. The thickness of the oxide layer is calculated to be ~ 3 nm for columnar grains with a diameter of 30 nm. This approximate value is reasonable for a native oxide thickness. In this calculation we have assumed that all of the oxygen, both in the as-deposited film and from exposure to air, goes toward formation of the Cr_2O_3 .

3.4 Optical Properties

In order to further investigate the properties of Cr films grown at high pressure, optical measurements were performed using variable angle spectroscopic ellipsometry (VASE). Amplitude ratio, Ψ , and phase difference, Δ , of the reflected light from chromium thin films sputtered on silicon substrates were measured from 1.5 to 4.1 eV. Assuming that the oxide was mixed with chromium metal in the films deposited at high pressures, the Effective Medium Approximation (EMA) model was used to fit the data from a 10-nm-thick film deposited on a silicon substrate at 0.93 Pa deposition pressure. The model consisted of a Si substrate, a native oxide layer and a flat metal layer which is mixed with metal oxide. Two constituents were chosen for the EMA model: chromium bulk and chromium oxide (Cr_2O_3). The fraction of chromium oxide was chosen as the fit parameter. The result of the fit showed that a film with a mixture of 35% Cr_2O_3 and 65% bulk Cr would present the same optical properties as those measured by ellipsometry, proving that the films deposited at 0.93 Pa consists of a mixture of metal and oxide. The measured and model dispersion curves are shown in Figure 3-7. The approximate atomic percentage of oxygen in the film was calculated to be 21 percent from the estimated fraction of Cr_2O_3 . This estimate is

in agreement with the measured oxygen concentration from XPS analysis.

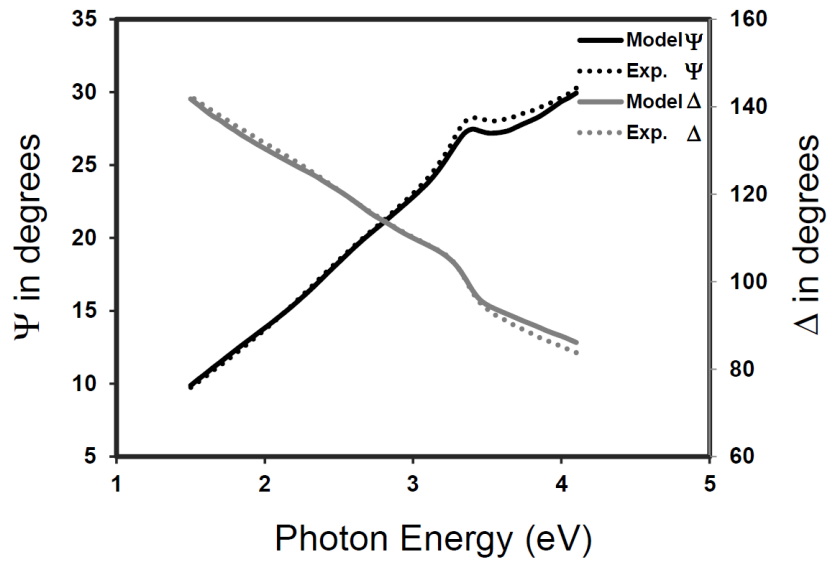


Figure 3-7 Comparison of the measured and model dispersion curves for 10 ± 1 nm Cr films grown at 0.93 Pa.

In an attempt to investigate the effect of sputtering pressure on the optical properties of Cr thin films, the optical properties of Cr films sputtered at 0.13, 0.39 and 0.93 Pa pressures were measured using spectroscopic ellipsometry data. Figure 3-8 shows the refractive index (n) of the Cr thin films sputtered at different pressures. It can be seen that the refractive index decreased as the sputtering pressure is increased. For the film deposited at 0.13 Pa pressure, the refractive index is very close to the bulk value. The data presented in Table 3-3 shows the refractive index of the sputtered films at 633 nm (1.96 eV). Comparing the refractive index of thin films with that of the bulk can give indirect information about the density of the films [21, 22]. This confirmed that Cr films deposited at lower sputtering pressures have a denser structure compared to films deposited at higher pressures.

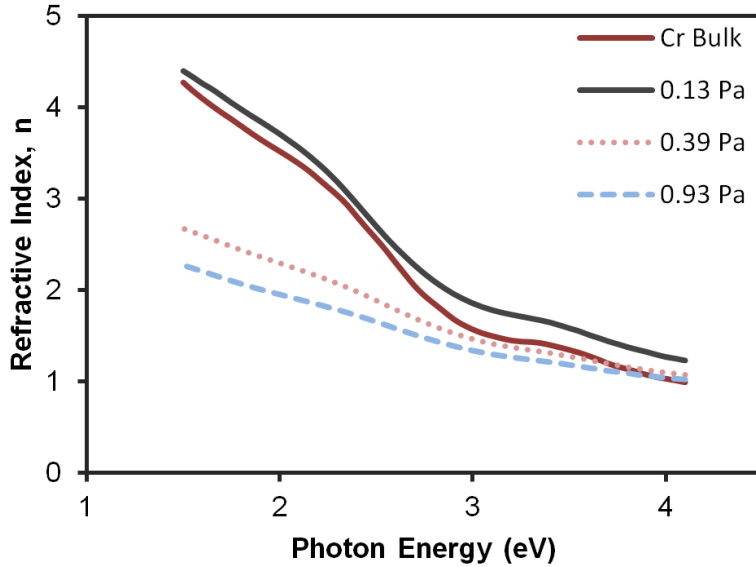


Figure 3-8 Optical properties of Cr thin films deposited at different sputtering pressures

Table 3-3 Refractive index (n) of chromium thin films sputtered at different sputtering pressures

| Deposition Pressure (Pa) | Refractive Index (n) at 633 nm |
|--------------------------|--------------------------------|
| 0.13 | 3.47 |
| 0.39 | 2.33 |
| 0.93 | 1.97 |
| Cr Bulk | 3.58 |

Transmittance and reflectance measurements also provide indirect information about film density. Figure 3-9 shows the transmittance and reflectance of Cr thin films sputtered on glass slides at different pressures as a function of photon energy. Transmittance is defined here as the ratio of the light that passes through the film to the original beam intensity. The data showed that the films sputtered at higher pressures transmitted more light and reflected less compared to the films sputtered at lower pressures. This also confirmed that the sputtering pressure had a strong effect on the film density.

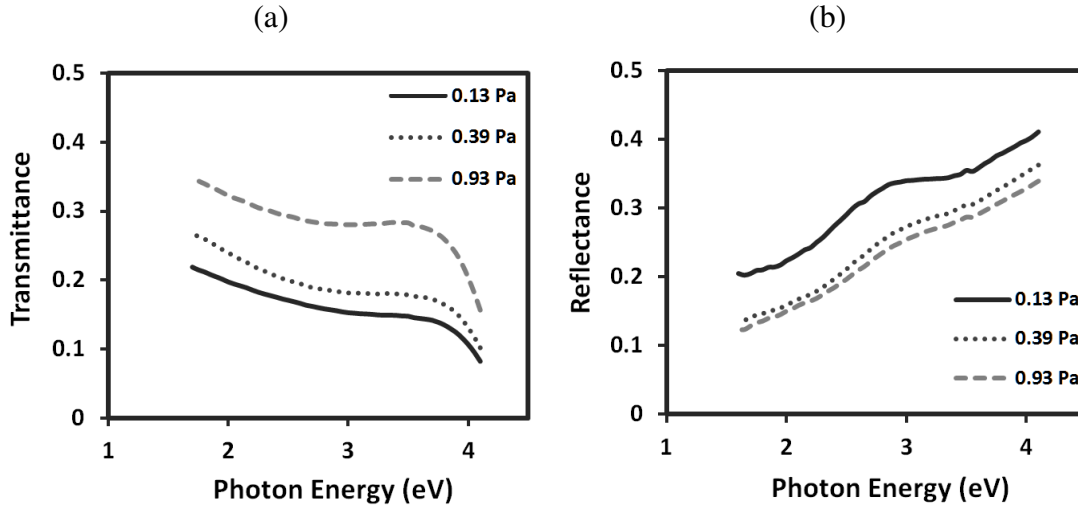


Figure 3-9 Transmittance and reflectance of Cr thin films deposited at different sputtering pressures

3.5 Conclusions

It was shown that sputtered Cr thin films contain two sources of oxygen, one from residual oxygen in the vacuum chamber, and the other from exposure to air. It was shown by calculation and XPS that the residual oxygen in Cr films was approximately 8 at.% O in a deposition system with a base pressure of 4.0×10^{-5} Pa. Calculations showed that in the 3.2×10^{-4} Pa base pressure system the residual oxygen was much higher. This difference in residual oxygen explained the difference in film resistivity between the two systems. Investigation of films grown in the 4.0×10^{-5} Pa base pressure system showed that the oxygen incorporated due to air exposure is influenced by the microstructure of the film which is in turn determined by the sputtering pressure [9, 10]. Resistivity also increased as the Ar sputtering pressure increased. Films grown below 0.3 Pa had a dense structure and only formed a surface native oxide when exposed to air. However, films formed at higher pressures were porous and upon exposure to air the internal structure of the film formed a thin native oxide layer. A simple model was used to calculate the thickness of the thin oxide layer. The data from XPS

measurements confirmed that oxygen, up to 24 at.% O, was incorporated into the film structure. Optical measurements also proved that the films deposited at high sputtering pressures were porous.

3.6 References

- [1] C.W. Tan, J.M. Miao, *Thin Solid Films* 517/17 (2009) 4921.
- [2] E. Fawcett, *Rev Mod Phys* 60/1 (1988) 209.
- [3] E. Fawcett, H.L. Alberts, V.Y. Galkin, D.R. Noakes, J.V. Yakhmi, *Rev Mod Phys* 66/1 (1994) 25.
- [4] Z. Boekelheide, E. Helgren, F. Hellman, *Phys Rev B* 76/22 (2007).
- [5] Z. Boekelheide, D.W. Cooke, E. Helgren, F. Hellman, *Phys Rev B* 80/13 (2009).
- [6] M.A. Elhiti, M.A. Ahmed, M. Elshabasy, *J Mater Sci Lett* 8/3 (1989) 329.
- [7] A.K. Kulkarni, L.C. Chang, *Thin Solid Films* 301/1-2 (1997) 17.
- [8] M.A. Angadi, L.A. Udachan, *J Mater Sci* 16/5 (1981) 1412.
- [9] J.A. Thornton, *J Vac Sci Technol* 11/4 (1974) 666.
- [10] J.A. Thornton, *J Vac Sci Technol* 12/4 (1975) 830.
- [11] R. Messier, A.P. Giri, R.A. Roy, *J Vac Sci Technol A* 2/2 (1984) 500.
- [12] P.B. Barna, M. Adamik, *Thin Solid Films* 317/1-2 (1998) 27.
- [13] D.W. Hoffman, J.A. Thornton, *Thin Solid Films* 40/Jan (1977) 355.
- [14] J.A. Thornton, D.W. Hoffman, *J Vac Sci Technol* 14/1 (1977) 164.
- [15] D.W. Hoffman, J.A. Thornton, *Thin Solid Films* 45/2 (1977) 387.
- [16] J.A. Thornton, *Annu Rev Mater Sci* 7 (1977) 239.
- [17] S.P. Murarka, *Metallization, Theory and Practice for VLSI and ULSI*, Butterworth-Heinemann, Stoneham, MA, 1993.
- [18] L.I. Maissel, R. Glang, in: H. Frey, H.R. Khan (Eds.), *Handbook of Thin Film Technology*, McGraw-Hill Inc., New York, NY, 1970.
- [19] A. Foroughi-Abari, C. Xu, K.C. Cadien, *Thin Solid Films* (2011).

- [20] Y. He, Z. Li, H. Qi, W. Gao, *Materials Research Innovations* 1/3 (1997) 157.
- [21] D.E. Aspnes, *Thin Solid Films* 89/3 (1982) 249.
- [22] D. Mergel, D. Buschendorf, S. Eggert, R. Grammes, B. Samset, *Thin Solid Films* 371/1-2 (2000) 218.

Chapter 4 ALD of Oxides on Metal Substrates *

4.1 Introduction

Fundamental understanding of the deposition of nanometer thick oxides for device applications is extremely important and has been investigated by many researchers in the field [1-3]. These oxides are deposited on silicon for metal oxide silicon (MOS) applications, on gallium nitride and gallium arsenide for metal oxide field effect transistor (MOSFET) applications, and on metal substrates for metal-insulator-metal (MIM) devices. However, native oxides on the substrate can affect the performance of these devices since this oxide affects the capacitance of the dielectric stack [1, 4-6]. Substrate pre-treatments have been developed to limit the formation of native oxide [5, 6]. The focus of this chapter is on the atomic layer deposition (ALD) of aluminum oxide, hafnium oxide, and zirconium oxide on metallic thin films with a special attention to deposition of aluminum oxide on chromium metal. Chromium and aluminum oxide are good candidate materials for MIM devices since sputtered chromium thin films have smooth surfaces required for MIM electrodes and aluminum oxide has excellent dielectric properties and good adhesion to many surfaces [1].

* A version of this chapter has been published in:
A. Foroughi-Abari, K. Cadien, *Journal of The Electrochemical Society*, 159 (2), 2012

ALD is a thin film deposition technique based on self-limiting surface chemical reactions that is capable of producing dense, uniform and conformal films. ALD film growth consists of a number of sequential cycles; each involves pulsing of two precursors into the reaction chamber one after the other. The precursors react at the surface to form a monolayer (or sub-monolayer) of the desired material after completion of each cycle. In thermal ALD, the energy required for reactions is provided by heating the substrate to a temperature usually between 100 and 400°C, i.e. the so called ALD window [7]. For deposition temperatures below the ALD window, there is not enough energy for reactions to take place and the film contains a lot of impurities [8]. Additionally, some emerging applications require lower process temperatures due to heat-sensitive substrates such as polymers, organic materials and photoresist used in lift-off processes. Plasma enhanced ALD (PEALD) can be used for such applications. In PEALD, a plasma is used to generate highly reactive radicals and ions which enhance the surface reactions and allow reactions to occur at much lower substrate temperatures. Successful film deposition at temperatures as low as room temperature has been reported [3, 9-11].

One of the areas that can potentially benefit from PEALD is the fabrication of MIM diodes, since they require the deposition of very thin (1 to 3 nm), high quality dielectric material between two metal electrodes. Some researchers have recently started to use ALD to fabricate MIM diodes [12]. It is important to study the growth behavior of ALD oxides on metal surfaces and the possible surface changes that occur as a result of ALD film nucleation and growth. There exist very little published data on ALD growth characteristics of oxides on metal surfaces. George et al. [1] briefly described the thermal ALD growth of aluminum oxide on various metal substrates similar to the growth on HF-etched Si (100) and on the native oxide SiO₂ layer. However the metal films they used as substrates were prepared by E-beam evaporation and sputtering and were exposed to air prior to being put in the ALD reaction chamber.

Spectroscopic ellipsometry (SE) is an optical technique that is widely used for precise determination of the film thickness and optical properties over a wide spectral range [13]. In principle, spectroscopic ellipsometry is able to detect changes in the thickness of surface layers equivalent to 0.01 monolayers [14]. This level of sensitivity makes SE ideal for *in-situ* analysis of film nucleation and growth during the ALD process. The application of *in-situ* ellipsometry to study the growth of ALD films has been adapted by a growing number of research groups [14-17] .

In this work, *in-situ* ellipsometry is used to study the thermal and plasma enhanced ALD growth of metal oxides on metal substrates and show that the ALD process itself causes oxidation of the substrate; techniques to eliminate this oxide are also discussed.

4.2 Experimental

4.2.1 Sample Preparation

Experiments were done in an ALD research system consisting of a Kurt J. Lesker ALD 150 LX system integrated with a CMS 18 sample preparation chamber via a load lock as shown in Figure 4-1. The ALD system can accommodate up four precursors and is capable of both thermal and plasma ALD. The plasma emanates from a continuous-flow inductively coupled remote source. The ALD chamber is equipped with an *in-situ* J. A. Woollam M-2000DI ellipsometer which has a fixed angle of 70° with respect to the substrate. The sample preparation chamber has a sputter source and ion cleaning capability. Samples can be transferred from the sample preparation chamber to the ALD reactor while under vacuum.

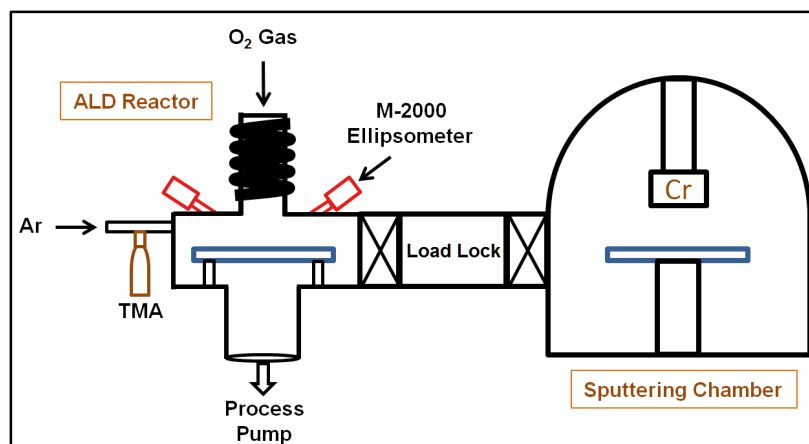


Figure 4-1 Schematic of the equipment used for the experiments.

Metallic films, approximately 10 nm thick, were grown on silicon substrates in the sample preparation chamber by DC magnetron sputtering at an argon pressure of 0.22 Pa and a power of 300 W. The base pressure of the sputtering chamber was $<1.3 \times 10^{-5}$ Pa and the purity of the argon sputter gas was 99.999 %. The silicon substrates had a native oxide that was approximately 1.5 nm thick. The samples were then transferred into the ALD chamber through the load lock without breaking the vacuum. The vacuum transfer helped minimize surface contamination and oxidation of the pristine metal surfaces.

FTIR measurements were performed using a Nicolet 8700 system operating in reflectance mode on 5-nm aluminum oxide films deposited on optically thick chromium films. The reflectance measurements were referenced against a gold background.

4.2.2 Analysis

Spectroscopic ellipsometry (SE) was used to determine the precise thickness of the dielectric layer and to monitor any changes to the metal surface due to oxygen plasma exposure. Ellipsometry is based on the accurate measurement of the

changes in the polarized light upon reflection on a sample [13]. The ellipsometry measures two values: the amplitude ratio Ψ and phase angle Δ . They are defined by the amplitude ratio of the amplitude reflection coefficients for p- and s-polarizations based on the following equation:

$$\rho = \frac{r_p}{r_s} = \tan \Psi e^{i\Delta} \quad (4-1)$$

where r_p and r_s are the amplitude reflection coefficients and ρ is the complex reflectance ratio [13]. The extraction of the optical constants (n, k) or thickness of a simple single-layer structure can be done using the Fresnel equations. For more complex structures the physical data can be extracted through model-based analysis and fitting of the experimental data. The ellipsometer used in the experiments was an M-2000DI from J. A. Woollam with a wide spectral range of 193 to 1700 nm (0.73 to 6.43 eV) and capable of simultaneous CCD detection of all wavelengths with a fast data acquisition speed of 20 dispersion measurements per second.

In order to measure the ALD film thickness deposited on the metal surfaces, the exact thickness and optical constants of the metal layers was required. The optical constants of metal films strongly depend on how the films were prepared. In the case of sputtering, the deposition pressure is one of the key factors that significantly influence the optical properties. Here, the sputtering process was performed at a low sputtering pressure of 0.23 Pa to obtain metal films with optical properties close to the bulk values. Since the optical constants and the exact thickness of the metal layers were unknown, a coupling technique was used which is described in detail in [18]. The reason for using thin metal layers (10 nm) instead of thick layers is that when the metal layer is thin enough, the light can reach the lower interface and, therefore, the SE measurements will be sensitive to the thickness changes of the metal layer. Once the optical constants and thickness of the metal layers were determined, measuring the thickness of the dielectric layer grown by ALD was relatively straightforward.

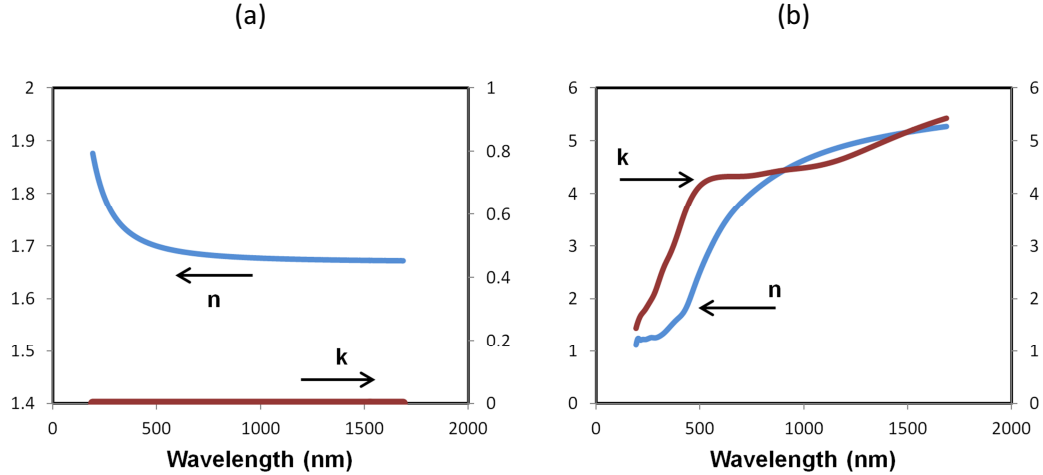


Figure 4-2 Optical dispersion curves for aluminum oxide (a) and chromium (b) thin films.

The general SE model that was used for thickness measurements consisted of a Si substrate at the bottom, 1.5 nm of silicon native oxide, 10 nm of metal layer, a thin layer of metal oxide (which may form due to oxygen exposure during ALD) and the dielectric layer grown by ALD on the top. The thicknesses of the three top layers were the fitting parameters during the analysis. All SE measurements were performed at wavelengths ranging from 193 to 1700 nm. In order to accurately separate the ALD oxide from the metal native oxide, the thickness of the native oxide layer was coupled with the thickness of the metal layer.

To describe the optical properties of aluminum oxide, a standard Cauchy dispersion relation was used:

$$n = A_n + \frac{B_n}{\lambda^2} + \frac{C_n}{\lambda^4}, k = 0 \quad (4-2)$$

where A_n , B_n and C_n are the Cauchy fit parameters and λ is the wavelength in nm. The complex multilayer structure of a sample can be analyzed by SE provided that the optical constants of the layers showed measurable differences. This made it possible to accurately measure the thickness variation of a dielectric layer on top of a metal layer. Additionally, coupling the thickness of the metal oxide layer (Cr_2O_3) layer to the metal (Cr) layer based on the physical fact that the metal

needed to be consumed for the formation of its oxide made the distinction more accurate.

4.3 Results and Discussion

4.3.1 Optical Properties

In order to accurately describe the optical properties of aluminum oxide films deposited by ALD, a standard Cauchy model was used. A typical optical dispersion curve for aluminum oxide deposited at 200 °C is presented in Figure 4-2a. The fit parameters for the Cauchy model were $A_n=1.67$, $B_n=0.0075 \mu\text{m}^2$ and $C_n=0$. The refractive index of aluminum oxide at 633 nm is 1.68 which is very close to the published values for aluminum oxide thin films prepared by ALD [14, 19]. Figure 4-2b shows the optical constants of sputtered Cr thin films. It was assumed during the optical modeling that the surface of the chromium films as well as the aluminum oxide films were flat with negligible surface roughness. This assumption was based on the AFM measurements on sputtered chromium films and also ALD grown aluminum oxide films which proved that the films were smooth as shown in Figure 4-3. The root mean square (RMS) roughness for sputtered Cr thin films was 0.2 nm. The surface of the films did not show noticeable difference in the RMS roughness after depositing 5 nm of Al_2O_3 by ALD (Figure 4-3b).

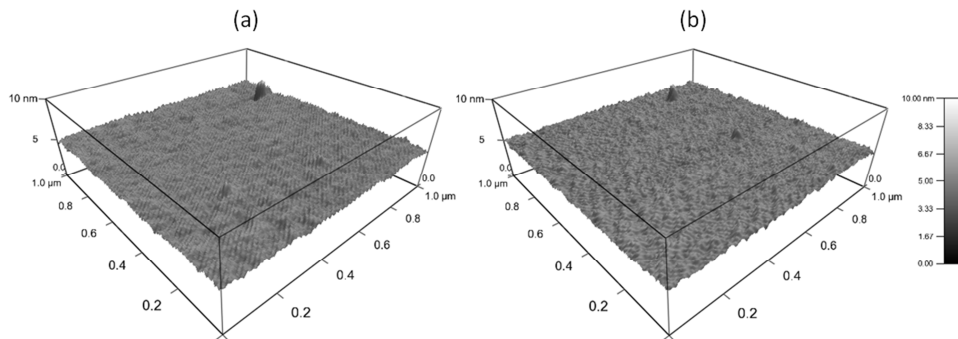


Figure 4-3 AFM images of Cr thin film surface (10 nm thickness) before (a) and after (b) the ALD of Al_2O_3 (5 nm).

4.3.2 Metal Oxidation under Plasma Exposure

The first step to characterize the PEALD growth behavior of dielectric materials on metal surfaces was to investigate the possible effects of oxygen plasma exposure on the structure of the metal surfaces. Therefore, the prepared metal layers were exposed to oxygen plasma for several minutes to observe the changes. The effect of plasma exposure on the surface of chromium layer is presented in Figure 4-4. Initially the thickness of the chromium layer was about 9 nm without any surface oxide. After 60 s, oxygen gas started to flow inside the chamber with a flow rate of 60 sccm which increased the chamber pressure to 147 Pa. As a result of reaction between O_2 gas and Cr, a thin Cr oxide layer formed, while the Cr metal layer was consumed (as seen by a small decrease in the metal thickness). This was a thermal oxidation process that was clearly self-limiting. The initial rate of oxidation was relatively high due to rapid reaction of gaseous oxygen with the bare metal surface. Once an oxide layer was formed, additional oxidation required diffusion of oxygen (or metal) through the oxide layer. As the oxide layer grew thicker the flux of oxygen or chromium through the oxide decreased significantly because it took longer for individual particles to diffuse through the layer.

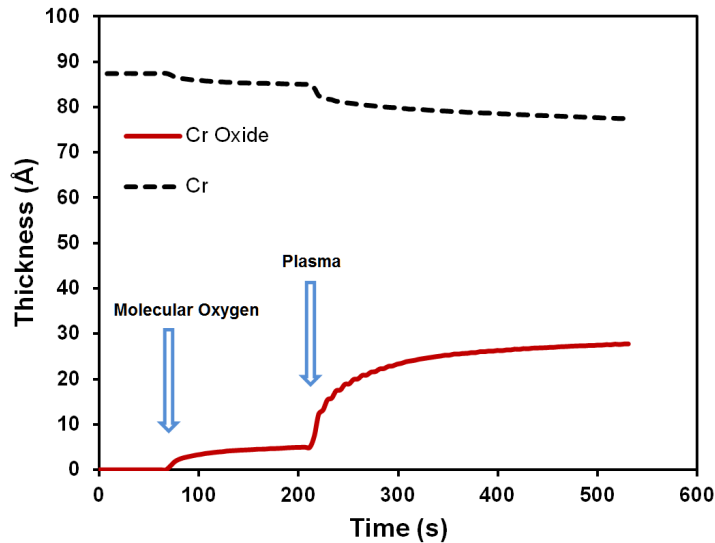


Figure 4-4 Oxidation of Cr film under oxygen plasma at 100°C.

Once the plasma was ignited at approximately 210 s, rapid oxidation occurred as seen by the sharp change in the thickness of the Cr oxide layer and the noticeable drop in the metal thickness. The increase in the oxidation rate after exposure to plasma was caused by a number of factors such as production of highly reactive oxygen species, ion implantation of oxygen in the oxide layer and modification of charge transfer. Oxidation in the presence of plasma is generally a complex phenomenon; additional energy may be transferred to the deposition surface from the remote plasma which could facilitate the diffusion of oxygen species through the oxide layer and the plasma environment could affect the rate of charge transfer through the oxide layer leading to higher oxidation rates [20, 21]. Similar to thermal oxidation, the plasma oxidation rate slows as the film gets thicker.

In order to investigate the effect of plasma exposure on the surface of other metals, the same experiment was performed on several sputtered metallic thin films. Figure 4-5 shows the oxidation behaviour of Ni, Cr, Ta, Zr, and Ag metals exposed to oxygen plasma at a substrate temperature of 100°C. The trend for Zr, Ta, and Ni metals appeared to be similar to oxidation of Cr. They all have a relatively fast oxidation rate followed by a slow one. The main difference was in the final oxide thickness and the time it took for the oxidation curve to level off. The most noticeable difference was observed for the case of silver oxidation. The experiment showed that the whole silver layer turned into silver oxide within a few seconds. The reason for this catastrophic oxidation was linked to the properties of silver oxides. The reaction of molecular oxygen with silver results in formation of Ag₂O; however in presence of atomic oxygen, AgO is formed based on the following reaction [22-24]



Thermodynamic calculations can be found in [22]. This oxide was not dense enough to act as a protective layer. The presence of micro-pores and defects in the oxide layer promoted the diffusion of oxygen species to reach the metal-oxide

interface. Unlike silver, the rest of the metals in the experiment formed protective oxide layers that decreased the oxidation rate significantly.

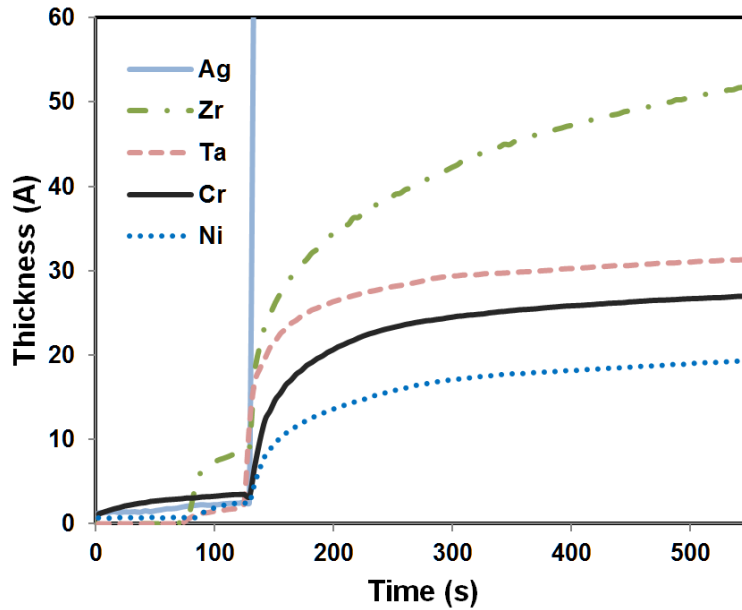


Figure 4-5 Oxidation of various metals under oxygen plasma exposure at 100°C

Figure 4-6 depicts a simple schematic view of the oxidation process in metals. It involves both ionic and charge transport through the forming oxide layer. Various kinetic theories exist that intend to explain the oxidation of metals [25]. The simplest model considers only the diffusion of particles through the oxide layer which gives the well-known parabolic growth law:

$$L(t)^2 - L(0)^2 = 2kt \quad (4-4)$$

where L is the oxide thickness, t is time, and k is the rate constant. The parabolic growth law is derived from Fick's law of diffusion. An extension to the parabolic law would include a linear reaction-controlled regime at the beginning of the oxidation leading to linear-parabolic growth models such as Deal-Grove model [26]. Although the parabolic growth has been observed in many metal oxidation process, for low temperature oxidation or in the presence of plasma it may not give accurate results. In such conditions, other models must be considered. The

Cabrera-Mott model can be used to describe the growth of thin oxides on metal surfaces at low temperatures. It states that since the temperature is not high enough for thermionic emission to occur, the electrons must transfer through the oxide via quantum-mechanical tunneling. This limits the thickness of the growing oxide to a few tens of angstroms. The ionic current J_i is given by the following equation [25]:

$$J_i = 2n_i v_i \exp\left(-\frac{W_i}{k_B T}\right) \sinh\left(-\frac{q_i a V_m}{k_B T L}\right) \quad (4-5)$$

where n_i is the number of ions per unit area, W_i is the rate-limiting energy barrier, V_m is the Mott potential, v_i is the attempt frequency, $2a$ is the ionic jump distance, q_i is the charge per particle, k_B is the Boltzmann constant, and T is the absolute temperature. The Mott potential, V_m is defined as

$$e^{-1}(\phi_O - \phi_L) \quad (4-6)$$

where e is the magnitude of the electron charge, ϕ_O is the metal work function, and ϕ_L is the difference between the vacuum potential and the O^- levels on the oxide surface. Since the oxidation rate is related to the Mott potential, the metal work function can affect the oxidation rate. The work function energies for Zr, Ta, Cr, and Ni metals are shown in Table 4-1. It can be seen that the metals with lower work functions had a higher oxidation rate compared to those with higher work functions. However, it must be noted that this may not be a general trend for all the metals and other parameters such as grain size, roughness, film density, and oxide properties could also affect the oxidation process. Further experiments must be conducted to draw general conclusions.

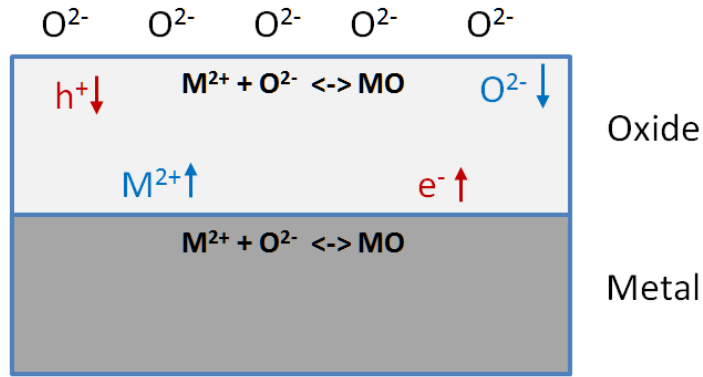


Figure 4-6 Schematic general representation of metal oxidation

Table 4-1 Work function energy for Zr, Ta, Cr, and Ni meals

| Metal | Work Function |
|-------|---------------|
| Zr | 4.05 |
| Ta | 4.25 |
| Cr | 4.5 |
| Ni | 5.15 |

Based on the ionic current, J_i in equation (4-5), the relationship between the growing oxide thickness (L) and time (t) can be expressed using the Ghez approximation [27]:

$$\frac{L^*}{L} = -\ln \left[\frac{(t+\tau)}{L^2} \right] - \ln(L^*u) \quad (4-7)$$

$$u = n_i \Omega v_i \exp \left(-\frac{W_i}{k_B T} \right) \quad (4-8)$$

$$L^* = |q_i a V_m / (k_B T)| \quad (4-9)$$

where u is defined as the characteristic velocity and L^* is the characteristic distance [28]. Ω is the volume of oxide per ionized atom and τ is a time constant. Equation (4-7) shows that a linear relation exists between the $\frac{1}{L}$ and $\ln \left(\frac{t}{L^2} \right)$. Figure 4-7 shows the plot of $\ln \left(\frac{t}{L^2} \right)$ as a function of $\frac{1}{L}$ for Ta,

Cr, and Ni metals (from oxidation data in Figure 4-5). A linear fit was performed to determine the slope which is the characteristic distance, L^* . Using $L^* = |q_i a V_m / k_B T|$ and assuming $q_i=2$, $a=1.5\text{\AA}$, $T=373\text{K}$, the Mott potential, V_m was calculated to be 2.4V, 1.3V, and 0.7V for Ta, Cr, and Ni oxidation.

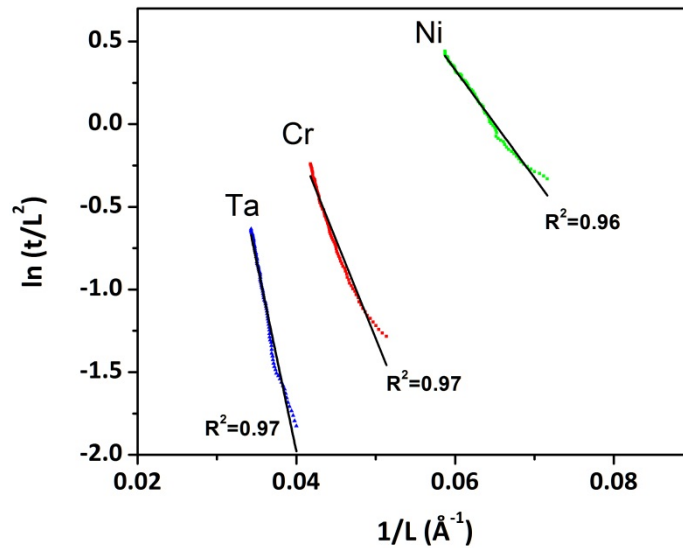
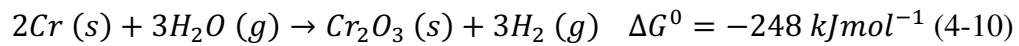


Figure 4-7 Plot of oxide growth for Ta, Cr, and Ni metals during oxygen plasma oxidation based on the Ghez approximation.

4.3.3 Growth of Aluminum Oxide

Figure 4-8 shows the results of *in-situ* ellipsometry of PEALD of Al_2O_3 on a chromium surface using TMA precursor and oxygen plasma. The depositions were both carried out at 100 °C for 50 ALD cycles. In the first experiment, Figure 4-8a, the deposition started with a TMA pulse. Each ALD cycle had 20 ms of TMA pulse and 1 s of oxygen plasma pulse. The top horizontal axis shows the ALD cycles starting from 0 (start of the ALD process) and up to 50 cycles. Each ALD cycles takes 9 seconds to complete. The first rise in the thickness of Cr oxide is due to the thermal oxidation as discussed earlier. More interestingly, during the first few ALD cycles, Cr oxide thickness increased as a result of

exposure to the oxygen plasma. A small but noticeable drop is also seen in the thickness of the Cr layer. The oxidation stops at some point due to the formation of a critical thickness of Al₂O₃ on the surface which inhibits further diffusion of oxygen atoms to the metal layer. The aluminum oxide film was grown with a growth per cycle of 1.5 Å/cycle. No noticeable difference was observed between the growth characteristics of Al₂O₃ on Si (100) and Cr surface. In the second experiment, Figure 4-8b, all the process conditions were the same except the ALD process was initiated with plasma oxygen exposure instead of a TMA pulse. In this case, Cr oxide is much thicker than in Figure 4-8a. If aluminum oxide is grown on Cr by thermal ALD, using water instead of plasma oxygen, no metal oxidation is observed, as shown in Figure 4-9. The reaction between H₂O and Cr is thermodynamically possible at this temperature:



However, due to high barrier energy the reaction kinetics are very slow. Thermal ALD has the advantage of leaving the Cr surface unchanged during the growth of Al₂O₃. However, if the process is limited to low deposition temperatures, such as the case of any device fabrication which involves the lift-off process, PEALD may give superior results in terms of the film quality and levels of impurity [2].

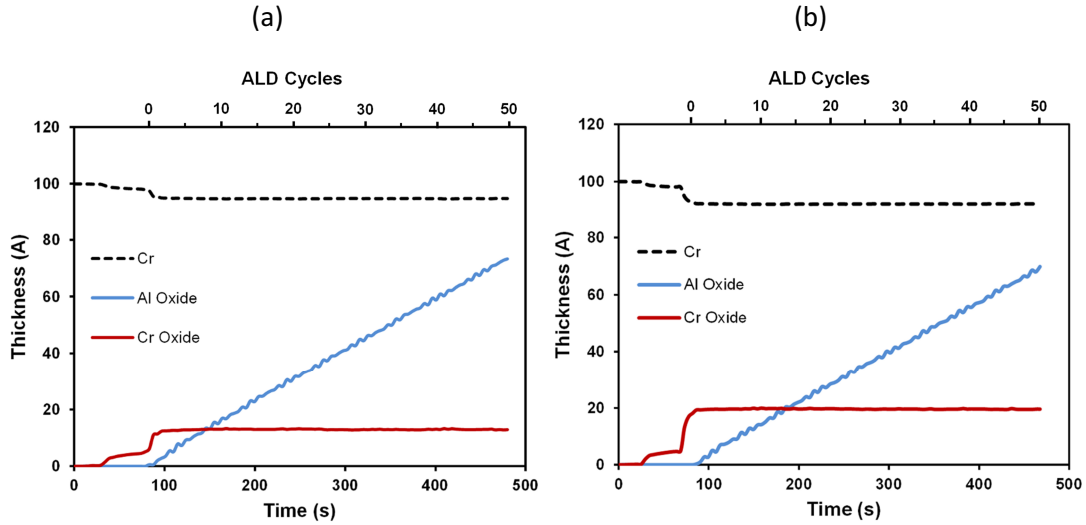


Figure 4-8 Growth of aluminum oxide on Cr surface; (a) ALD cycles started with TMA pulse; (b) ALD cycles started with plasma exposure.

The results show that a thin layer of Cr oxide is formed during the PEALD of Al_2O_3 on a Cr surface. In order to investigate the role of the plasma on the oxidation process, the plasma pulse duration was varied between 0.5 and 4 seconds, keeping all other parameters constant. Figure 4-10 shows the oxidation of Cr surface during PEALD of Al_2O_3 at different plasma exposure durations. The exposure time appears to have a noticeable effect on the amount of oxidation. The longer plasma pulse grows a much thicker Cr oxide. As shown in Figure 4-4, during continuous exposure of a Cr thin film to oxygen plasma it takes a long time (100s) for the growth rate of the Cr oxide to level off. During the ALD of Al_2O_3 there is a competition between the oxidation of the Cr and the growth of the Al_2O_3 . When the oxygen pulse is short, only a thin layer of Cr oxide is formed underneath the Al_2O_3 after each ALD pulse. This occurs until the Al_2O_3 reaches a critical thickness as described above. For longer plasma oxygen pulses the Cr oxide layer formed per pulse is thicker while the growth rate of the Al_2O_3 is the same as for shorter oxygen pulses, hence a much thicker Cr oxide forms.

In an attempt to minimize the formation of Cr oxide during PEALD of Al_2O_3 , the Cr surface was first covered with 0.5 nm of Al_2O_3 grown by thermal ALD (6

cycles). Then PEALD at a temperature of 100 °C was started with cycles each having 20 ms of TMA pulse and 0.5 s of oxygen plasma exposure. The result is presented in Figure 4-11. The ultra-thin aluminum oxide layer acted as an effective diffusion barrier to stop the oxidation of the Cr surface once the PEALD started.

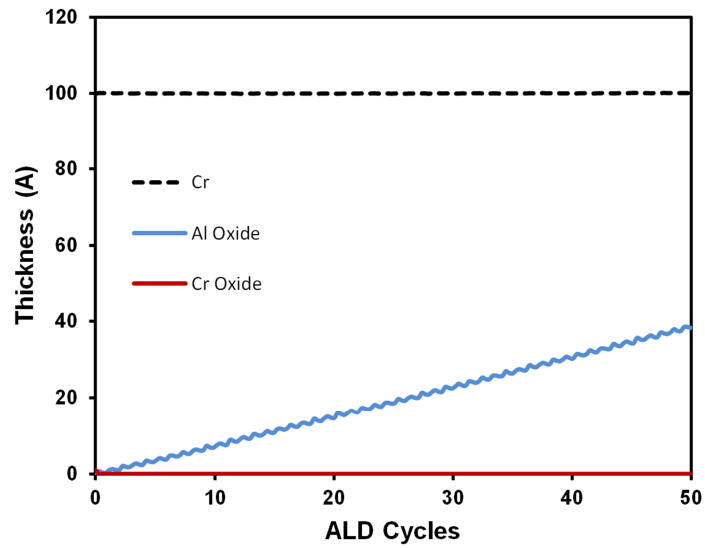


Figure 4-9 Thermal ALD of aluminum oxide on Cr surface at 100°C.

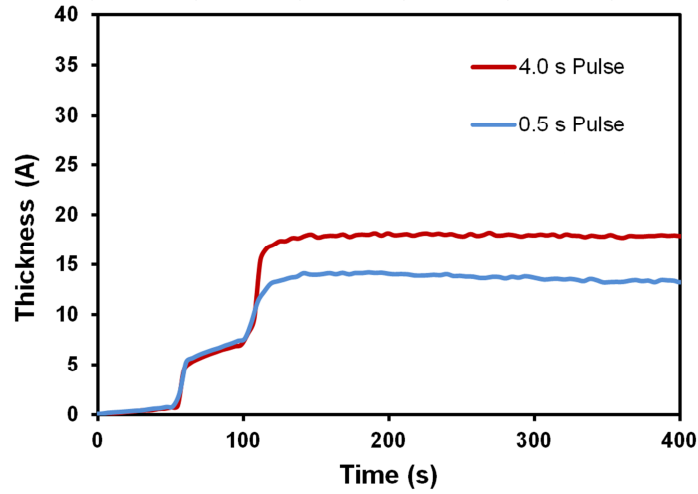


Figure 4-10 Effect of plasma exposure time on oxidation of Cr surface during PEALD of aluminum oxide.

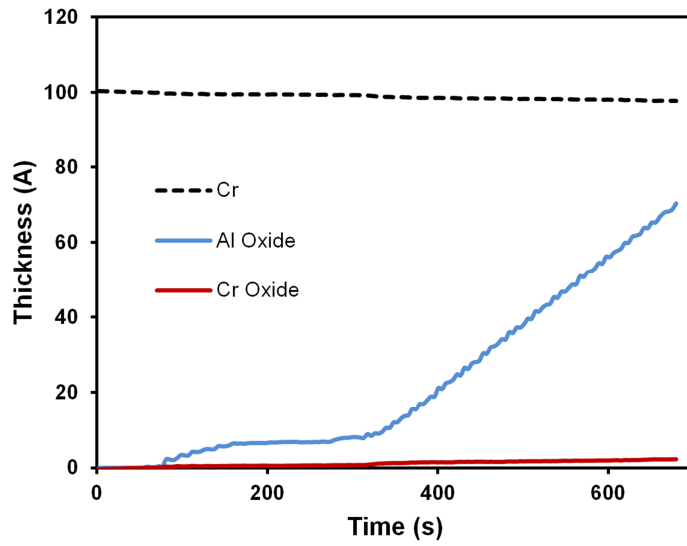


Figure 4-11 ALD started with 6 cycles of thermal aluminum oxide deposition.

In order to study the effect of deposition temperature on oxidation of Cr surface during PEALD of Al_2O_3 , the measurements were repeated at different temperatures. The results, summarized in Table 4-2, show that as the deposition temperature increases, a thicker Cr oxide layer is formed.

Table 4-2 Effect of deposition temperature on oxidation of Cr.

| Deposition Temperature, °C | Cr Oxide Thickness Å | Growth per Cycle Å/Cycle |
|----------------------------|----------------------|--------------------------|
| 25 | 9 ± 2 | 1.86 ± 0.04 |
| 100 | 14 ± 2 | 1.57 ± 0.05 |
| 200 | 20 ± 3 | 1.30 ± 0.06 |
| 300 | 25 ± 4 | 1.12 ± 0.07 |

In order to explain the data, the plasma oxidation phenomenon must be examined more closely. During the oxidation process, the following reaction takes place at the metal surface:



As the oxide grows, the oxygen atoms need to diffuse through the oxide layer and reach the metal/oxide interface for the oxidation to proceed. The self-limiting oxide growth (Figure 4-4) is due to the fact that the diffusivity of oxygen atoms through the oxide layer is significantly slowed once the oxide layer reaches a certain thickness. However, when ALD deposition is occurring concurrently with oxidation there is a competition between the growth of ALD oxide and the substrate metal oxide, in this case between Al₂O₃ and Cr₂O₃. The ALD oxide reduces the flux of oxygen diffusion since the oxygen needs to diffuse through the growing Al₂O₃ layer as well as the Cr₂O₃ layer (Figure 4-12). This explains why a thinner Cr₂O₃ layer is formed during the ALD (Figure 4-8) compared to the Cr₂O₃ layer formed as the result of the direct oxygen plasma exposure (Figure 4-4).

As the deposition temperature increases, two main conditions change. Firstly, the diffusion of oxygen through the oxide layer is enhanced due to thermal activation, as shown by:

$$D = D_0 e^{\left(\frac{-E_a}{RT}\right)} \quad (4-12)$$

where D is the diffusion coefficient, D_0 is the maximum diffusion coefficient (at infinite temperature), E_a is the activation energy and T is the temperature. Secondly, the Al_2O_3 growth per cycle decreases as the temperature is raised (Table 4-2). Therefore, at higher temperatures, oxidation of Cr occurs at a higher rate and at the same time the growth rate of ALD Al_2O_3 , which acts as a diffusion barrier, is decreased. The net effect is that a thicker Cr_2O_3 layer is formed during ALD film growth as can be seen in Table 4-2.

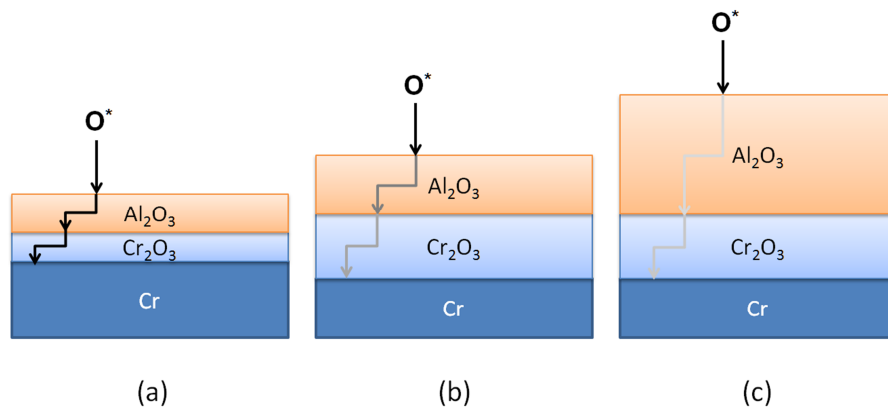


Figure 4-12 Schematic of radical oxygen diffusion through growing Al_2O_3 and Cr_2O_3 layers. As the ALD film grows, the available oxygen for reaction at the Cr surface decreases until there is very little oxygen available to react with Cr.

The same experiment was performed using several other metals. The results, summarized in Table 4-3, show that the thickness of the interfacial layer follows the trend observed in the pure plasma oxidation experiment (Figure 4-5).

Table 4-3 Thickness of interfacial oxide layer formed during the PEALD of Al_2O_3 on various metals. The deposition temperature was 100°C .

| Metal | Zr | Ta | Cr | Ni | Au |
|--|----|----|----|----|----------|
| Interfacial Oxide Thickness (\AA) | 25 | 20 | 14 | 9 | ~ 0 |

4.3.4 Growth of Aluminum Oxide on Silver

As mentioned earlier, rapid oxidation occurs when silver films are exposed to oxygen plasma. The rapid oxidation is shown in Figure 4-13. Figure 4-14 demonstrates that thermal ALD of Al_2O_3 on silver does not oxidize the underlying silver substrate. One can notice that the growth rate does not stabilize until the thickness passes about 15 \AA , which could be an indication of substrate-inhibited growth. An additional experiment utilized a 0.5 nm thermal Al_2O_3 interface layer to protect the underlying silver surface from oxygen plasma exposure. In this case, the *in-situ* ellipsometry results showed that oxidation of the silver layer was markedly reduced during PEALD Al_2O_3 , as indicated in Figure 4-15.

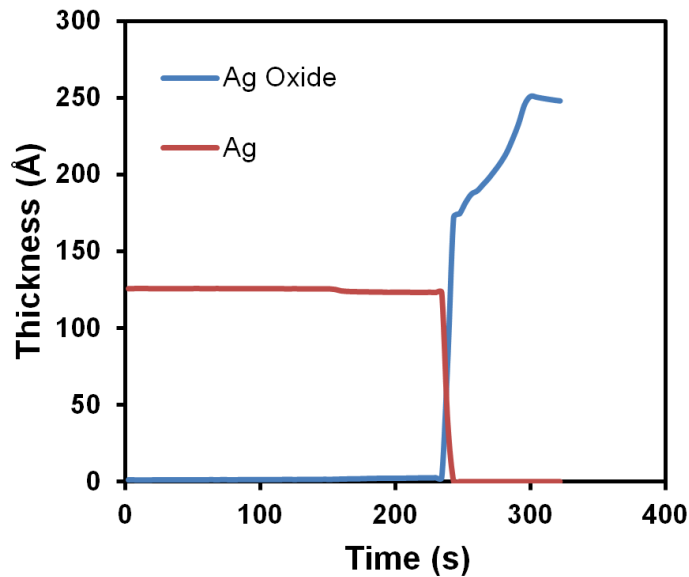


Figure 4-13 Oxidation of silver layer during oxygen plasma exposure at 100°C .

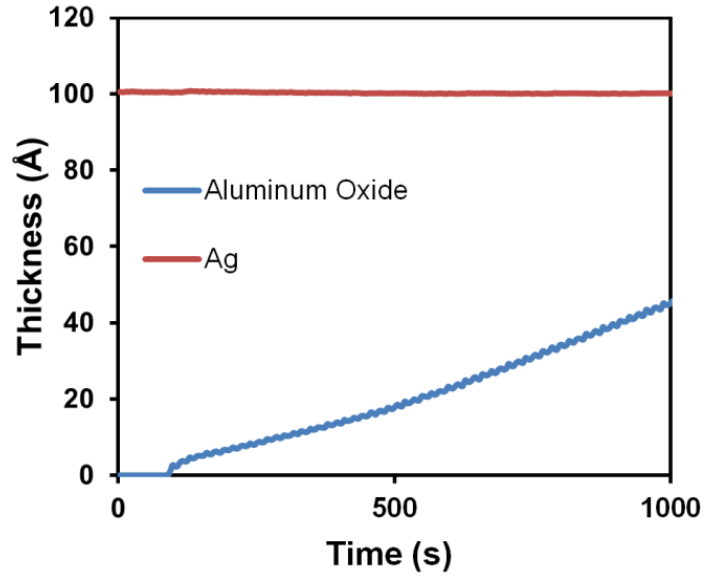


Figure 4-14 Thermal Al₂O₃ ALD on silver at 100°C.

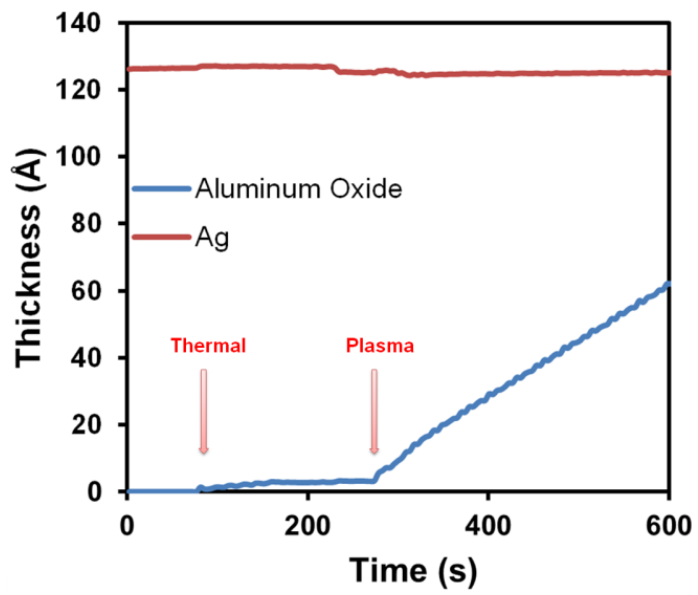


Figure 4-15 PEALD Al₂O₃ on 0.5 nm thermal Al₂O₃ interface layer on silver at 100°C.

4.3.5 Non-Linear Growth in Thermal ALD

It was shown that the thermal ALD of Al_2O_3 on a Cr surface at 100°C resulted in linear growth (Figure 4-9). However, the conditions changed when the substrate temperature was increased to 200°C and 300°C . Both *in-situ* and *ex-situ* spectroscopic ellipsometry measurements showed that thermal ALD of metal oxides on metal substrates may initially have substrate-prohibited growth. Figure 4-16 shows the growth of HfO_2 and ZrO_2 on Si and Cr substrates at a deposition temperature of 200°C . The growth of HfO_2 and ZrO_2 on Si is identified as linear ALD growth. However, the growth on Cr was not ideal linear ALD film growth. Instead, it took about 30 to 40 ALD cycles for the growth rate to stabilize. The growth curve can be divided into three stages. In the first stage which lasts only a few ALD cycles, the growth rate was relatively high. It was followed by the second stage where the growth rate decreased. During the third stage, linear growth was observed. The same experiment done for deposition of Al_2O_3 on Cr revealed a similar result as presented in Figure 4-17.

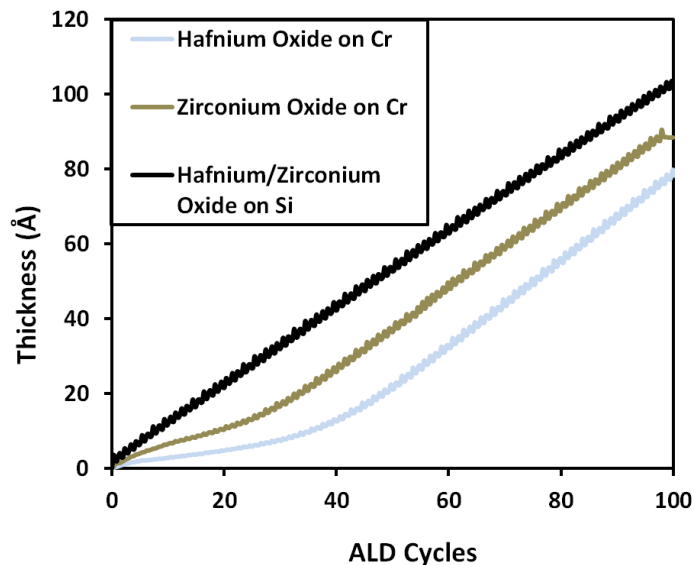


Figure 4-16 Growth of thermal ALD HfO_2 and ZrO_2 on Cr and Si substrates. Unlike deposition on Si, the growth on Cr is initially slower, but gradually increases until it stabilizes.

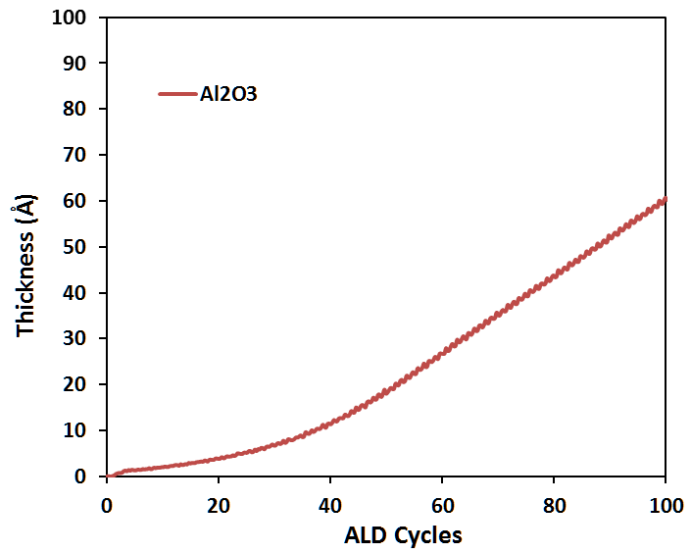


Figure 4-17 Thermal ALD of Al₂O₃ on Cr substrate at a deposition temperature of 200°C.

Initially, it was believed that the non-linear growth was due to using improper settings during the ellipsometry measurements. Further extensive experiments revealed that the observation must be real. In order to understand what might have caused this effect, several other experiments were performed in which the process parameters were changed. Among the parameters, H₂O pulse duration had a significant effect on the growth behavior of these metal oxides on Cr substrates. Figure 4-18 demonstrates the effect of water pulse duration on the growth characteristics of Al₂O₃ on Cr at a deposition temperature of 300°C. Thermal ALD of Al₂O₃ on Si using a water pulse of 0.5 s had a linear growth curve, while the growth on Cr showed a non-linear growth. When the H₂O pulse was increased to 1.0 s, the growth rate increased and the initial non-linear stage was reduced. Increasing the H₂O pulse to 1.5 s completely eliminated the non-linear stage so that growth was very similar to the growth on a silicon substrate.

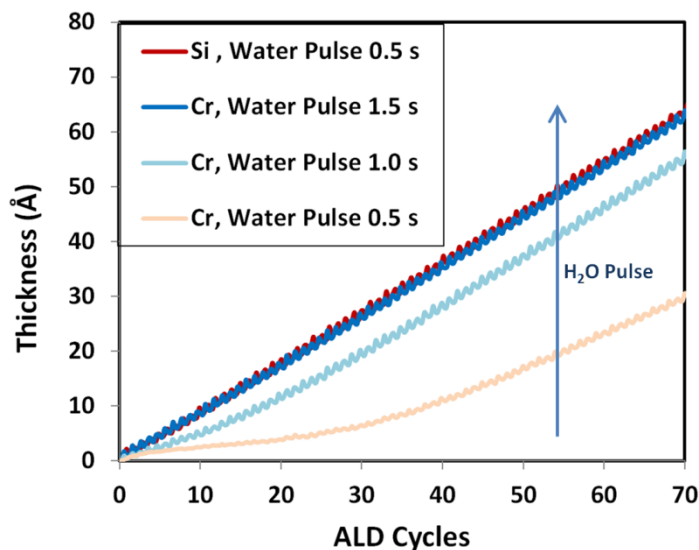


Figure 4-18 Effect of water pulse duration on the growth of Al_2O_3 on Cr at a deposition temperature of 300°C .

This experiment proved that the possible nucleation or delayed growth was in some way linked to the surface reactions involving water. The exact explanation is not available at this point; however, it is proposed that this phenomenon is caused by desorption of water from the surface and low surface density of hydroxyl groups at the beginning of the deposition. It is already known that the growth per cycle during ALD of metal oxides is directly related to the surface density of hydroxyl groups [29-33]. The fact that this effect was only occurring at deposition temperatures above 100°C indicated that temperature had a major role. Experiments have shown that the density of hydroxyl groups decreases as the substrate temperature increases through the process of dehydroxylation [34-36], which is an activated process; increasing the temperature results in an increase in the desorption rate. Since non-linear growth is not observed for deposition on silicon substrates, it is thought that the metal surface enhances the dehydroxylation process. Increasing the H_2O pulse can override the effect of dehydroxylation by providing a higher flux of water molecules toward the surface. When a small water dose (0.5 s) was used, the generation rate of hydroxyl groups on the surface was not high enough to achieve saturation. Therefore, the

growth rate was smaller than normal. As film growth continued, the generation rate of -OH groups increased after each ALD cycle until it reached a constant rate. After this point, the effect of substrate was minimal and linear growth was observed. Similar results have been reported for ALD of metal oxides on H-terminated silicon substrates [31, 37, 38]. The experiments showed that the deposition of oxides on H-terminated silicon involved nucleation and delayed growth [39, 40]. Therefore, it is thought that the metal surface limits the adsorption of water necessary for formation of dense nucleation sites. However, more experiments using *in-situ* analytical tools such as FTIR must be performed to prove this explanation. Additionally, more complicated optical models can be developed to study the nucleation period. One of limitations of the current model was that the layers were assumed to be flat. When such model is used to determine the thickness of a discontinuous film, such as growing nuclei on a surface, the thickness measurement may not be very accurate before a continuous film forms.

It is also important to note that the growth rate in the linear part of the deposition with short 0.5 s water pulses was noticeably lower than the growth rate of the deposition with long pulses. Based on ideal ALD characteristics, it was expected to observe the same growth rate once the initial non-linear part ended. However, the growth rate was found to be lower. This observation implied that long water pulses were required to achieve surface saturation and maximum growth rate during thermal ALD, during both non-linear and linear growth. A possible cause could be insufficient mass transport inside the ALD chamber. Since the sample was placed at the center of the sample holder and the carrier gas mixed with reactants was flowing from the top, a stagnation point formed near the center of the sample, which affected the transport of the reactants to the substrate surface. The surface roughness of Cr metal possibly made this effect more prominent, which can explain the difference between the growth on Si and Cr.

The initial high growth rate observed at the very first few cycles was possibly caused by the adsorption of metalorganic precursor molecules. It is thought that

the precursor molecules are physisorbed on defects on the metal surface after the first pulse, as seen by a jump in the film thickness ($\sim 1 - 2 \text{ \AA}$). Figure 4-19 shows a close-up view of the initial cycles during ALD of aluminum oxide on Cr (from Figure 4-17). The adsorption of TMA molecules on the surface can be identified as a sudden increase in the film thickness after the first cycle. However, these physisorbed molecules do not participate in reactions with the H_2O molecules. With each water pulse, the surface density of hydroxyl groups increased and as a result, more precursor molecules were involved in reactions, generating more $-\text{OH}$ groups. The process continued until there was enough $-\text{OH}$ groups on the surface to reach saturation.

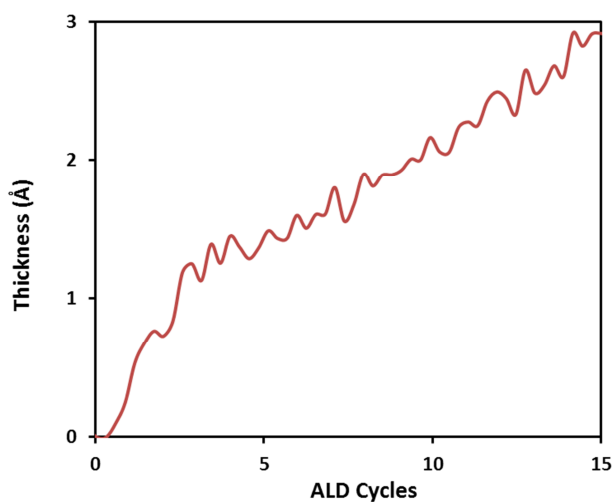


Figure 4-19 The first few cycles during thermal ALD of Al_2O_3 on Cr substrate at a deposition temperature of 200°C . The adsorption of TMA on the surface is identified as a jump in thickness after the first cycle.

Plan-view TEM imaging was used to search for the nucleation sites formed during the second stage. The images were taken using a JEOL 2010 microscope operating at 200 kV accelerating voltage. In order to simplify the sample preparation process, Cr metal was sputter deposited on a TEM nickel grid to form a 20-nm metal layer on top of the thin carbon film. The grid was transferred into ALD chamber and was used as a substrate to deposit Al_2O_3 by thermal ALD.

Figure 4-20 shows the TEM images at three different magnifications showing the surface of the Cr metal covered with Al_2O_3 . Energy dispersive spectroscopy (EDS) measurements confirmed the presence of aluminum and oxygen on the surface. However, the images only showed Cr grains. Diffraction patterns were all related to the Cr BCC structure with a lattice parameter of 2.88 \AA . It was concluded that the very thin Al_2O_3 did not have enough contrast to be detected in this configuration. Cross-section imaging might be a more suitable approach.

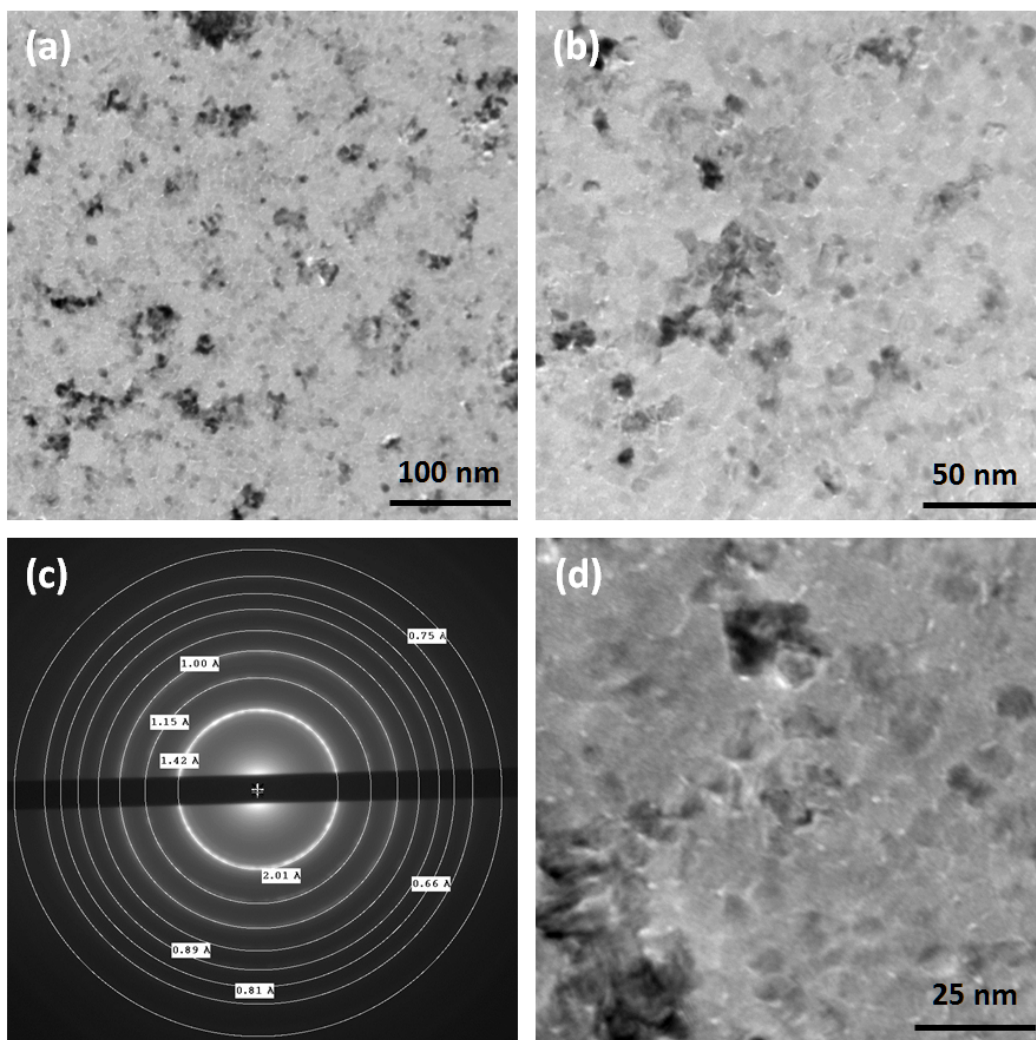


Figure 4-20 Top-view TEM images of thin Al_2O_3 on Cr at various magnifications.

4.3.6 FTIR Analysis

FTIR measurements were performed on 5-nm ALD Al_2O_3 films deposited on 100-nm Cr films to support the observed data from *in-situ* SE measurements, which suggested an interfacial oxide layer formed during PEALD. Four samples were prepared under different conditions:

- (i) *Thermal ALD – Exposed to Air*: Cr film exposed to air for two hours prior to deposition of Al_2O_3 by thermal ALD
- (ii) *Plasma ALD*: An as-grown Cr film was transferred to ALD chamber under vacuum followed by PEALD of Al_2O_3
- (iii) *Thermal ALD / Plasma ALD*: An as-grown Cr film was transferred to ALD chamber under vacuum followed by deposition of 0.5 nm Al_2O_3 by thermal ALD and 4.5 nm Al_2O_3 by PEALD
- (iv) *Thermal ALD*: An as-grown Cr film was transferred to ALD chamber under vacuum followed by thermal ALD of Al_2O_3

The FTIR spectra obtained from the samples are presented in Figure 4-21. The FTIR spectrum from a Cr film without any Al_2O_3 film is also presented as a reference. Sample number (i) had a very similar spectrum to the Cr sample. The only difference was the broad peak between 750 and 950 cm^{-1} [41] due to the Al_2O_3 layer (Al-O stretching) which was absent in the Cr spectrum. Samples (iii) and (iv) also showed similar spectra. The spectra for these samples showed less absorbance in the range of 500 to 2500 cm^{-1} relative to the sample (i). Both sample (i) and (iv) were prepared by depositing 5 nm of Al_2O_3 on Cr surface by thermal ALD. The only difference was that the sample (i) had been exposed to air prior to Al_2O_3 deposition while the other had been transferred under vacuum. The SE analysis showed that the sample (iv) did not have the Cr_2O_3 layer however the sample (i) had a native Cr_2O_3 layer with a thickness of about 2-3 nm due to exposure to air. Therefore, the difference in the shape of the FTIR spectrum is caused by the presence of the chromium oxide layer which changes the metal/ALD oxide interface. The spectrum of sample (ii) which had a 5-nm Al_2O_3

deposited by PEALD was between samples (i) and (iv), which is consistent with the SE data which showed that it has a 1.4-nm chromium oxide layer. To better distinguish the differences in the FTIR spectra of these samples, their corresponding curves were subtracted from the curve of Cr sample and an offset was added to match the Al-O stretching peak. The results are shown in Figure 4-22. As mentioned earlier, the shape of the curves underwent significant changes as a result of change in the interface. It is suggested that the presence and thickness of the interfacial chromium oxide layer cause the spectrum to shift up or down.

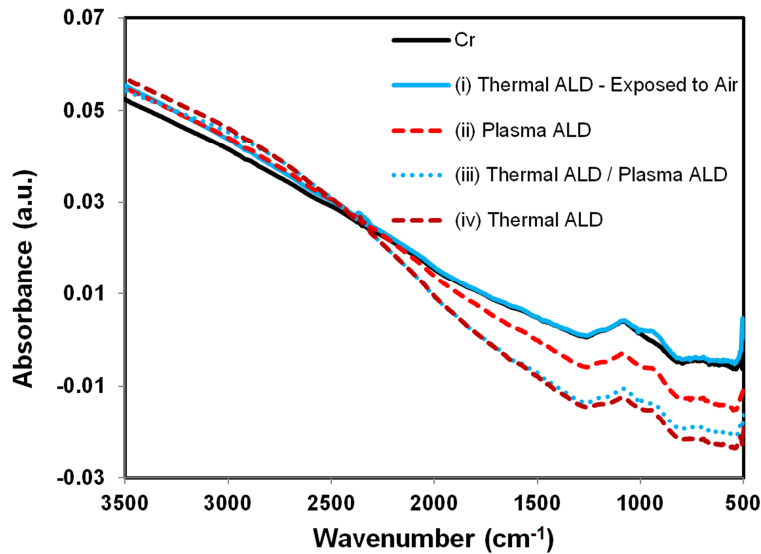


Figure 4-21 FTIR spectra of thin aluminum oxide on Cr films with different Cr/Al₂O₃ interfaces.

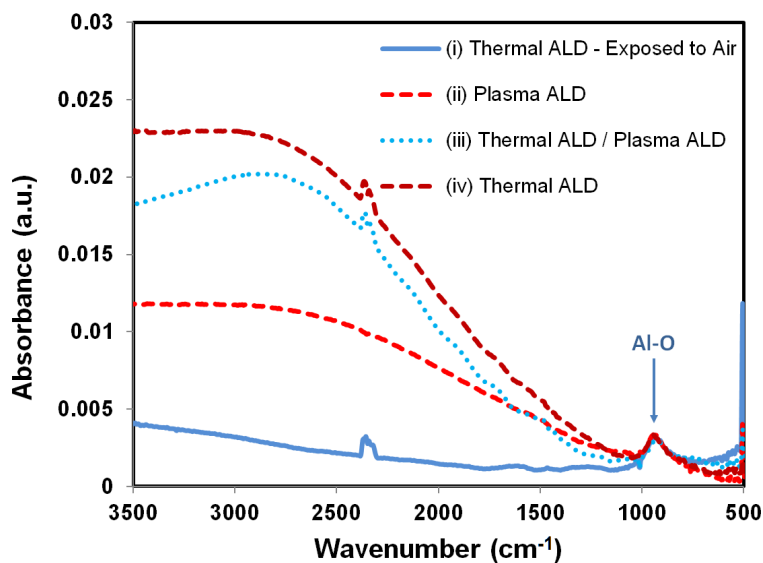


Figure 4-22 FTIR spectra of thin aluminum oxide on Cr films with different Cr/Al₂O₃ interfaces subtracted from the Cr spectrum.

4.4 Conclusions

The deposition of thin metal oxide films using thermal and plasma enhanced atomic layer deposition on metallic surfaces was studied using *in-situ* spectroscopic ellipsometry. The results indicated that a thin layer of metal oxide was formed during the initial stages of PEALD film growth. The thickness of this interfacial oxide layer depended on the deposition parameters such as temperature and also the order of introducing the reactants into the reaction chamber. The results also showed that covering the metal surface with a very thin layer of thermal ALD Al₂O₃ could effectively protect the metal surface from oxidation during the PEALD process. Thermal ALD of oxides did not involve noticeable oxidation of the substrate metal; however, non-linear growth was observed for the depositions at higher temperatures for short water pulses. The substrate-inhibited growth was possibly caused by the water desorption and the lack of –OH groups on the surface. Increasing the water pulse during each ALD cycle resulted in linear growth. FTIR analysis showed that the IR spectra for Cr/Al₂O₃ films were affected by the presence and thickness of the interfacial layer.

4.5 References

- [1] M.D. Groner, J.W. Elam, F.H. Fabreguette, S.M. George, *Thin Solid Films* 413/1-2 (2002) 186.
- [2] F. Zaera, *J Mater Chem* 18/30 (2008) 3521.
- [3] H. Kim, H.-B.-R. Lee, W.J. Maeng, *Thin Solid Films* 517/8 (2009) 2563.
- [4] C.O. Chui, S. Ramanathan, B.B. Triplett, P.C. McIntyre, K.C. Saraswat, *IEEE Electr Device L* 23/8 (2002) 473.
- [5] D. Shahrjerdi, E. Tutuc, S.K. Banerjee, *Appl Phys Lett* 91/6 (2007).
- [6] A. Chin, B.C. Lin, W.J. Chen, Y.B. Lin, C. Thai, *IEEE Electr Device L* 19/11 (1998) 426.
- [7] S.E. Potts, W. Keuning, E. Langereis, G. Dingemans, M.C.M. van de Sanden, W.M.M. Kessels, *Journal of The Electrochemical Society* 157/7 (2010) P66.
- [8] S.M. George, *Chem Rev* 110/1 (2010) 111.
- [9] T.O. Kääriäinen, D.C. Cameron, *Plasma Processes and Polymers* 6/S1 (2009) S237.
- [10] A. Niskanen, K. Arstila, M. Ritala, M. Leskelä, *Journal of The Electrochemical Society* 152/7 (2005) F90.
- [11] H. Kim, *Thin Solid Films* 519/20 (2011) 6639.
- [12] E.W. Cowell, N. Alimardani, C.C. Knutson, J.F. Conley, D.A. Keszler, B.J. Gibbons, J.F. Wager, *Adv Mater* 23/1 (2011) 74.
- [13] H. Fujiwara, *Spectroscopic Ellipsometry: Principles and Applications*, Wiley, 2007.
- [14] E. Langereis, S.B.S. Heil, H.C.M. Knoop, W. Keuning, M.C.M. van de Sanden, W.M.M. Kessels, *J Phys D Appl Phys* 42/7 (2009).
- [15] E. Langereis, S.B.S. Heil, M.C.M. van de Sanden, W.M.M. Kessels, *Journal of Applied Physics* 100/2 (2006).
- [16] D. Schmidt, S. Strehle, M. Albert, W. Hentsch, J.W. Bartha, *Microelectron Eng* 85/3 (2008) 527.

- [17] H.C.M. Knoop, A.J.M. Mackus, M.E. Donders, M.C.M. van de Sanden, P.H.L. Notten, W.M.M. Kessels, *Electrochem Solid St* 12/7 (2009) G34.
- [18] H.G. Tompkins, T. Zhu, E. Chen, *J Vac Sci Technol A* 16/3 (1998) 1297.
- [19] S.K. Kim, S.W. Lee, C.S. Hwang, Y.S. Min, J.Y. Won, J. Jeong, *Journal of The Electrochemical Society* 153/5 (2006) F69.
- [20] T. Saburi, T. Suzuki, K. Kiuchi, Y. Fujii, *Thin Solid Films* 506-507 (2006) 331.
- [21] F. A.T, Jr., *Thin Solid Films* 95/4 (1982) 297.
- [22] A. Derooij, *Esa Journal-European Space Agency* 13/4 (1989) 363.
- [23] L. Sun, K.W. Noh, J.-G. Wen, S.J. Dillon, *Langmuir* 27/23 (2011) 14201.
- [24] D.B. Oakes, R.H. Krech, B.L. Upschulte, G.E. Caledonia, *Journal of Applied Physics* 77/5 (1995) 2166.
- [25] A.T. Fromhold, *Theory of Metal Oxidation*, North-Holland Publishing Company, Amsterdam, 1976.
- [26] Y. Song, S. Dhar, L.C. Feldman, G. Chung, J.R. Williams, *Journal of Applied Physics* 95/9 (2004) 4953.
- [27] R. Ghez, *The Journal of Chemical Physics* 58/5 (1973) 1838.
- [28] A.N. Rider, R.N. Lamb, M.H. Koch, *Surf Interface Anal* 31/4 (2001) 302.
- [29] S.M. George, A.W. Ott, J.W. Klaus, *J Phys Chem-US* 100/31 (1996) 13121.
- [30] M. Ritala, T. Asikainen, H. Leskela, *Electrochem Solid St* 1/3 (1998) 156.
- [31] M.A. Alam, M.L. Green, *Journal of Applied Physics* 94/5 (2003) 3403.
- [32] R. Matero, A. Rahtu, M. Ritala, M. Leskelä, T. Sajavaara, *Thin Solid Films* 368/1 (2000) 1.
- [33] L.G. Gosset, J.F. Damlencourt, O. Renault, D. Rouchon, P. Holliger, A. Ermolieff, I. Trimaille, J.J. Ganem, F. Martin, M.N. Semeria, *J Non-Cryst Solids* 303/1 (2002) 17.

- [34] H.B. Profijt, S.E. Potts, M.C.M. van de Sanden, W.M.M. Kessels, *Journal of Vacuum Science & Technology A* 29/5 (2011).
- [35] M. Deminsky, *Surface Science* 549/1 (2004) 67.
- [36] M. Juppo, A. Rahtu, M. Ritala, M. Leskelä, *Langmuir* 16/8 (2000) 4034.
- [37] J.C. Hackley, T. Gougousi, J.D. Demaree, *Journal of Applied Physics* 102/3 (2007).
- [38] R.L. Puurunen, W. Vandervorst, W.F.A. Besling, O. Richard, H. Bender, T. Conard, C. Zhao, A. Delabie, M. Caymax, S. De Gendt, M. Heyns, M.M. Viitanen, M. de Ridder, H.H. Brongersma, Y. Tamminga, T. Dao, T. de Win, M. Verheijen, M. Kaiser, M. Tuominen, *Journal of Applied Physics* 96/9 (2004) 4878.
- [39] R.L. Puurunen, W. Vandervorst, W.F.A. Besling, O. Richard, H. Bender, T. Conard, C. Zhao, A. Delabie, M. Caymax, S. De Gendt, M. Heyns, M.M. Viitanen, M. de Ridder, H.H. Brongersma, Y. Tamminga, T. Dao, T. de Win, M. Verheijen, M. Kaiser, M. Tuominen, *Journal of Applied Physics* 96/9 (2004) 4878.
- [40] J. Kim, T.W. Kim, *JOM* 61/6 (2009) 17.
- [41] D. N. Goldstein, J. A. McCormick, S. M. George, *Journal of Physical Chemistry C* 112 (2008) 19530.

Chapter 5 ALD for Fabrication of Metal-Insulator-Metal Diodes *

5.1 Introduction

Metal-insulator-metal (MIM) diodes are rectifying electron devices formed by positioning a thin insulating layer between two metallic electrodes. Electrons tunnel through the oxide in the presence of a potential difference between the electrodes [1, 2]. MIM devices are currently the center of attention for the development of next generation antenna-coupled infrared detectors [3-5], high frequency mixers [6], and optical rectennas [7]. The main advantage of MIM diodes over semiconductor rectifiers is superior response and broader bandwidth. MIM diodes have been fabricated using various techniques such as, thermal oxidation [8-10], plasma oxidation [3, 5] and anodic oxidation [11] of metallic surfaces. Recently Cowell *et al.* [12] demonstrated the application of atomic layer deposition (ALD) to grow metal oxides between metallic electrodes.

* A version of this chapter has been submitted to Journal of The Electrochemical Society.

ALD is a thin film deposition technique based on alternating surface reactions of the individual precursors leading to the controlled layer by layer growth of thin films [13, 14]. ALD film growth takes place through repetition of ALD cycles. Each cycle begins with introduction of the first precursor into the reaction chamber followed by carrier gas purge to remove excess reactant and chemical by products. Then the second precursor is pulsed into the chamber followed by a carrier gas purge. The key distinctive feature of ALD is its self-limiting growth behavior which means the film thickness is simply controlled by counting the number of ALD cycles (growth per cycle or GPC) [15, 16]. This feature brings several benefits including excellent film uniformity over large areas, low temperature growth and accurate thickness control at the atomic scale [17, 18]. There are two modes of operation for ALD: thermal and plasma-enhanced. In thermal ALD (TALD), the energy required for reactions is provided solely by heating the substrate surface whereas in plasma-enhanced ALD (PEALD) a remote plasma is used as an additional source of energy to generate highly reactive radicals to accelerate the surface reactions. The main advantage of PEALD is its ability to deposit films at much lower temperatures even at room temperature [19].

Fabrication of MIM diodes featuring multiple insulating layers is possible using ALD. Successful fabrication of MIM diodes requires selection of suitable materials and appropriate deposition conditions. Here, MIM diodes with the following structures were fabricated: Cr/Al₂O₃/Cr and Cr/HfO₂/Cr. Chromium metal was selected due to its good electrical conductivity and relatively smooth sputtered surface. Aluminum oxide and hafnium oxide are high-k materials with high break down electric fields and have been successfully deposited using ALD.

In this chapter findings on the application of thermal and plasma-enhanced ALD for deposition of metal oxides used in fabrication of MIM diodes are presented. Since deposition of a thin insulator on a metal surface is a major step in fabrication of MIM diodes, deposition characteristics of aluminum and hafnium oxide as an insulator on chromium electrodes is examined in this chapter.

Electrical measurements including capacitance-voltage (CV) and current-voltage (IV) were also performed to study the electrical properties of the fabricated MIM diodes.

5.2 Experimental Procedure

The structure of MIM diodes is shown schematically in Figure 5-1. The chromium metal film as the bottom electrode was deposited by DC magnetron sputtering on a thermally oxidized Si (100) substrate. This was followed by the deposition of an insulating oxide using ALD. Finally, the top chromium electrode, in the form of circular dots, was sputter deposited on the ALD oxide layer using a shadow mask. ALD films were also grown on bare Si (100) wafers for comparison.

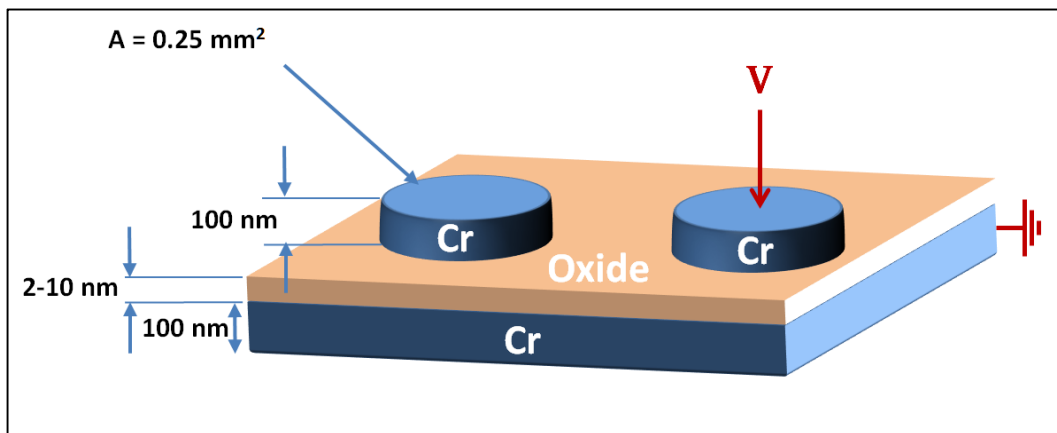


Figure 5-1 Schematic structure of MIM diodes. The two metallic electrodes are separated by a thin insulating layer. The electrical measurements are performed by applying a potential across the insulating layer.

The depositions were carried out in an integrated ALD research system from Kurt J. Lesker that incorporated an ALD reactor with dual thermal and remote plasma capability, as well as *in-situ* spectroscopic ellipsometry. The ALD reactor was connected, through vacuum transfer via a load-lock, with a sputtering chamber as shown schematically in Figure 5-2. The sputtering chamber had a base pressure of $<1.3 \times 10^{-5}$ Pa.

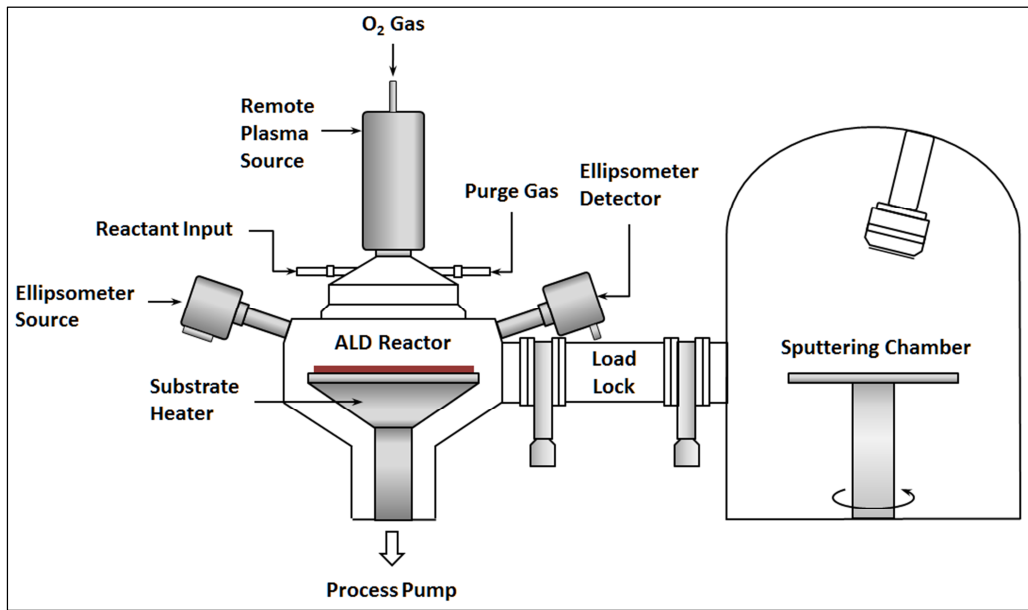


Figure 5-2 Schematic layout of the ALD research system.

The metal depositions were carried out with an argon pressure of 0.23 Pa and at constant power of 300 W. The operating conditions were chosen based on studies on Cr sputtering reported elsewhere [20] to obtain metallic films with the lowest residual oxygen and therefore lowest resistivity. The thickness of both the bottom and top Cr electrodes was chosen to be 100 nm. Each of the top electrodes had an area of 0.25 mm². The ALD system was loaded with tetrakis(dimethylamino)hafnium, TDMAH, and trimethylaluminium, TMA, precursors that were used along with water (TALD) or oxygen plasma (PEALD)

to deposit hafnium and aluminum oxide. The water precursor was 18 M Ω deionized water, and the oxygen for PEALD was 99.999% pure. High purity argon (99.999%) was used as the purge gas. Each thermal cycle included a short dose (20-40 ms) of the metallo-organic precursor (TDMAH or TMA) followed by 5 s purge and a water pulse (0.5 s) followed by a 10 s purge. The first half of the PEALD cycle was the same as for thermal ALD; however, in the second half, instead of using water the chamber was exposed to 1 s of remote oxygen plasma followed by 2 s of argon purge. The oxides deposited by ALD had a nominal thickness of 1.5-6.5 nm. The oxide film thickness was measured *in-situ*, using a J. A. Woollam M-2000DI ellipsometer with a wide spectral range of 197-1700 nm and fast acquisition speed of 20 dispersions per second. This was ideal for real-time monitoring of film thickness and any change in properties of film-substrate interface.

To determine the surface composition of the films, XPS analysis was performed using a Kratos Analytical AXIS-165 spectrometer at the Alberta Centre for Surface Engineering and Science (ACSES). The base pressure in the analytical chamber was lower than 3×10^{-8} Pa. A monochromatic Al K α ($h\nu = 1486.6$ eV) source was used at a power of 210 W. Survey spectra were collected for binding energies ranging from 1100 to 0 eV with a pass energy (PE) of 160 eV and a step of 0.35 eV. High-resolution spectra were measured with a PE of 20 eV and a step of 0.1 eV. To remove surface contamination, samples were sputter etched using argon ions for 2 min.

Electrical measurements were also carried out in order to evaluate the properties of fabricated MIM diodes. I-V and capacitance measurements were performed using a Keithley 2400 source meter and a Keithley 595 quasistatic CV meter, respectively. The measured capacitance was corrected to include effects of leakage current.

5.3 Results and Discussion

5.3.1 Deposition and Film Properties

One key consideration in the fabrication process of MIM structures is the growth of the insulating material with a desired thickness. Since the insulator layer needs to be very thin (2-5 nm range) to increase the tunneling probability, precise thickness measurement is essential. Although linear film growth (thickness versus the number of ALD cycles) is attributed to ALD, the first stages of film growth may involve nucleation, substrate-enhanced growth or interfacial changes. To study the ALD growth of aluminum and hafnium oxide films on chromium surfaces and the effect of ALD mode (thermal and plasma enhanced), the change in film thickness after each ALD cycle was measured by *in-situ* ellipsometry. The results presented in Figure 5-3 show the growth characteristics of Al₂O₃ and HfO₂ on Cr surfaces at 100°C. Thermal ALD of Al₂O₃ on Cr (Figure 5-3a) showed linear growth with a slope (growth per cycle, GPC) of ~0.85 Å/cycle that is very close to the GPC of Al₂O₃ on Si substrates. Thermal ALD of HfO₂ on Cr surface (Figure 5-3b) also showed linear growth with a slope of ~1.35 Å/cycle. However, the growth rate was slightly lower during the first few cycles (<10). This observation suggested that the thermal ALD growth of HfO₂ on Cr was affected by the Cr substrate. This type of ALD growth is referred to as substrate-inhibited growth [16]. At the deposition temperature of 300°C, the effect of substrate on the thermal ALD growth was more dominant causing growth delays for both Al₂O₃ and HfO₂.

The PEALD deposition (Figure 5-3c, d) on Cr involved oxidation of the Cr surface due to exposure to oxygen plasma during the first few ALD cycles. As a result, the growth rate appeared to be higher initially (Cr₂O₃ thickness was added to ALD oxide thickness). Once the deposited oxide thickness was large enough to prevent the oxygen reaching the underlying Cr layer, the oxidation stopped and linear ALD growth was observed. The inset graph in Figure 5-3c depicts a more

detailed view of the initial ALD cycles that led to the oxidation of Cr surface. The first half-cycle covered the surface with adsorbed TMA molecules. Once the plasma pulse was ignited during the second half-cycle (indicated by the vertical arrow), in addition to the growth of Al_2O_3 , a thin chromium layer was also formed. This caused the GPC to be higher than expected. As the deposition continued, the ALD oxide layer grew thicker and the amount of chromium oxide formed during each cycle decreased rapidly until it stopped completely after 5 cycles. The dashed lines in Figure 5-3 c and Figure 5-3d represent the linear growth observed in ALD of the corresponding oxide on a Si substrate. Therefore, the offset between the measured thickness and the dashed line is a representation of the magnitude of the interfacial chromium oxide layer.

The results presented in the previous chapter showed that the thickness of the interfacial chromium oxide layer formed during PEALD of Al_2O_3 on Cr was in the range of 1.4 - 2.5 nm, depending on the ALD conditions. The deposition at 300°C also had similar characteristics to 100°C. The main difference was the interfacial oxide that was slightly thicker at 300°C. A comparison between the growth curves for Al_2O_3 and HfO_2 indicated that a thicker interfacial chromium oxide formed during the PEALD of HfO_2 . This suggested that on the nano-scale, aluminum oxide was a better plasma oxygen diffusion barrier than hafnium oxide.

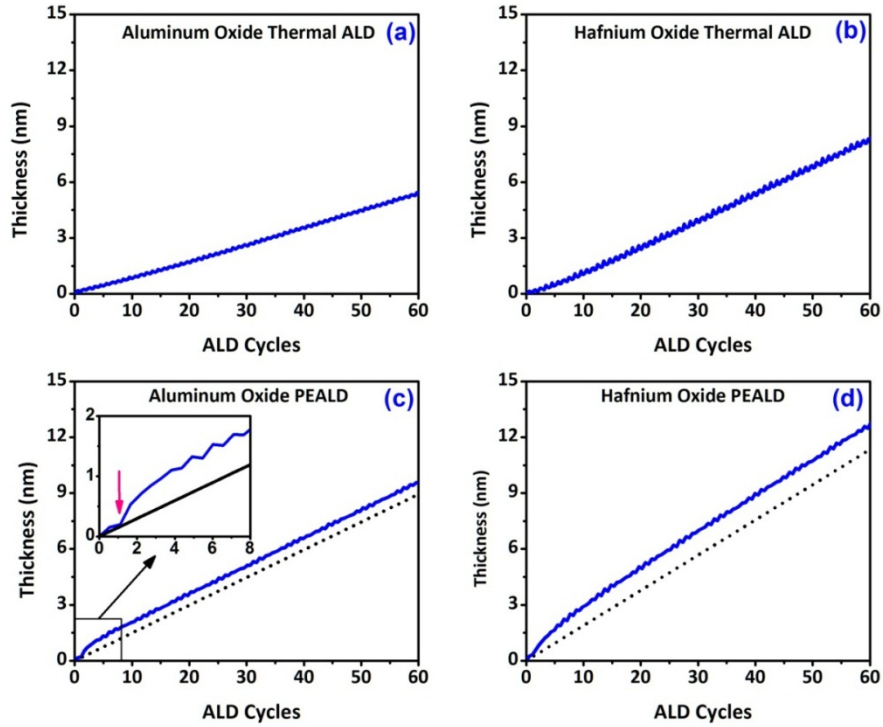


Figure 5-3 Growth of Al_2O_3 and HfO_2 thin films on Cr substrate as measured by *in-situ* ellipsometry; (a) Thermal ALD of Al_2O_3 ; (b) Plasma ALD of Al_2O_3 ; (c) Thermal ALD of HfO_2 ; (d) Plasma ALD of HfO_2 . All the depositions were at 100°C . The dashed lines indicate ideal growth.

The chemical composition of thin (10 nm) Al_2O_3 and HfO_2 films calculated from XPS quantitative analysis is presented in Table 5-1 and Table 5-2, respectively. All the films contained carbon as an impurity that was due to organometallic nature of the precursors. Hafnium oxide films contained more carbon than aluminum oxide films since the precursor used for deposition of HfO_2 (TDMAH) had a higher carbon content than the TMA. There are eight carbon atoms for every metal atom in the TDMAH molecule whereas for TMA, the carbon/metal ratio is only three. This increased the chance of carbon incorporation into the HfO_2 films.

Table 5-1 Chemical composition of Al₂O₃ ALD films

| Oxide | ALD Type | Deposition Temperature (°C) | Al at. % | O at. % | C at. % | O/M ratio |
|--------------------------------|----------|-----------------------------|----------|---------|---------|-----------|
| Al ₂ O ₃ | TALD | 100 | 36.7 | 60.5 | 2.8 | 1.65 |
| Al ₂ O ₃ | PEALD | 100 | 36.8 | 61.2 | 2.0 | 1.66 |
| Al ₂ O ₃ | TALD | 300 | 38.3 | 59.6 | 2.1 | 1.56 |
| Al ₂ O ₃ | PEALD | 300 | 38.5 | 60.0 | 1.5 | 1.56 |

Table 5-2 Chemical composition of HfO₂ ALD films

| Oxide | ALD Type | Deposition Temperature (°C) | Hf at. % | O at. % | C at. % | O/M ratio |
|------------------|----------|-----------------------------|----------|---------|---------|-----------|
| HfO ₂ | TALD | 100 | 30.5 | 64.7 | 4.8 | 2.12 |
| HfO ₂ | PEALD | 100 | 28.6 | 66.4 | 4.9 | 2.32 |
| HfO ₂ | TALD | 300 | 31.2 | 65.3 | 3.5 | 2.09 |
| HfO ₂ | PEALD | 300 | 31.5 | 65.5 | 3.0 | 2.07 |

For Al₂O₃ films, PEALD produced films with less carbon content compared to thermal ALD. However for HfO₂ films, carbon content did not depend on the type of ALD process. The oxygen to metal ratio was higher than the oxide stoichiometry of 1.5 for Al₂O₃ and 2.0 for HfO₂. The ratio was closer to the stoichiometric value when the deposition temperature was increased from 100°C to 300°C. Additionally, the carbon levels were lower in the films deposited at 300°C, which indicated that denser films were grown at higher deposition temperatures. This observation is in good agreement with previously reported results [21]. The films were also expected to contain some levels of hydrogen, although the XPS results could not be used to confirm this due to insensitivity to light elements.

Figure 5-4 shows XPS spectra for Al 2p, Hf 4f, and C 1s core levels in both thermal ALD and PEALD 10nm-thick Al₂O₃ and HfO₂ films on Si substrates grown at a deposition temperature of 100°C. The peaks were calibrated based on

the C 1s peak at 284.8 eV. As shown in Figure 5-4 a and b, Al 2p and Hf 4f peaks were very similar in both of the thermal and plasma ALD films. However, a small shift toward the lower binding energies was observed in the PEALD films that appeared to be related to the difference in the oxygen/metal ratio in the films (PEALD films being slightly richer in oxygen). The shift was more prominent in the HfO₂ films (~ 0.5 eV) since a relatively larger difference in the oxygen/metal ratio of the thermal ALD and PEALD is observed in the quantitative analysis (Table 5-1). This shift in the binding energy of Hf 4f peaks as a result of change in oxygen/metal ratio was also observed previously by He *et al.* [22].

Since the films contained carbon as impurity, high resolution XPS spectra of C 1s peak are also presented in the Figure 5-4c, d. The characteristic C 1s peak was observed at 284.8 eV and a second unknown peak occurs between 288 and 292 eV. This peak may be due to carbon compounds that contain the O-C=O bond at 289.03 eV. The comparison between thermal ALD and PEALD indicated that the second carbon peak was larger in the PEALD films, which contained more oxygen than the stoichiometric ratio. In addition to hydrogen, some of the excess oxygen in the films is bound to carbon. The O-C=O peak was barely visible in the thermal HfO₂ spectra that had the lowest oxygen/metal ratio. The O-C=O peak was also not detected in any films grown at 300°C.

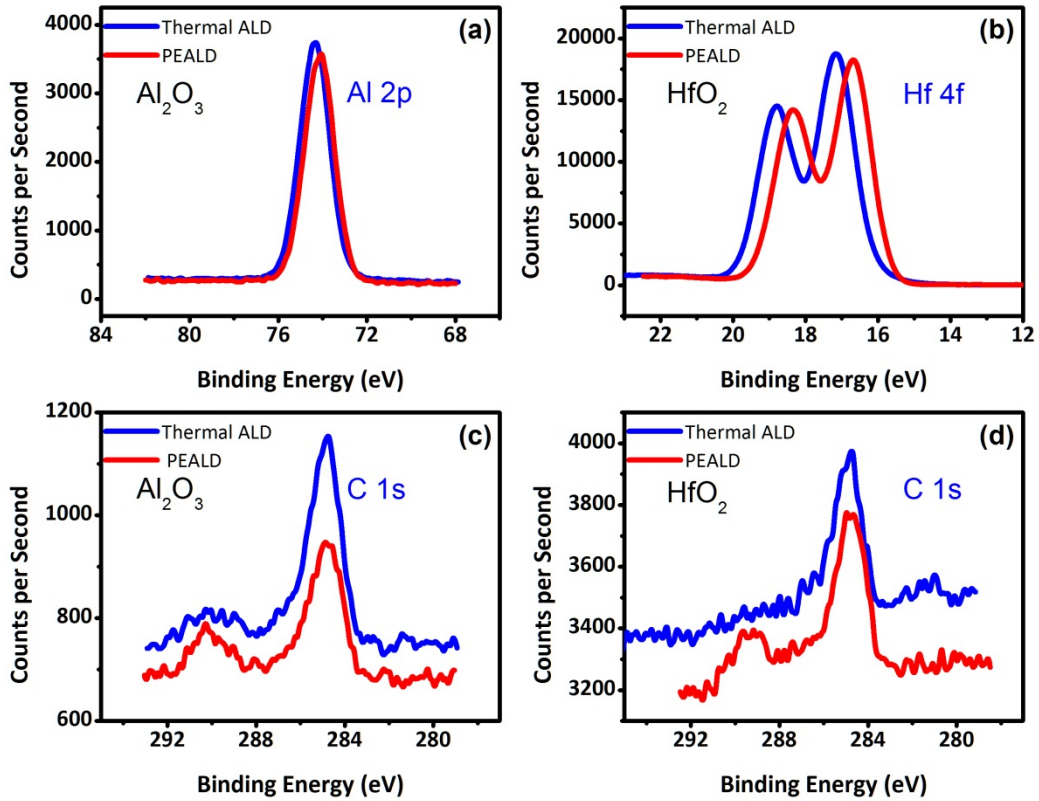


Figure 5-4 XPS spectra of ALD films (10-nm) deposited on Si (100) substrate in thermal and plasma modes at 100°C: (a) Al 2p peak from Al₂O₃; (b) Hf 4f peaks from HfO₂; (c) C 1s peak from Al₂O₃; (d) C 1s peak from HfO₂.

A cross sectional TEM image of an MIM structure is shown in Figure 5-5. The ALD oxide consisted of a 2 nm-thick HfO₂ layer and 2 nm-thick Al₂O₃ layer deposited in PEALD mode. The surface of the bottom Cr metal appeared to be relatively rough with an RMS roughness of ~1.4 nm from AFM measurements. The structure of the Cr layer consisted of columnar grains. The image in the right shows a close up view of one of the grains at the surface of the upper Cr layer covered in a thin layer of native oxide. The upper left image shows the ALD oxide film between the two metal layers. Although the surface of the bottom Cr layer was rough, the interface between the ALD oxide and the upper Cr layer appeared to be relatively smooth. It is expected that the thin ALD film creates the same topography as the original surface since conformal film deposition is a key

attribute of the ALD process. However, in this case the exposure of the metal surface to oxygen plasma is believed to change the surface features making the surface smoother.

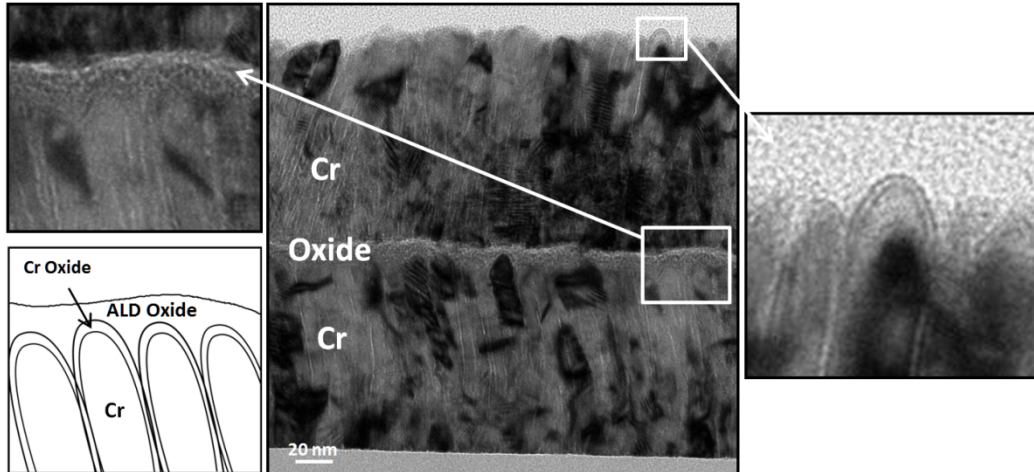


Figure 5-5 Cross sectional TEM image of an MIM (Cr/Cr₂O₃-HfO₂-Al₂O₃/Cr) structure. The bottom-left image schematically shows the structure of the native oxide around the Cr grains and the deposited ALD oxide.

Figure 5-6 shows SEM images of sputtered Cr films before and after exposure to oxygen plasma. As can be seen in the figure, the surface features are affected by the plasma treatment and the surface appears to be not as rough. Therefore the simultaneous growth of chromium oxide caused by plasma oxidation and growth of ALD oxides resulted in the formation of a smoother surface.

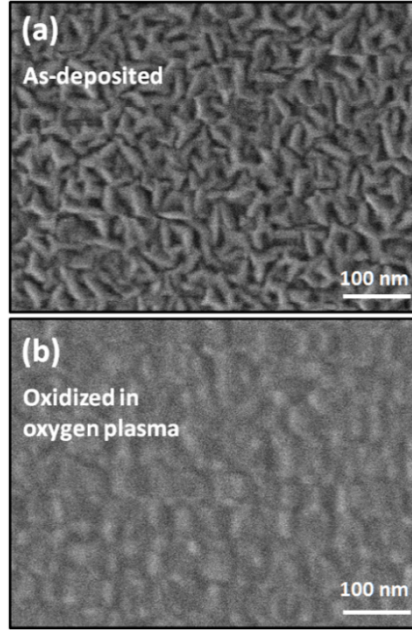


Figure 5-6 Plan-view SEM image of sputtered Cr surface: (a) as-deposited and (b) after being exposed to oxygen plasma. The oxidation process has changed the morphology of the surface.

5.3.2 Capacitance Measurements

The CV plot for Cr/ 4.6 nm Al_2O_3 /Cr diode is shown in Figure 5-7. The capacitance model can be considered as a simple oxide layer between two metallic flat surfaces. Therefore the capacitance does not have a significant dependence on the applied voltage. However, the measured capacitance needs to be corrected by excluding the effect of current leakage on capacitance (here done through CV meter internal software). The comparison between MIM diodes with oxides prepared by thermal ALD and PEALD revealed that the using PEALD resulted in lowered measured capacitance. The ellipsometry data showed that a thin interfacial chromium oxide layer was formed during the ALD film growth. The presence of this interfacial layer lowered the capacitance. The diode with PEALD oxide deposited at 300°C showed a higher C compared to the one deposited at 100°C. The difference was explained by referring to the chemical composition

data which showed that the films deposited at higher substrate temperatures had less impurity. Therefore, the dielectric properties could be improved by increasing the deposition temperature (within the limits of ALD temperature window).

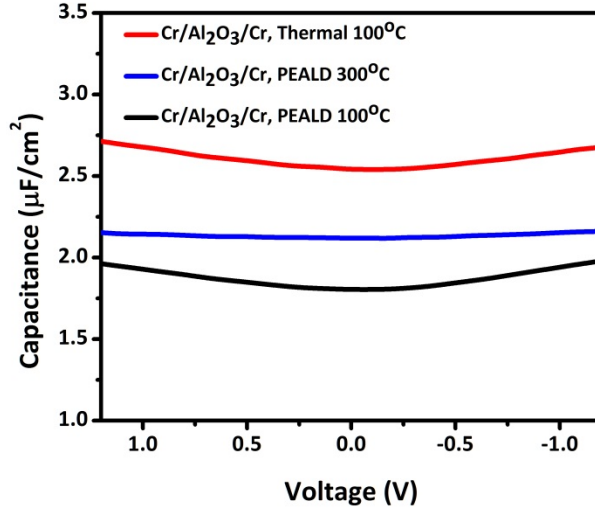


Figure 5-7 CV characteristics of Cr/4.6 nm Al₂O₃/Cr diodes. A lower capacitance was measured for MIM diodes prepared by PEALD due to presence of a thin interfacial chromium oxide.

Figure 5-8 shows the variation of capacitance as a function of insulator thickness for Cr/Al₂O₃/Cr and Cr/HfO₂/Cr MIM diodes. It can be seen that the capacitance decreased with an increase in dielectric film thickness. The dashed lines show the calculated capacitance from $C = \epsilon_0 \epsilon_r \frac{A}{d}$ equation based on the average measured dielectric constant of Al₂O₃ (~8.5) and HfO₂ (~20) ALD films. ϵ_0 is a constant, ϵ_r is the dielectric constant, A is the area and d is the thickness of the dielectric layer. It is clear that the capacitance of MIM diodes was higher than what it should be based on the calculations. One possible explanation for this discrepancy was connected with the surface roughness of the metallic electrodes in MIM diodes. As the TEM images suggested, the real surface area in an MIM diode was slightly larger than the geometric area, A (used in the calculation). As a result, the measured capacitance was higher than the calculated value. The comparison

between the MIM diodes prepared by plasma and thermal ALD revealed that the PEALD resulted in a lower capacitance value. This is explained by the formation of a thin interfacial metal oxide layer between the metal surface and the ALD layer during the plasma ALD process as discussed previously. Interestingly, the difference between the capacitance of MIM diodes prepared by plasma and thermal ALD was larger for hafnium oxide diodes compared to aluminum oxide diodes. As shown in Figure 5-3, a thicker native oxide was formed during PEALD of hafnium oxide and therefore the MIM diodes made by PEALD showed a larger decrease in capacitance with respect to the MIM diodes made by thermal ALD. The difference between the calculated and measured C was relatively small for 10-nm diodes. One possible explanation is that the real surface area is getting closer to the geometric area as the thickness of the insulator layer increases.

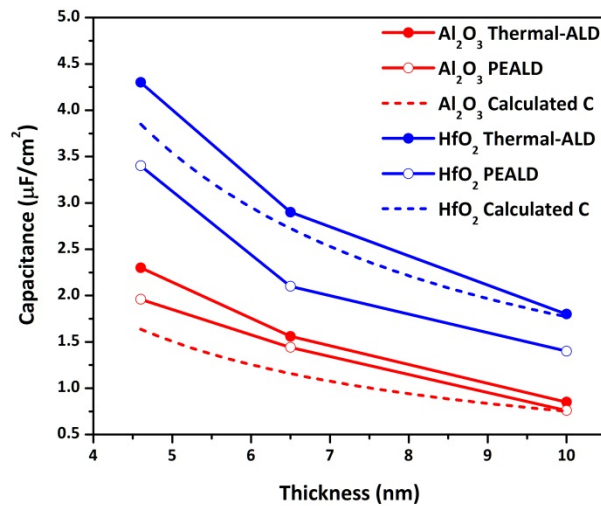


Figure 5-8 Capacitance vs thickness for MIM structures prepared by PEALD and thermal ALD.

5.3.3 IV Characteristics

The IV characteristics of the fabricated Cr/ 4.6 nm Al₂O₃/Cr diodes are shown in Figure 5-9. At low applied voltages, the leakage current was very small (on the

order of few nA). At higher potentials, a rapid increase in the current was observed that is described as Fowler–Nordheim tunneling. Further increase in the applied voltage led to irreversible breakdown of the insulating layer.

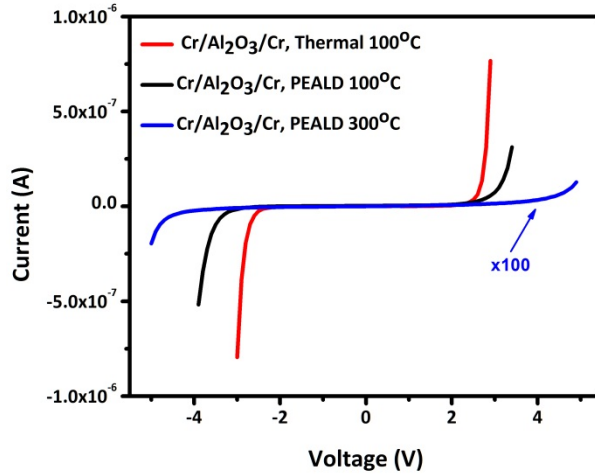


Figure 5-9 IV characteristics of MIM diodes with Cr/Al₂O₃/Cr structure with an ALD oxide thickness of 4.6 nm.

Comparison between the diodes made by PEALD and thermal ALD revealed that the Fowler–Nordheim tunneling occurred at higher potentials for diodes made from PEALD films. Consequently, a higher breakdown voltage was also observed for PEALD diodes compared to the thermal ALD. Additionally, the diodes fabricated by PEALD, had lower leakage currents than thermal ALD with the same ALD oxide thickness. This difference was due to the interfacial chromium oxide layer which increased the overall thickness of the insulating layer in the diodes made by PEALD.

The effect of deposition temperature on tunneling characteristics was also seen by comparing IV curves for diodes with oxides grown by PEALD at 100°C and 300°C. The increase in the deposition temperature resulted in a higher breakdown voltage and a lower tunneling current. The interfacial oxide was measured to be

slightly thicker for films deposited at higher temperatures which increased the overall thickness causing the tunneling to occur at a higher voltage. Additionally, a better oxide quality was obtained for films grown at 300°C (lower impurity levels) which affected the electrical performance. Beside breakdown voltage, another property of these IV curves is their asymmetry which is defined here as the ratio of absolute measured current at an applied voltage bias of ± 2 V. A higher asymmetry value of 2.6 was obtained for diodes with PEALD oxide compared to a value of 1.3 for thermal ALD-grown diodes. A zero-bias resistance of $0.9 \times 10^{12} \Omega$ and $1.2 \times 10^{12} \Omega$ was measured for thermal ALD and PEALD diodes, respectively.

Figure 5-10 shows IV curves for MIM diodes with HfO_2 as the insulator layer. Similar to Al_2O_3 diodes, HfO_2 diodes behaved differently for thermal ALD and PEALD. This was due to the presence of the interfacial chromium oxide layer. The zero-bias resistance was measured to be $1.2 \times 10^{11} \Omega$ and $2.3 \times 10^{11} \Omega$ for thermal ALD and PEALD diodes, respectively. The IV curve for a Cr/ 6.5 nm HfO_2 /Cr is also presented in Figure 5-10 to illustrate the effect of insulator thickness on the IV curves.

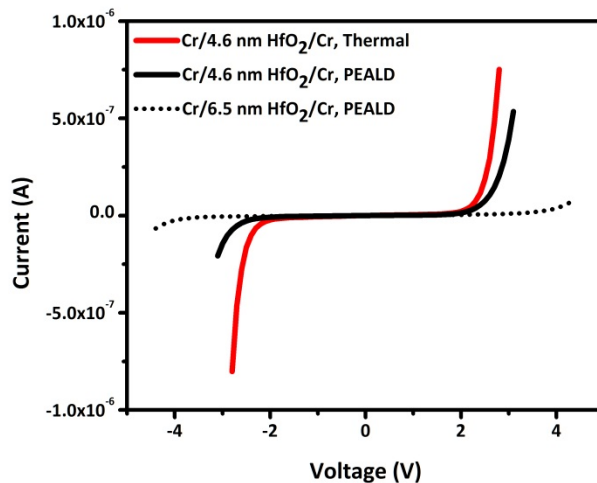


Figure 5-10 IV curves for MIM diodes with Cr/ HfO_2 /Cr structure.

The IV characteristics of Cr/Al₂O₃/Cr diodes with PEALD oxide thickness of 1.5 and 2.3 nm is shown in Figure 5-11. 1.5 nm (10 PEALD cycles) was the thinnest ALD oxide thickness that resulted in working MIM diodes. The diodes with thinner oxides were electrically shorted. Unlike diodes with thicker insulating layers, for 1.5 nm diode the tunneling occurs at very small potentials. The overall insulator thickness in this sample was ~3 nm, including the interfacial chromium oxide layer. Since the RMS value for surface roughness of Cr metals was ~ 1.4 nm, the ALD oxide needed to be at least equal to the RMS roughness for MIM diodes to be working. For thermal ALD, the minimum required thickness was 4 nm which indicated that PEALD was a more practical tool for fabrication of MIM diodes with ultra-thin layers (plasma grows a thicker chrome oxide layer which produced a smoother PEALD layer than thermal ALD). The minimum oxide thickness can be lowered by decreasing the surface area of the diodes as well as reducing the surface roughness of the metallic electrodes.

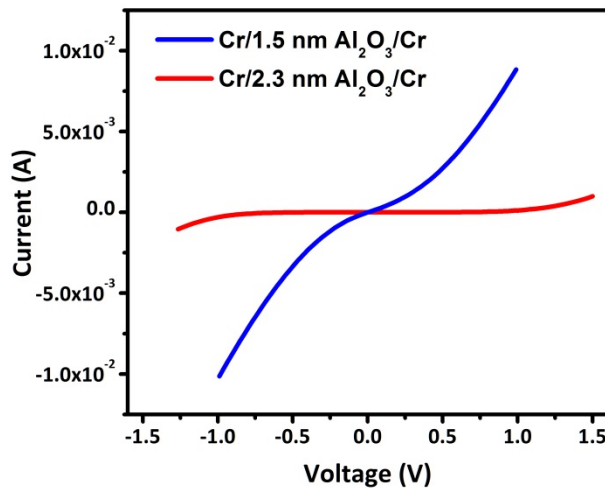


Figure 5-11 IV curves for MIM diodes (Cr/PEALD Al₂O₃/Cr)

The XPS and CV data indicated that the MIM diodes with ALD oxides deposited at higher temperatures had a superior quality with respect to impurity levels, density and dielectric properties. PEALD seemed to be a more suitable option due

to its linear growth characteristics and lower impurity levels. The samples with oxide grown by thermal ALD at high substrate temperatures were often electrically short. As a result of growth delays combined with the rough surface of the substrate, the final film was neither uniform nor thick enough to electrically isolate the two metallic electrodes. The main limitation in applying the PEALD in fabrication of MIM diodes was the possible effects of the interfacial oxide layer. However, the oxidation of the metal electrode during the PEALD could be effectively reduced by utilizing a combination of thermal ALD and PEALD. The metal surface can be protected against plasma oxidation by depositing a very thin layer of oxide using thermal ALD (thickness ~ 0.5 nm) prior to the main PEALD process. The thin oxide layer acts as a diffusion barrier and reduces the oxidation rate of metal substrate when exposed to oxygen plasma during PEALD. For instance when the desired insulating layer is 5 nm of aluminum oxide, a 0.5 nm Al_2O_3 layer is first deposited by thermal ALD followed by deposition of 4.5 nm Al_2O_3 by PEALD. Figure 5-12 demonstrates the difference between the two types of MIM diodes, one with the interfacial oxide layer and the other without it. In Figure 5-12a, the schematics of the two samples with a Cr/4-nm Al_2O_3 /Cr structure are shown.

The left sample had a regular PEALD recipe (at 300°C) which resulted in formation of an interfacial chromium oxide layer. The right sample had the modified thermal ALD/PEALD recipe. *In-situ* ellipsometry data proved that the effect of oxygen plasma on the metal substrate was minimal when this recipe was used.

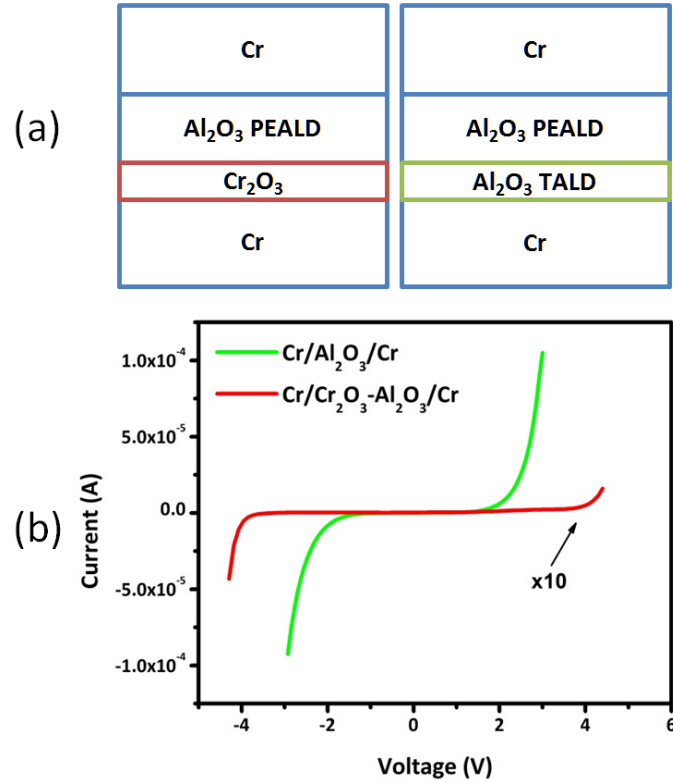


Figure 5-12 Comparison between diodes fabricated by regular PEALD and combination of TALD/PEALD. (a) Schematic representation of diode structures made by PEALD (left) and TALD/ PEALD (right). (b) The corresponding IV curves for the two different type of structures.

Figure 5-12 b shows the IV curve for the two samples. The sample with interfacial oxide layer had a higher breakdown voltage and lower current flow which was expected from its thicker insulating layer (Al₂O₃ + Cr₂O₃). Due to the presence of chromium oxide, the current in the forward and reverse bias was not the same (an asymmetry value of 3.9 at 4.3V). The sample without the interfacial layer had a smaller total thickness (only Al₂O₃). Therefore, it showed a smaller breakdown voltage. Additionally, a symmetric IV curve was observed for this sample. The increase in asymmetry for MIM diodes fabricated by regular PEALD process can be regarded as an advantage when high non-linearity is desired. Recently, it was demonstrated that high IV non-linearity could be achieved by utilizing multilayers instead of single insulating layers. For instance, a diode with Cr/Cr₂O₃-Al₂O₃-

HfO₂/Cr produced very high non-linear IV curves*. In this case, the presence of the interfacial oxide did not have any negative effect.

5.3.4 MIM Diodes with Multiple Insulating Layers

In order to increase the IV asymmetry, one approach is to have multiple insulating layers instead of one single layer. Since the electron tunneling probability depends on the insulator thickness and the metal work function, the barrier under forward and reverse bias must be different to increase asymmetry. The idea initially proposed by Di Ventra *et al.* [23] was that an electron tunneling device consisting of laterally indented barriers would have enhanced non-linearity compared to a conventional MIM device. A comparison between the IV characteristics of an MIM diode with two insulating layers, Al₂O₃ and HfO₂, and two MIM diodes with single layers is shown in Figure 5-13. The overall thickness was 4 nm for all the diodes. It can be seen that the MIM diode with two layers presents an asymmetric curve. The films were all deposited by PEALD at 300°C. In order to prevent the formation of the Cr interfacial oxide layer, the Cr films were transferred under vacuum to the ALD chamber after the sputtering process. Additionally, the Cr surface was first coated with 0.5 nm of Al₂O₃ by thermal ALD to protect the metal surface against oxidation during the subsequent PEALD, as discussed earlier.

* Paper under publication: Observation of Resonant Tunneling Phenomenon in Metal-Insulator-Insulator-Insulator-Metal Electron Tunnel Devices, Appl. Phys. Lett. (2012)

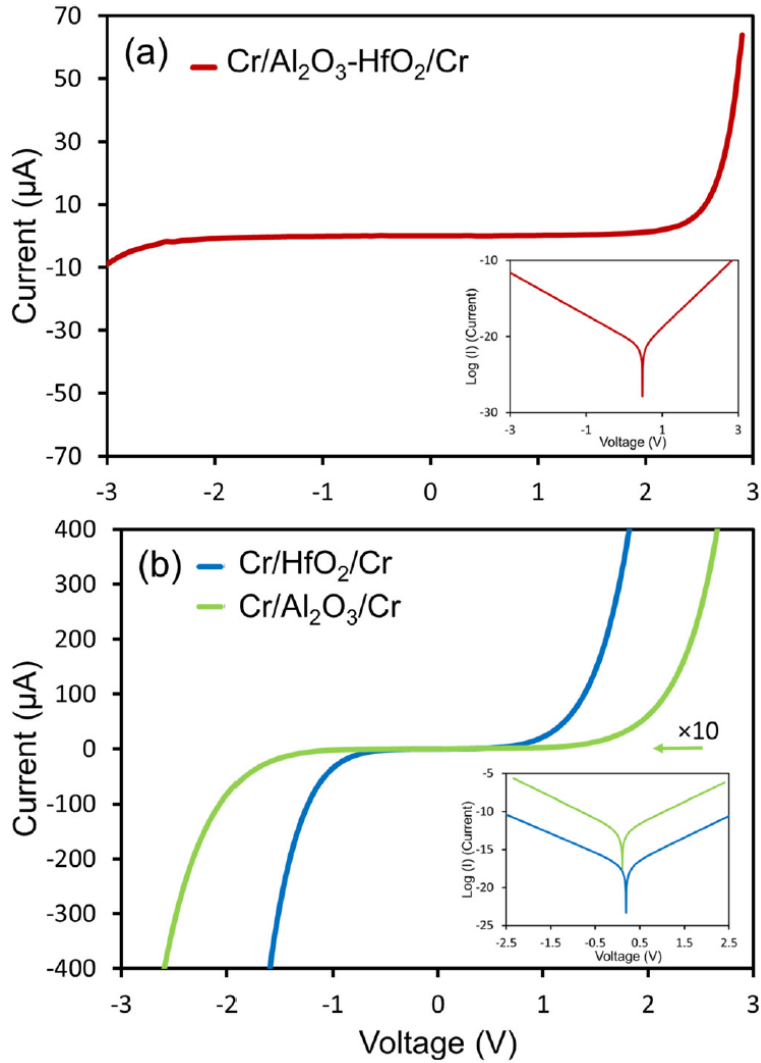


Figure 5-13 IV curves for (a) the Cr/2nm Al₂O₃- 2 nmHfO₂/Cr and (b) the Cr/4 nm HfO₂/Cr and Cr/4nm Al₂O₃/Cr diodes* .

5.4 Conclusions

MIM diodes were fabricated by depositing thin layers of Al₂O₃ and HfO₂ on sputtered Cr electrodes using ALD operated in thermal and plasma-enhanced

* The graphs in this figure have been published in:
P. Maraghechi, A. Foroughi-Abari, K. Cadien, and A. Y. Elezzabi, Appl. Phys. Lett. 99, 253503 (2011)

modes. The thickness and growth characteristics of ALD films on Cr electrodes were analysed using *in-situ* spectroscopic ellipsometry. The results showed that during the plasma ALD, a thin interfacial chromium oxide layer was formed between the ALD oxide and the metallic layer. Electrical characterization revealed that the interfacial oxide layer could alter various properties of the MIM diodes. MIM diodes fabricated using PEALD, showed higher breakdown voltage, higher zero bias resistance and less leakage current. Additionally, MIM diodes prepared using PEALD had lower capacitance compared to those prepared using thermal ALD. Thermal ALD and PEALD can both be successfully used in the fabrication process of MIM diodes. PEALD is a more suitable method for preparation of MIM diodes with ultra-thin dielectric layers.

5.5 References

- [1] A. Sanchez, C.F. Davis, K.C. Liu, A. Javan, *Journal of Applied Physics* 49/10 (1978) 5270.
- [2] F.K. Kneubuhl, C. Fumeaux, W. Herrmann, H. Rothuizen, *Infrared Phys Techn* 39/3 (1998) 123.
- [3] B. Tiwari, J.A. Bean, G. Szakmany, G.H. Bernstein, P. Fay, W. Porod, *J Vac Sci Technol B* 27/5 (2009) 2153.
- [4] P. Esfandiari, G. Bernstein, P. Fay, W. Porod, B. Rakos, A. Zarandy, B. Berland, L. Boloni, G. Boreman, B. Lail, B. Monacelli, A. Weeks, *Infrared Technology and Applications XXXI*, Pts 1 and 2 5783 (2005) 470.
- [5] P.C.D. Hobbs, R.B. Laibowitz, F.R. Libsch, *Appl Optics* 44/32 (2005) 6813.
- [6] I. Wilke, W. Herrmann, F.K. Kneubuhl, *Appl Phys B-Lasers O* 58/2 (1994) 87.
- [7] R. Corkish, M.A. Green, T. Puzzer, *Sol Energy* 73/6 (2002) 395.
- [8] G.M. Elchinger, A. Sanchez, C.F. Davis, A. Javan, *Journal of Applied Physics* 47/2 (1976) 591.
- [9] M. Heiblum, S. Wang, J.R. Whinnery, T.K. Gustafson, *IEEE J Quantum Elect* 14/3 (1978) 159.
- [10] E.N. Grossman, T.E. Harvey, C.D. Reintsema, *Journal of Applied Physics* 91/12 (2002) 10134.
- [11] P.A. Parilla, P. Periasamy, J.J. Berry, A.A. Dameron, J.D. Bergeson, D.S. Ginley, R.P. O'Hayre, *Adv Mater* 23/27 (2011) 3080.
- [12] E.W. Cowell, N. Alimardani, C.C. Knutson, J.F. Conley, D.A. Keszler, B.J. Gibbons, J.F. Wager, *Adv Mater* 23/1 (2011) 74.
- [13] H. Kim, P.C. McIntyre, *J Korean Phys Soc* 48/1 (2006) 5.
- [14] K.E. Elers, T. Blomberg, M. Peussa, B. Aitchison, S. Haukka, S. Marcus, *Chemical Vapor Deposition* 12/1 (2006) 13.

- [15] L. Niinisto, J. Paivasaari, J. Niinisto, M. Putkonen, M. Nieminen, *Physica Status Solidi a-Applied Research* 201/7 (2004) 1443.
- [16] R.L. Puurunen, *Journal of Applied Physics* 97/12 (2005) 121301.
- [17] M. Ritala, M. Leskela, *Nanotechnology* 10/1 (1999) 19.
- [18] H. Kim, H.-B.-R. Lee, W.J. Maeng, *Thin Solid Films* 517/8 (2009) 2563.
- [19] T.O. Kääriäinen, D.C. Cameron, *Plasma Processes and Polymers* 6/S1 (2009) S237.
- [20] A. Foroughi-Abari, C. Xu, K.C. Cadien, *Thin Solid Films* 520 (2011) 1762.
- [21] J.L. van Hemmen, S.B.S. Heil, J.H. Klootwijk, F. Roozeboom, C.J. Hodson, M.C.M. van de Sanden, W.M.M. Kessels, *Journal of The Electrochemical Society* 154/7 (2007) G165.
- [22] G. He, M. Liu, L.Q. Zhu, M. Chang, Q. Fang, L.D. Zhang, *Surface Science* 576/1–3 (2005) 67.
- [23] M. Di Ventra, G. Papp, C. Coluzza, A. Baldereschi, P.A. Schulz, *Journal of Applied Physics* 80/7 (1996) 4174.

Chapter 6 Summary, Conclusions, and Future Directions

Deposition of metal oxides on metallic substrates using ALD was studied in this thesis. Special attention was given to the growth of aluminum oxide on chromium metal. Chapter 2 focused on characterizing the deposition of metal oxides on silicon substrates using various analytical techniques such as spectroscopic ellipsometry, XPS, TEM, and FTIR. The ALD research system used in the experiments had the capability to operate in the conventional thermal and plasma-enhanced modes. The films deposited in these two different operation modes were compared in terms of growth characteristics and other properties such as chemical analysis, and index of refraction. Compositional analysis performed by XPS measurements showed that all the ALD films contained carbon as impurity. The oxygen to metal ratio was also determined to be higher than the stoichiometry ratio. Both the impurity levels and oxygen to metal ratio were improved by increasing the deposition temperature. XPS analysis was insensitive to hydrogen level in the films. Other analytical techniques such as Rutherford backscattering spectrometry (RBS) can be used to reliably determine the hydrogen level in the films. The results can then be used to describe the relation between hydrogen content and ALD process parameters. It is also important to note that the characterization was only done on as-deposited films. Thermal annealing can be performed to decrease the impurity level.

To study the ALD film growth on metallic substrates, thin metal films were deposited on silicon and silicon oxide substrates by means of D.C. magnetron sputtering. The metal films were then transferred under vacuum to the ALD chamber to monitor the film deposition using *in-situ* spectroscopic ellipsometry. Chapter 3 presented the results on the relationship between sputtering parameters, mainly base pressure and argon working pressure, and the film properties including microstructure, resistivity, and impurity levels in the sputtering process of chromium as a representative of metals. The results showed that low sputtering pressure and low base pressure were needed to obtain chromium thin films with low oxygen levels and low resistivity values. The depositions were done at room temperature. Further examination with the addition of substrate temperature as a parameter is proposed as a future step.

In Chapter 4, *in-situ* spectroscopic ellipsometry was used to monitor the film growth during the ALD of metal oxides on metallic substrates, both in thermal and plasma-enhanced ALD. The exposure of metal surface to highly reactive oxygen radicals generated in the oxygen plasma resulted in the oxidation of the metal surface. The oxidation kinetics was monitored for several metals including chromium, tantalum, nickel, and silver. Cabrera-Mott oxidation model was implemented to describe the complex oxidation kinetics. *In-situ* ellipsometry was shown to be a very capable and precise tool for observation of oxidation process in oxygen plasma environment.

The results showed that a thin layer of interfacial metal oxide formed when plasma-enhanced ALD was used. Additionally, the relation between the interfacial layer thickness and ALD process parameters was investigated. Thermal ALD did not involve any oxidation of the base metal; however, non-linear growth was observed for the deposition at temperatures above 100°C. The exact nature of this type of growth could not be determined. More experiments are needed to shed light on this phenomenon. High-resolution cross-section TEM imaging and Auger electron spectroscopy (AES) elemental mapping may be used to study the possible nucleation of oxides on metal substrates.

The results also showed that covering the metal surface with a very thin (~0.5 nm) layer of thermal ALD oxide could effectively protect the metal surface from oxidation during the PEALD process. It was demonstrated that PEALD can be employed to prepare oxide films on metallic substrates without the formation of interfacial oxide layers.

Chapter 5 presented the fabrication and characterization of metal-insulator-metal (MIM) diodes as an important application of ALD film deposition on metal substrates. MIM diodes were fabricated using combination of metal sputtering and ALD operated in both thermal and plasma-enhanced modes. The diodes were then electrically characterized to determine their electrical performance. The results showed that both thermal and plasma-enhanced ALD could be successfully employed to fabricate MIM diodes; however, plasma-enhanced ALD was preferred due to its flexibility and superior device performance. It is important to note that one must pay attention to the presence of interfacial oxide layer when plasma-enhanced ALD is used, as this thin layer could alter the device electrical characteristics. However, the oxidation of the metal electrode during the PEALD could be effectively reduced by utilizing a combination of thermal ALD and PEALD.

With the knowledge of ALD growth characteristics on metals, novel MIM devices with multiple insulating layers were fabricated which presented enhanced properties such as high non-linearity.

One of the major drawbacks of using sputtering to prepare metal surfaces for MIM fabrication was that the metal surfaces are usually very rough. A possible solution is to polish the metal surface to obtain an atomically smooth surface. This could be done using chemical mechanical polish (CMP). Having a very smooth metal surface would allow fabrication of MIM diodes with an insulator thinner than 2 nm which could improve the quantum tunneling current.